NANOMATERIALS

Carbothermal shock synthesis of high-entropy-alloy nanoparticles

Yonggang Yao,[1]* Zhennan Huang,[2]* Pengfei Xie,[3]* Steven D. Lacey,[1]* Rohit Jiji Jacob,[4] Hua Xie,[1] Fengjuan Chen,[1] Anmin Nie,[2] Tiancheng Pu,[3] Miles Rehwoldt,[4] Daiwei Yu,[5] Michael R. Zachariah,[4] Chao Wang,[3]† Reza Shahbazian-Yassar,[2]† Ju Li,[5]† Liangbing Hu[1]†

The controllable incorporation of multiple immiscible elements into a single nanoparticle merits untold scientific and technological potential, yet remains a challenge using conventional synthetic techniques. We present a general route for alloying up to eight dissimilar elements into single-phase solid-solution nanoparticles, referred to as high-entropy-alloy nanoparticles (HEA-NPs), by thermally shocking precursor metal salt mixtures loaded onto carbon supports [temperature ~2000 kelvin (K), 55-millisecond duration, rate of ~10^5 K per second]. We synthesized a wide range of multicomponent nanoparticles with a desired chemistry (composition), size, and phase (solid solution, phase-separated) by controlling the carbothermal shock (CTS) parameters (substrate, temperature, shock duration, and heating/cooling rate). To prove utility, we synthesized quinary HEA-NPs as ammonia oxidation catalysts with ~100% conversion and >99% nitrogen oxide selectivity over prolonged operations.

Multimetallic nanoparticles (MMNPs) are of interest in a wide range of applications, including catalysis (*1*–*7*), energy storage (*8*), and bio/plasmonic imaging (*8*, *9*). Alloying multiple metallic elements into individual nanoscale products offers the promise of material properties that could exceed single-element (or unary) nanoparticles (*2*, *5*, *6*). The current and primary approaches toward the preparation of MMNPs arise from wet-chemistry synthesis, where a variety of particle sizes, shapes, and phases can be attained (*3*, *4*, *7*, *10*). However, most studies via wet-chemical methods report alloy compositions not exceeding three elements, which limits the compositional space. Additionally, more site-specific synthesis techniques, including printing- and lithography-based methods (*1*, *11*, *12*), have shifted the compositional space toward quaternary and even quinary nanostructures; however, the subsequent reduction procedures tend to limit the structural complexity to phase-separated MMNPs, especially for immiscible elemental combinations (*1*, *12*, *13*). In terms of bulk material synthesis, melt processing is a scalable method that has led to the creation of high-entropy alloys (HEAs) consisting of five or more elements in a solid solution (uniform mixing), which have shown great potential as structural materials (*14*–*18*). To date, only a limited family of HEAs have been achieved, due to the difficulty of mixing elements with vastly different chemical and physical properties, as well as cooling rate constraints. Moreover, downsizing HEAs to the nanoscale is a daunting task, especially by conventional alloying methods. Therefore, the development of a synthesis method where elemental composition, particle size, and phase can be precisely controlled could bring about a new repertoire of alloys and nanostructures with unprecedented functionalities.

We developed a facile, two-step carbothermal shock (CTS) method that employs flash heating and cooling (temperature of ~2000 K, shock duration of ~55 ms, and ramp rates on the order of 10^5 K/s) of metal precursors on oxygenated carbon support to produce high-entropy-alloy nanoparticles (HEA-NPs) with up to eight dissimilar metallic elements (table S1). MMNPs synthesized by CTS have a narrow size distribution and are uniformly dispersed across the carbon support, despite being exposed to high temperatures that conventionally cause particle coarsening. The high temperature, in conjunction with the catalytic activities of the liquid metals, drives rapid particle "fission" and "fusion" events that result in uniform mixtures of multiple elements. Subsequently, the rapid cooling rate facilitates kinetic control over the thermodynamic mixing regimes and enables the formation of crystalline solid-solution nanoparticles, analogous to

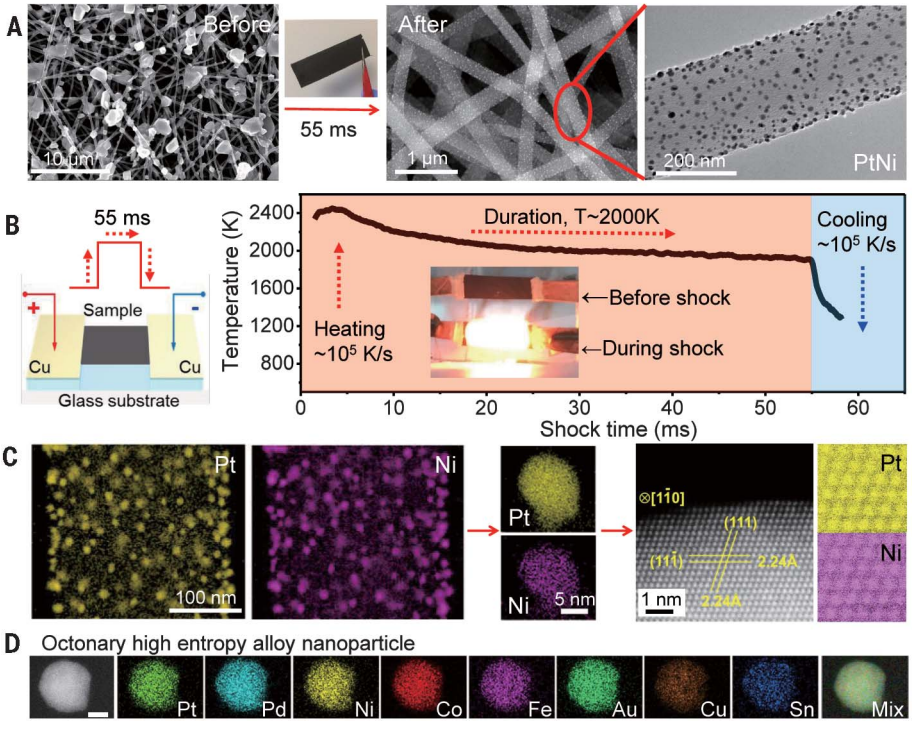

Fig. 1. CTS synthesis of HEA-NPs on carbon supports. (**A**) Microscopy images of microsized precursor salt particles on the carbon nanofiber (CNF) support before thermal shock, as well as the synthesized, well-dispersed (PtNi) nanoparticles after CTS. (**B**) Sample preparation and the temporal evolution of temperature during the 55-ms thermal shock. (**C**) Low-magnification and single-particle elemental maps, an HAADF image, and corresponding atomic maps for a binary PtNi alloy. (**D**) Elemental maps of an HEA-NP composed of eight dissimilar elements (Pt, Pd, Ni, Co, Fe, Au, Cu, and Sn). Scale bar, 10 nm.

Downloaded from http://science.sciencemag.org/ on March 31, 2018

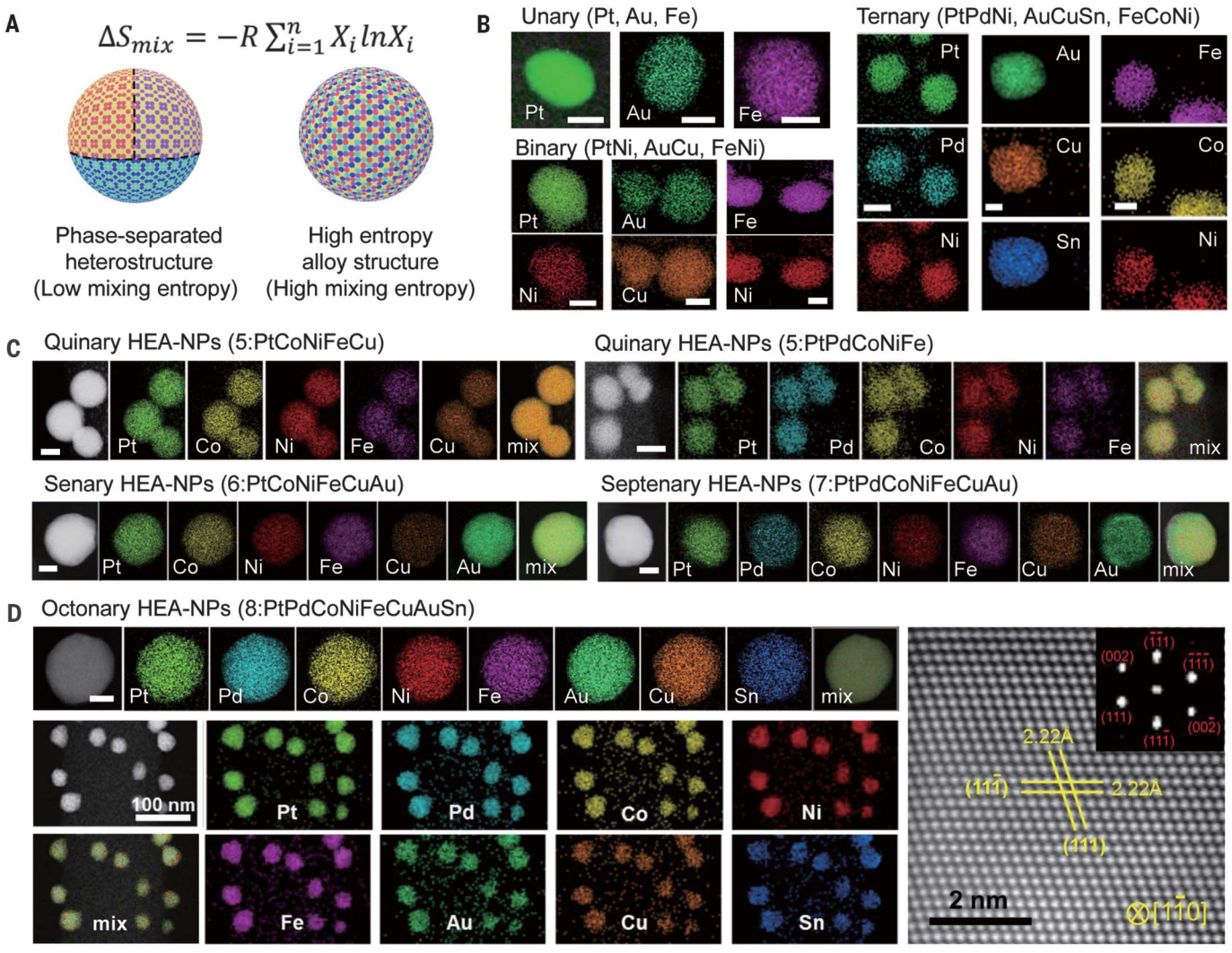

Fig. 2. Elemental characterization of HEA-NPs. (**A**) Schematic comparison of phase-separated heterostructures synthesized by a conventional slow reduction procedure (slow kinetics) versus solid-solution HEA-NPs synthesized by the CTS method (fast kinetics). (**B**) STEM elemental maps of unary (Pt, Au, and Fe), binary (PtNi, AuCu, and FeNi), and ternary (PtPdNi, AuCuSn, and FeCoNi) nanoalloys. Scale bar, 5 nm. (**C**) HAADF images and STEM elemental maps of HEA-NPs: quinary (PtFeCoNiCu and PtPdCoNiFe), senary (PtCoNiFeCuAu), and septenary (PtPdCoNiFeCuAu). Scale bar, 10 nm. (**D**) Individual and low-magnification elemental maps (left) and a high-resolution HAADF-STEM image with fast Fourier transform analysis (right) of octonary (PtPdCoNiFeCuAuSn) HEA-NPs, showing solid solutions with an fcc structure. The low-magnification elemental maps verify the structural and compositional uniformity of the HEA-NPs. Scale bar, 10 nm.

martensitic steels and metallic glasses that are also kinetically trapped (*19*, *20*). By adjusting the input electrical pulse parameters, we can also produce phase-separated nanoparticles by decreasing the cooling rate. This CTS technique opens a vast space for synthesizing alloys and nanocrystals, which has potential for a wide range of applications.

[1]Department of Materials Science and Engineering, University of Maryland, College Park, MD 20742, USA. [2]Department of Mechanical and Industrial Engineering, University of Illinois at Chicago (UIC), Chicago, IL 60607, USA. [3]Department of Chemical and Biomolecular Engineering, Johns Hopkins University, Baltimore, MD 21218, USA. [4]Department of Chemical and Biomolecular Engineering and Chemistry and Biochemistry, University of Maryland, College Park, MD 20742, USA. [5]Department of Nuclear Science and Engineering, Department of Materials Science and Engineering, and Department of Electrical Engineering and Computer Science, Massachusetts Institute of Technology, Cambridge, MA 02139, USA.
*These authors contributed equally to this work.
†Corresponding author. Email: binghu@umd.edu (L.H.); rsyassar@uic.edu (R.S.-Y.); liju@mit.edu (J.L.); chaowang@jhu.edu (C.W.)

Results

The CTS method we used to synthesize uniformly dispersed, solid-solution nanoparticles (up to eight elements) requires two steps (*21*). First, we mixed metal salt precursors MCl_xH_y (M is Pt, Pd, Ni, Fe, Co, Au, Cu, or Sn, among others) into a solution and loaded onto a conductive carbon support, such as carbon nanofibers (CNFs). CNFs carbonized at 1073 K (CNF-1073K, denoted as CNF hereafter) are the substrates used in this work unless stated otherwise. After drying, we exposed the precursor-loaded sample to a rapid thermal shock (55 ms) in an Ar-filled glovebox, which leads to a high concentration of nanoparticles (e.g., PtNi) that form across the carbon surface (Fig. 1A and figs. S1 to S4). The electrical pulse that we applied controls the thermal exposure conditions (Fig. 1B), with a common temperature of ~2000 K and heating/cooling rates up to ~10^5 K/s as measured with a pyrometer (figs. S5 to S7). We found no apparent elemental segregation or phase separation for the PtNi nanoparticles (Fig. 1C and fig. S4) using scanning transmission electron microscopy (STEM) elemental maps. The high-angle annular dark-field (HAADF) images and atomic maps also demonstrated both uniform atomic scale mixing and the formation of a face-centered cubic (fcc) crystalline structure (Fig. 1C). Our general method extends to more complex HEA-NPs. For example, we readily fabricated HEA-NPs composed of eight dissimilar elements (Pt, Pd, Ni, Co, Fe, Au, Cu, and Sn). These elements

Downloaded from http://science.sciencemag.org/ on March 31, 2018

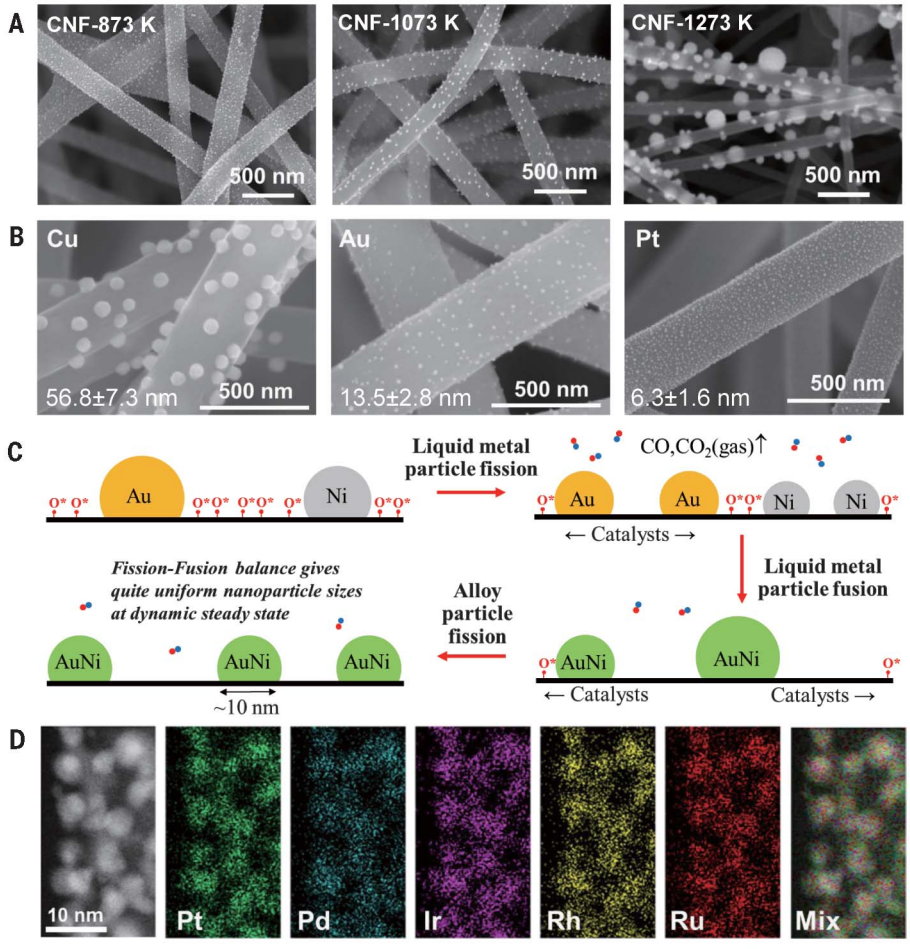

Fig. 3. Particle dispersion mechanism for the CTS process. (**A**) SEM images of synthesized AuNi nanoparticles on CNFs carbonized at different temperatures: 873, 1073, and 1273 K. A higher carbonization temperature leads to higher crystallinity and lower defect concentrations within the carbon support, which affects particle size and dispersion. (**B**) SEM images of Cu, Au, and Pt particle distributions synthesized on identical CNF supports via the same CTS process. The higher catalytic activities of the metal species (Au and Pt) lead to smaller nanoparticles and more uniform distributions. (**C**) An illustration of the catalysis-driven particle fission/fusion mechanism to synthesize uniformly dispersed HEA-NPs. (**D**) HAADF image and elemental maps of ultrafine and well-dispersed quinary HEA-NPs (PtPdIrRhRu) on CO_2-activated CNFs. A narrow size distribution is achieved by increasing the support's surface defect concentration through CO_2 activation, as well as employing metal species with high catalytic activities.

have a range of atomic radii (1.24 to 1.44 Å), reduction potentials (−0.25 to 1.5 V versus the standard hydrogen electrode), preferred crystal structures (fcc, body-centered cubic, hexagonal close-packed, or tetragonal), and melting temperatures (500 to 2000 K) that typically prevents solid-solution formation (Fig. 1D and table S2).

MMNPs have been previously synthesized using conventional reduction procedures (*1*, *3*). However, these synthetic methods tend to create phase-separated heterostructures among immiscible elements, which greatly reduces the configurational entropy of mixing (fig. S8). The CTS process leads to solid solution MMNPs (i.e., HEA-NPs), where arbitrary metallic elements are completely mixed to maximize the mixing entropy (ΔS_{mix}) (Fig. 2A). We demonstrated the versatility by synthesizing a series of multi-element nanoparticles and characterized them by STEM, transmission EM (TEM), scanning EM (SEM), and energy-dispersive x-ray spectroscopy (EDS). We synthesized unary (Pt, Au, and Fe), binary (PtNi, AuCu, and FeNi), and ternary (PtPdNi, AuCuSn, and FeCoNi) nanoparticles that exhibit compositional uniformity (Fig. 2B). The nanoparticles also possess size uniformity, with diameters of ≥5 nm (fig. S9), regardless of the elemental compositions. By adding additional metal salts to the precursor solutions, we synthesized quinary (PtCoNiFeCu and PtPdCoNiFe), senary (PtCoNiFeCuAu), septenary (PtPdCoNiFeCuAu) and octonary (PtPdCoNiFeCuAuSn) HEA-NPs, which are solid solutions and evenly dispersed across the carbon support (Fig. 2, C and D, and figs. S10 to S16). Moreover, the HEA-NPs are of nanoscale dimensions in fcc crystal structures (Fig. 2D and figs. S17 and S18).

The HEA-NPs exhibited solid solution mixing via the same 55-ms thermal shock protocol (figs. S19 and S21). We confirmed the structural uniformity (no phase separation) and negligible chlorine content with STEM (figs. S22 to S26), x-ray diffraction (XRD) (figs. S27 to S29), and x-ray photoelectron spectroscopy (XPS) (figs. S30 to S36). A statistical study conducted over different sample regions confirms the compositional uniformity among the synthesized nanoparticles (figs. S37 to S43). For example, the compositional variation for each element in our quinary HEA-NPs (PtPdCoNiFe) is ~10%, which is smaller than the >50% variation reported for lithography-based techniques (fig. S42) (*1*). Additionally, the macroscopic compositions that we determined by inductively coupled plasma mass spectroscopy (ICP-MS) agree well with the STEM-derived statistics. The HEA-NP composition has a small deviation from the ideal composition based on the initial precursor salt molar ratios, due to vapor loss at high temperature (figs. S44 to S46 and table S3). To demonstrate compositional control, we employed the (precursor) compensation approach, which is a common strategy in high-temperature synthesis when volatile elements are involved (figs. S47 to S52).

The HEA-NPs deviate from the phase-separated thermodynamic equilibrium structures reported in literature (*1*, *3*, *12*) due to the rapid quench-induced nucleation/growth process of the CTS method, which "freezes" the liquid alloy state to create solid-solution nanoparticles. The synthesized HEA-NPs are stable at room temperature and remained unchanged in terms of size, structure, and composition after 11 months of storage under standard conditions.

In addition to the rich chemistries, the morphologies of the synthesized nanoparticles indicate a formation mechanism for CTS that differs from other alloying approaches. Because ~2000 K far exceeds the thermal decomposition temperature of metal precursors (table S1), the salts easily decompose:

$$MCl_xH_y \rightarrow M(liq) + gases\uparrow \quad (1)$$

However, ~2000 K is below the boiling points of the metallic elements. In this case, the metallic elements are likely in the liquid phase and should be on a similar length scale as the initial (microsized) salt precursors. Since metals are nonwetting with carbon, the liquid metals should coarsen to minimize their surface energy at high temperature (*22*). Our observation departs from this behavior, requiring a mechanism to explain how initially single-element, micron-sized liquid metal droplets form uniformly dispersed alloy nanoparticles.

We performed two control experiments to explore HEA-NP formation. We found distinct particle morphology differences using the same CTS protocol (Fig. 3A and figs. S53 and S54), but with

Downloaded from http://science.sciencemag.org/ on March 31, 2018

supports differing in carbonization temperature. Specifically, electrospun polyacrylonitrile fibers carbonized in argon at a range of temperatures (873, 1073, and 1273 K) generated CNF supports with various defect concentrations. Lower carbonization temperatures resulted in smaller, more uniform particle dispersions. Each pyrolysis temperature was insufficient to drive away all surface-bound oxygen (O*) and thus resulted in an increasing amount of O* residuals remaining on CNFs carbonized at lower temperatures (fig. S2). Therefore, we surmised that the surface defect concentration of the carbon support is an important parameter for particle dispersion. Our second control experiment used identical CNF supports (CNF-1073K) and synthesis conditions (55 ms, ~2000 K), but with a variety of single-metal salt precursors (Fig. 3B and figs. S55 to S57). Nanoparticle size distribution changes in this case with Cu having a much larger particle size (~56.8 nm) than Au (~13.5 nm) and Pt (~6.3 nm). This trend resembles the catalytic activities of the corresponding elements, with Pt and Cu being the most and least active, respectively. Because Au and Cu possess similar physical properties (table S4), the discrepancy requires a different particle dispersion mechanism than a simple, physical melting-and-nucleation process.

Since defects and metal catalysts play a key role during the CTS process, we considered a catalytically driven particle dispersion mechanism for the defective carbon supports. To verify this, we used in situ mass spectrometry to analyze the gases created during CTS for defective CNF supports with and without precursor salts. Compared with bare CNF, the precursor-loaded CNF exhibited a larger and much sharper release of CO gas during the CTS process (fig. S58). Thus, the release of CO gas upon thermal shock arises from a catalytically driven carbon metabolism reaction:

$$C + O^* \rightarrow CO \uparrow \quad (2)$$

where O* denotes surface-bound residual oxygen. The carbon metabolism reaction involves C (fuel), O* (oxidizer), and metal (catalyst), which correlates the surface defect concentration (e.g., carbonization temperature) and the metal's catalytic activity to the final nanoparticle size and level of dispersity. We hypothesize that during the 55-ms high-temperature exposure, the liquid metal droplets actively travel around and split ("fission") to harvest the dispersed O* on the carbon surface based on the catalytically driven reaction, C + O* = CO (gas) (ΔH = –110.5 kJ/mol). Previously published works (*23*–*26*) and an in situ TEM study (*27*) also showed that metallic particles can move and split under a catalytic driving force, which is similar to our proposed carbon metabolism reaction.

Mechanistically (Fig. 3C), a larger O* concentration and the use of catalytically active metals can drive vigorous metabolism with more frequent catalyst motion and fission events. This opposes equilibrium thermodynamic directive for the metal droplets to coarsen. Conversely, depleted O* concentrations should lead to decreased mobility and the localization of liquid droplets that coarsen slowly to reduce their total surface energy. The liquid alloys have a wide solubility range at ~2000 K. Therefore, the liquid metal movement driven by O* harvesting allows different droplet compositions to continually meet and fuse into single-phase alloys during the CTS process. Numerous particle fusion and fission events, which we estimated to be >10^6 times based on time-scale analysis (fig. S59) (*28*–*30*), yield a dynamic steady state during the 55-ms high-temperature shock. This enables uniform nanoscale dispersions and homogeneous high-entropy mixing. To verify the effects of supports with more surface-bound defects, we synthesized quinary HEA-NPs (PtFeCoNiCu) on CNFs with and without CO_2 activation, resulting in 5.30 ± 1.31-nm particles on CO_2-activated CNFs and 11.3 ± 2.2-nm particles on CNFs (fig. S60). We achieved further improvements in ultrafine particle sizes and narrow distributions when more catalytically active metal combinations (PtPdIrRhRu HEA-NPs, 3.28 ± 0.81 nm) are employed on identical CO_2-activated CNF supports (Fig. 3D and figs. S61 and S62). Therefore, the catalytic metabolism-induced particle fission/fusion mechanism for metal alloying at the nanoscale is distinct compared with previously reported alloying methods (*1*, *3*, *7*, *16*).

By tuning the shock duration and heating/cooling rates, we can adjust the MMNP size, distribution, and structure. We loaded multiple CNF samples using an identical PtNi precursor solution and exposed the support to a temperature of ~2000 K for 5-ms, 55-ms, 1-s, and 10-s durations. The faster exposure times yield smaller particle sizes (3.51 ± 0.62 nm for 5 ms and 5.01 ± 1.69 nm for 55 ms) compared with prolonged shock durations (8.57 ± 1.98 nm for 1s and 13.30 ± 6.98 nm for 10 s) (Fig. 4, A and B). We observed similar behavior with AuNi (fig. S63). As the thermal shock

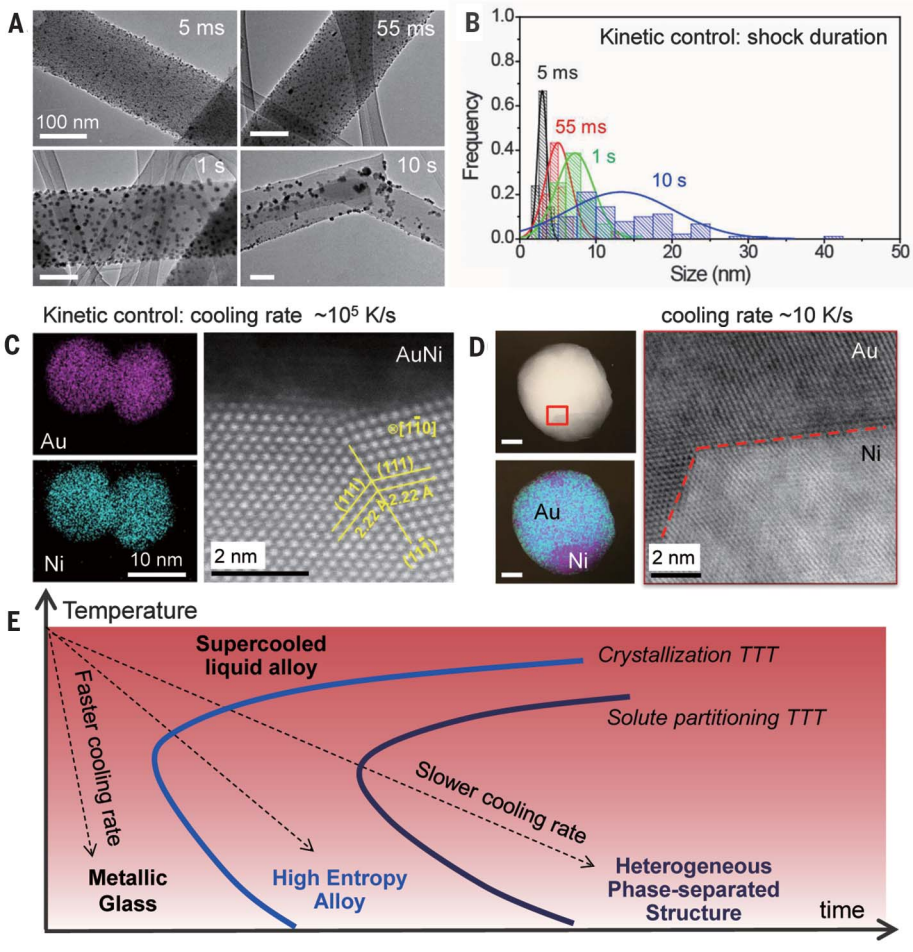

Fig. 4. Kinetic control over nanoparticle formation. (**A**) TEM images displaying the particle size and dispersity at various thermal shock durations (5 ms, 55 ms, 1 s, and 10 s). Scale bars, 100 nm. (**B**) Particle size distribution of PtNi nanoparticles on CNFs. (**C** and **D**) Cooling rate–dependent AuNi nanostructures determined by elemental maps, HAADF, and ABF images. Ultrafast cooling rates (~10^5 K/s) enable the formation of solid-solution nanoparticles, whereas slower rates (~10 K/s) tend to induce phase separation. Scale bar, 10 nm. (**E**) Time-temperature-transformation (TTT) diagram showing the kinetic formation of metallic glass, HEA, and phase-separated structures, respectively, as a function of cooling rate.

Downloaded from http://science.sciencemag.org/ on March 31, 2018

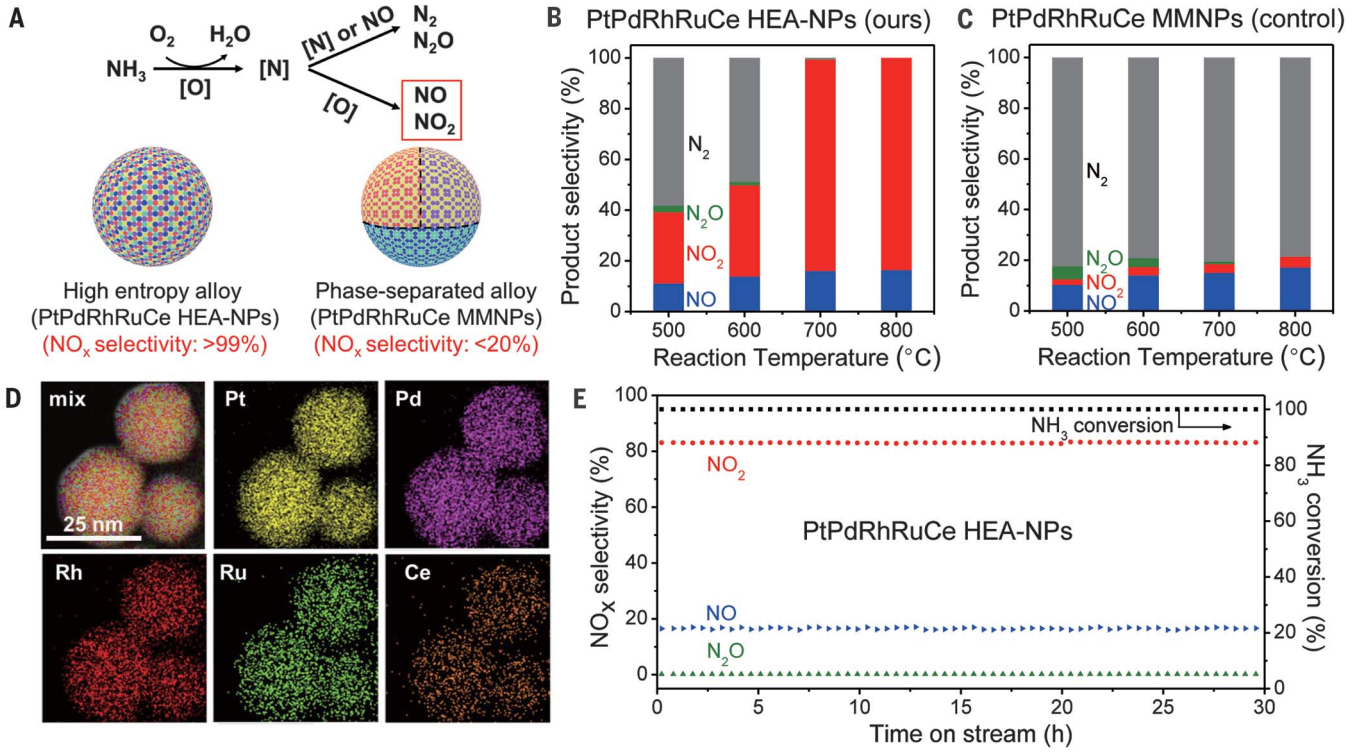

Fig. 5. Catalytic performance of quinary HEA-NPs (PtPdRhRuCe) for ammonia oxidation. (**A**) Reaction scheme for the ammonia oxidation process as well as the structural and performance differences between the PtPdRhRuCe HEA-NPs synthesized by CTS and the control sample (PtPdRhRuCe MMNPs) by wet impregnation. (**B** and **C**) Temperature-dependent product distribution and conversion of NH_3 for PtPdRhRuCe HEA-NPs and PtPdRhRuCe MMNPs, respectively. (**D**) STEM elemental maps for PtPdRhRuCe HEA-NPs. (**E**) The time-dependent catalytic performance of PtPdRhRuCe HEA-NPs at 700°C.

duration increases to 10 s, the size of the HEA-NPs increases and the synthesized particles become less uniform; the high-temperature exposure depletes the number of O* present on the CNF support, which inhibits particle fission and corresponding dispersity (fig. S64).

We investigated the effect of cooling rate by tuning the electrical input parameters (Fig. 1B) with Au/Ni and Cu/Co, which are immiscible binary elemental compositions (Fig. 4, C and D, and figs. S65 to S67). Due to differences in lattice parameters and surface energies, these metallic combinations tend to phase-separate according to equilibrium phase diagrams (*3*, *20*, *31*). However, through rapid quenching, the high-entropy mixing state of the liquid metals is retained and yields single-phase solid-solution nanoparticles (i.e., HEA-NPs) by avoiding the time-temperature-transformation (TTT) nose (Fig. 4E). The AuNi binary alloy formed a solid solution when quenched at both ~10^5 and ~10^3 K/s (Fig. 4C and fig. S66). However, nanoscale phase separation occurred when cooled slowly (~10 K/s), with a clear phase boundary between Au and Ni shown in the annular bright-field (ABF) image (Fig. 4D) and HAADF image (fig. S66). For the CuCo binary system, the 10^5 K/s produced a solid solution, but phase separation began at a cooling rate of ~10^3 K/s (fig. S65). Very slow cooling and heating rates (~10 K/s) also alter the dispersion and size distribution of the synthesized nanoparticles, which leads to aggregates and a nonuniform particle dispersion across the CNFs (figs. S67 and S68).

Our experimental results reveal valuable information about the nucleation and diffusion kinetics of the CTS method. The transformation of a liquid alloy into a single-phase solid solution with a specific elemental composition requires local structural rearrangements but no long-range solute partitioning. The cooling rate (~10^5 K/s) that we achieved by CTS is still slow enough to form crystalline structures. If higher cooling rates are attained with the CTS method, it may be possible to use this route to synthesize metallic glasses. The ~10^5 K/s cooling rate is fast enough to prevent solute partitioning across a distance of ~10 nm, enabling the formation of high-entropy-alloy structures. On the other hand, slower cooling rates (e.g., ~10 K/s) enable solute partitioning to occur through (slow) kinetics, which caused the MMNPs to phase separate into a Janus particle. Both single-phase and phase-separated nanoparticles are useful for applications such as catalysis and plasmonic imaging (*2*, *3*, *9*, *10*). The CTS method has the ability to control phase formation through ramp rates and may be useful for targeted nanoparticle synthesis.

The CTS method enables diverse compositions of uniformly mixed HEA-NPs that have potential for a wide range of applications. As a proof of concept, we demonstrated quinary HEA-NPs as advanced catalysts for ammonia oxidation, which is the key processing step in the industrial synthesis of nitric acid (Fig. 5A) (*32*). Despite extensive efforts on the exploration of new catalysts, PtPdRh-based multimetallic catalysts are still widely employed in industry to this day (*33*). Beyond the high content of precious metals, these catalysts also require very high temperatures (>800°C) to achieve high yields of NO_x (NO + NO_2) versus N_2/N_2O and tend to degrade under continuous operation (*34*). Using the CTS method, quinary PtPdRhRuCe HEA-NPs (figs. S69 and S70 and table S5 for the compositions) were prepared and employed as ammonia oxidation catalysts (*21*). We introduced Ru and Ce to improve the overall catalytic activity and reduce the Pt content (*35*, *36*).

We achieved ~100% conversion of ammonia (NH_3) and >99% selectivity toward NO_x (NO + NO_2) at a relatively low operation temperature of 700°C with the PtPdRhRuCe HEA-NP catalyst (Fig. 5B). For comparison, we prepared similar catalysts (in terms of composition) by the wet impregnation method (denoted as PtPdRhRuCe MMNPs), which produced a 18.7% yield of NO_x at the same operation temperature, whereas most of the output was N_2 (Fig. 5C). An elemental map comparison between the two catalysts suggests that the enhanced catalytic selectivity of the HEA-NPs is likely due to the highly homogeneous nature of the solid-solution nanoparticles compared with the phase-separated heterostructures derived from the wet impregnation method

Downloaded from http://science.sciencemag.org/ on March 31, 2018

(Fig. 5D and fig. S70). Note that synthesizing solid-solution PtPdRh multimetallic systems by conventional synthetic methods is challenging due to immiscibility (*2, 34*). We also performed degradation testing to study catalytic performance under prolonged operation conditions, and we observe no degradation in terms of catalytic activity or selectivity over ~30 hours of continuous operation at 700°C (Fig. 5E and fig. S71). We attributed this durability to the high-entropy nature of the catalysts prepared by the CTS method, which helps stabilize the MMNPs in solid solutions (i.e., HEA-NPs) and prevents phase separation or elemental segregation under the reaction conditions (*16*, *18*). Moreover, the precious metal content of the HEA-NPs can be reduced further without compromising catalytic performance or stability by replacing ~37.5% of Pt with Co and eliminating Ru (e.g., PtPdRhCoCe HEA-NPs) (fig. S72). Thus, HEA-NPs fabricated by the CTS method may be a general route toward highly active, durable, and cost-effective catalysts (see table S6 for a detailed literature comparison).

Discussion and conclusion

The CTS method provides an excellent platform for nanometallurgical studies. Immiscible elements are alloyed into single-phase nanoparticles on carbon supports with the following features: (i) high-entropy mixing, where multimetallic mixing leads to the creation of solid-solution nanoparticles with maximized configurational mixing entropy; (ii) nonequilibrium processing, where the shock process takes milliseconds to create HEA-NPs by rapid quenching and thus prevents phase separation among immiscible elements by avoiding the nose of the TTT curve (Fig. 4E); and (iii) uniform dispersion, where the catalytically driven carbon metabolism at high temperature enables uniform, well-dispersed, and controllably sized nanoparticles (as opposed to particle coarsening).

This synthetic technique also provides (i) generality, (ii) tunability, and (iii) potential scalability. The maximum temperature of the CTS method (2000 to 3000 K) is higher than the decomposition temperature of any metal salt, which promotes uniform mixing of nearly any metallic combination (i.e., generality). Precise control over the shock parameters (temperature, duration, and ramp rates) effectively tunes the particle size, dispersity, as well as final structure. The synthesis of a diverse array of nanoparticles with easily tunable processing parameters is ideal for large-scale nanomanufacturing, where a rapid (synthesis in milliseconds) and energy-efficient (immediate heating through an electrical pulse) synthetic procedure could enable high-rate and high-volume production of quality nanoparticles. Moreover, a scalability evaluation exhibited a 100-fold increase in HEA-NP production without sacrificing nanoparticle quality or dispersion by employing a three-dimensional carbon support (figs. S73 to S75). These CTS capabilities facilitate a new research area for materials discovery and optimization, where the elemental composition and mixing entropy of nanoparticles can be carefully designed and controlled. Further compositional exploration has the potential to transcend research efforts to broad technological applications.

REFERENCES AND NOTES

1. P.-C. Chen *et al*., *Science* **352**, 1565–1569 (2016).
2. L. Bu *et al*., *Science* **354**, 1410–1414 (2016).
3. S. G. Kwon *et al*., *Nat. Mater.* **14**, 215–223 (2015).
4. M. Takahashi *et al*., *Sci. Adv.* **3**, e1700101 (2017).
5. X. Huang *et al*., *Science* **348**, 1230–1234 (2015).
6. G. Chen *et al*., *Science* **344**, 495–499 (2014).
7. M. R. Buck, J. F. Bondi, R. E. Schaak, *Nat. Chem.* **4**, 37–44 (2011).
8. N. A. Frey, S. Peng, K. Cheng, S. Sun, *Chem. Soc. Rev.* **38**, 2532–2542 (2009).
9. M. B. Cortie, A. M. McDonagh, *Chem. Rev.* **111**, 3713–3735 (2011).
10. K. D. Gilroy, A. Ruditskiy, H.-C. Peng, D. Qin, Y. Xia, *Chem. Rev.* **116**, 10414–10472 (2016).
11. E. Reddington *et al*., *Science* **280**, 1735–1737 (1998).
12. P. C. Chen *et al*., *J. Am. Chem. Soc.* **137**, 9167–9173 (2015).
13. P.-C. Chen *et al*., *J. Am. Chem. Soc.* **139**, 9876–9884 (2017).
14. S. Ranganathan, *Curr. Sci.* **85**, 1404–1406 (2003).
15. J.-W. Yeh *et al*., *Adv. Eng. Mater.* **6**, 299–303 (2004).
16. B. S. Murty, J.-W. Yeh, S. Ranganathan, *High-Entropy Alloys* (Butterworth-Heinemann, 2014).
17. Z. Li, K. G. Pradeep, Y. Deng, D. Raabe, C. C. Tasan, *Nature* **534**, 227–230 (2016).
18. Y. F. Ye, Q. Wang, J. Lu, C. T. Liu, Y. Yang, *Mater. Today* **19**, 349–362 (2016).
19. D. C. Hofmann *et al*., *Nature* **451**, 1085–1089 (2008).
20. D. A. Porter, K. E. Easterling, M. Y. Sherif, *Phase Transformations in Metals and Alloys* (CRC Press, ed. 3, 2009).
21. Materials and methods are available as supplementary materials.
22. N. Eustathopoulos, M. G. Nicholas, B. B. Drevet, *Wettability at High Temperatures* (Elsevier, 1999), vol. 3.
23. M. Lukas *et al*., *Nat. Commun.* **4**, 1379 (2013).
24. F. Tao *et al*., *Science* **322**, 932–934 (2008).
25. M. A. Newton, C. Belver-Coldeira, A. Martínez-Arias, M. Fernández-García, *Nat. Mater.* **6**, 528–532 (2007).
26. F. Tao *et al*., *Science* **327**, 850–853 (2010).
27. P.-H. Lu *et al*., arXiv:1802.00207 [physics.app-ph] (1 Feb 2018).
28. N. Combe, P. Jensen, A. Pimpinelli, *Phys. Rev. Lett.* **85**, 110–113 (2000).
29. C. C. Wang *et al*., *Nano Res.* **8**, 2143–2151 (2015).
30. D.-G. Xie *et al*., *Nat. Mater.* **14**, 899–903 (2015).
31. D. Wang, Y. Li, *J. Am. Chem. Soc.* **132**, 6280–6281 (2010).
32. D. M. Considine, *Chemical and Process Technology Encyclopedia* (CRC Press, 1974).
33. L. Xin, H. Yongqiang, J. Husheng, *Rare Met. Mater. Eng.* **46**, 339–343 (2017).
34. P. A. J. Bagot *et al*., *J. Phys. Chem. C* **118**, 26130–26138 (2014).
35. B. V. I. Chernyshov, I. M. Kisil, *Platin. Met. Rev.* **37**, 136–143 (1993).
36. X. Hu, Y. Ning, L. Chen, Q. Shi, C. Jia, *Platin. Met. Rev.* **56**, 40–46 (2012).

ACKNOWLEDGMENTS

The authors thank K. Gaskell and S. Xu, as well as B. Liu, for their help with XPS and XRD measurements/analysis, respectively. The authors acknowledge the use and support of the Maryland NanoCenter and its AIMLab. This work made use of the JEOL JEM-ARM200CF in the Electron Microscopy Service (Research Resources Center, UIC). **Funding:** This work has no direct funding support. The acquisition of the UIC JEOL JEM-ARM200CF was supported by a MRI-R2 grant from the National Science Foundation (NSF) (DMR-0959470). R.S.Y. and J.L. acknowledge financial support from NSF DMR-1620901 and NSF DMR-1410636, respectively. S.D.L. acknowledges support by the Department of Defense through the National Defense Science and Engineering Graduate Fellowship. M.R.Z. and R.J.J. were partially supported by an Office of Naval Research Multidisciplinary University Research Initiative grant. P.X. and C.W. acknowledge the Catalyst and Discovery Awards of Johns Hopkins University. **Author contributions:** L.H. and Y.Y. conceived the idea and designed the present work. Y.Y., S.D.L., H.X., and F.C. carried out the experiments. Z.H., A.N., and R.S.Y. performed detailed microscopic characterizations. P.X., T.P., and C.W. performed the catalytic evaluation. R.J.J., M.R., and M.Z. conducted high-temperature characterization and in situ molecular beam measurements. D.Y. and J.L. developed the mechanism analysis. All authors discussed the results and contributed to the final manuscript. **Competing interests:** The authors declare no competing interests. Provisional patent applications have been applied for through the University of Maryland (62523646 and 62591638). **Data and materials availability:** All data are available in the manuscript and the supplementary materials.

SUPPLEMENTARY MATERIALS

www.sciencemag.org/content/359/6383/1489/suppl/DC1
Materials and Methods
Supplementary Text
Figs. S1 to S75
Tables S1 to S6
References (*37–47*)

28 April 2017; resubmitted 14 December 2017
Accepted 2 February 2018
10.1126/science.aan5412

Downloaded from http://science.sciencemag.org/ on March 31, 2018

Science

Carbothermal shock synthesis of high-entropy-alloy nanoparticles

Yonggang Yao, Zhennan Huang, Pengfei Xie, Steven D. Lacey, Rohit Jiji Jacob, Hua Xie, Fengjuan Chen, Anmin Nie, Tiancheng Pu, Miles Rehwoldt, Daiwei Yu, Michael R. Zachariah, Chao Wang, Reza Shahbazian-Yassar, Ju Li and Liangbing Hu

Science **359** (6383), 1489-1494.
DOI: 10.1126/science.aan5412

Nanoparticle synthesis gets a shock

Nanoparticles are useful in a wide range of applications such as catalysis, imaging, and energy storage. Yao *et al.* developed a method for making nanoparticles with up to eight different elements (see the Perspective by Skrabalak). The method relies on shocking metal salt-covered carbon nanofibers, followed by rapid quenching. The "carbothermal shock synthesis" can be tuned to select for nanoparticle size as well. The authors successfully created PtPdRhRuCe nanoparticles to catalyze ammonia oxidation.

Science, this issue p. 1489; see also p. 1467

ARTICLE TOOLS http://science.sciencemag.org/content/359/6383/1489

SUPPLEMENTARY MATERIALS http://science.sciencemag.org/content/suppl/2018/03/28/359.6383.1489.DC1

RELATED CONTENT http://science.sciencemag.org/content/sci/359/6383/1467.full

REFERENCES This article cites 41 articles, 9 of which you can access for free
http://science.sciencemag.org/content/359/6383/1489#BIBL

PERMISSIONS http://www.sciencemag.org/help/reprints-and-permissions

Use of this article is subject to the Terms of Service

Science (print ISSN 0036-8075; online ISSN 1095-9203) is published by the American Association for the Advancement of Science, 1200 New York Avenue NW, Washington, DC 20005. 2017 © The Authors, some rights reserved; exclusive licensee American Association for the Advancement of Science. No claim to original U.S. Government Works. The title *Science* is a registered trademark of AAAS.

Downloaded from http://science.sciencemag.org/ on March 31, 2018

NANOMATERIALS

Mashing up metals with carbothermal shock

Many elements can be combined in the formation of high-entropy-alloy nanoparticles

By **Sara E. Skrabalak**

Different materials and the capabilities they enabled have marked the ages of civilization. For example, the malleable copper alloys of the Bronze Age provided harder and more durable tools. Most exploration of new alloys has focused on random alloys, in which the alloying metal sites have no metal preference. In binary and ternary metal systems, dissimilar elements do not mix readily at high concentrations, which has limited alloying studies to intermetallics (ordered multimetallic phases) and random alloys, in which minor components are added to a principal element. In 2004, crystalline metal alloys consisting of five or more principal elements in equal or nearly equal amounts (*1*, *2*) were reported that were stabilized by their high configurational entropy. Unlike most random alloys, the "high-entropy" alloys (*3*, *4*) reside in the centers of their multidimensional phase diagrams (see the figure, right). On page 1489 of this issue, Yao *et al.* (*5*) present an innovative and general route to high-entropy alloys that can mix up to eight elements into single-phase, size-controlled nanoparticles (NPs).

High-entropy alloys usually have a minimum of five elements in nearly equal proportions. Synthesis of these compositions is challenging and not typically compatible with methods that yield well-defined nanoparticles. Such integration would enable the nanoscale properties of these complex compositions to be studied and potentially leveraged in diverse applications. For example, high-entropy alloys are being studied as structural materials and for their superparamagnetic and superconducting properties (*4*).

High-entropy alloys were initially synthesized through high-temperature melting or plasma routes that could produce atomically mixed phases before solidification (*1*, *3*). By contrast, nanoscale alloys are often made in solution by co-reducing metal salts along with capping agents that control crystal growth and aggregation (*6*, *7*). However, the compositional space of such alloys is often limited because the precursors react at different rates (*8*). The high surface energy of NPs can be exploited to access new metal phases, but only simple compositions have been reported (*9*). Even recent printing methods for synthesizing multimetallic NPs yield phase-segregated multicomponent NPs when the input composition becomes too complex (*10*, *11*). This observation is consistent with varied precursor reactivity and slow cooling rates.

By electrically shocking mixed-metal salt precursors dispersed on conductive carbon supports, Yao *et al.* accessed high-entropy alloys as size-controlled NPs. This method provided the high reaction temperatures (~2000 K) and rapid heating and cooling rates (~10^5 K/s) necessary for high-entropy-alloy formation, while the underlying carbon support inhibited coalescence of the NPs. Conveniently, the input ratio of metal was replicated in the final product, and the method is scalable.

The NP size could be tuned through the shock conditions. Interestingly, phase segregated multicomponent NPs were produced by slowing the cooling rate to facilitate diffusion and partitioning of the solutes. This observation gives insight into the formation mechanism of high-entropy alloyed NPs, in which a mixed phase must be achieved before solidification and then preserved through cooling at an optimal rate so that neither phase separation nor glass formation occurs (see the figure, left). This observation also suggests that this approach could yield new types of nanoscale heterostructures with further development.

Distinctive properties can emerge when new alloys undergo electron confinement at the nanoscale materials. For example, Yao *et al.* showed that their PtPdRhRuCe NPs were effective catalysts for ammonia oxidation, and this synthetic approach has the potential to yield additional new catalysts. An exceptionally high number of possible compositions and nanostructures can be envisioned, which introduces some fundamental challenges (*4*). In particular, identification of high-entropy alloys with useful properties by trial-and-error methods is unsatisfactory given the large phase space. High-throughput characterization of composition, nanoscale features, and properties are critically needed (*12*, *13*). These advances should be coupled with theory so that a deeper understanding of phase formation and the emergence of new properties can be achieved and enable materials by design. ■

Nanoscale high-entropy alloys

The synthesis route of Yao *et al.* makes mixtures of many elements.

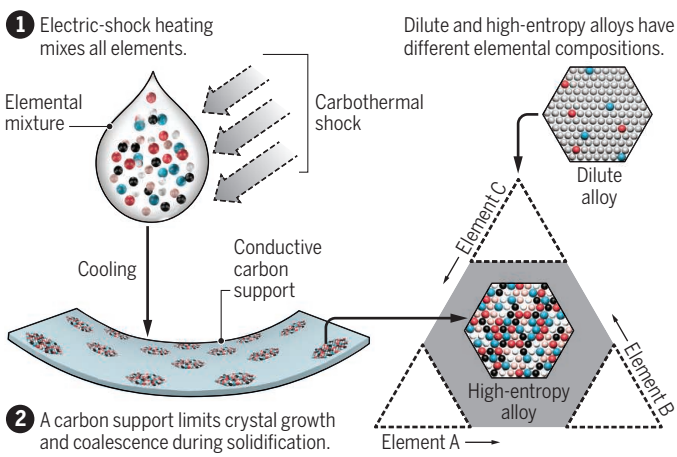

GRAPHIC: A. KITTERMAN/*SCIENCE*

Chemistry Department, Indiana University–Bloomington, 800 East Kirkwood Avenue, Bloomington, IN 47405, USA. Email: sskrabal@indiana.edu

REFERENCES

1. J.-W. Yeh *et al.*, *Adv. Eng. Mater.* **6**, 299 (2004).
2. B. Cantor, I. T. H. Change, P. Knight, A. J. B. Vincent, *Mater. Sci. Eng. A* **375–377**, 213 (2004).
3. D. B. Miracle, O. N. Senkov, *Acta. Mater.* **122**, 448 (2017).
4. Y. F. Ye, Q. Wang, J. Lu, C. T. Liu, Y. Yang, *Mater. Today* **19**, 349 (2016).
5. Y. Yao *et al.*, *Science* **359**, 1489 (2018).
6. R. Ferrando, J. Jellinek, R. L. Johnston, *Chem. Rev.* **108**, 845 (2008).
7. K. D. Gilroy, A. Ruditskiy, H.-C. Peng, D. Qin, Y. Xia, *Chem. Rev.* **116**, 10414 (2016).
8. N. Ortiz, R. G. Weiner, S. E. Skrabalak, *ACS Nano* **8**, 12461 (2014).
9. V. F. Puntes, K. M. Krishnan, P. Alivisatos, *Appl. Phys. Lett.* **78**, 2187 (2001).
10. P.-C. Chen *et al.*, *Science* **352**, 1565 (2016).
11. P.-C. Chen *et al.*, *J. Am. Chem. Soc.* **137**, 9167 (2015).
12. M. A. Payne, J. B. Miller, A. J. Gellman, *ACS Comb. Sci.* **18**, 559 (2016).
13. S. Ding, Y. Liu, Y. Li, Z. Liu, S. Sohn, F. J. Walker, J. Schroers, *Nat. Mater.* **13**, 494 (2014).

10.1126/science.aat1471

Downloaded from http://science.sciencemag.org/ on March 31, 2018

Published by AAAS

Science

Mashing up metals with carbothermal shock

Sara E. Skrabalak

Science **359** (6383), 1467.
DOI: 10.1126/science.aat1471

ARTICLE TOOLS http://science.sciencemag.org/content/359/6383/1467

RELATED CONTENT http://science.sciencemag.org/content/sci/359/6383/1489.full

REFERENCES This article cites 13 articles, 2 of which you can access for free
http://science.sciencemag.org/content/359/6383/1467#BIBL

PERMISSIONS http://www.sciencemag.org/help/reprints-and-permissions

Use of this article is subject to the Terms of Service

Science (print ISSN 0036-8075; online ISSN 1095-9203) is published by the American Association for the Advancement of Science, 1200 New York Avenue NW, Washington, DC 20005. 2017 © The Authors, some rights reserved; exclusive licensee American Association for the Advancement of Science. No claim to original U.S. Government Works. The title *Science* is a registered trademark of AAAS.

Downloaded from http://science.sciencemag.org/ on March 31, 2018

www.sciencemag.org/content/359/6383/1489/suppl/DC1

Supplementary Materials for

Carbothermal shock synthesis of high-entropy-alloy nanoparticles

Yonggang Yao,* Zhennan Huang,* Pengfei Xie,* Steven D. Lacey,* Rohit Jiji Jacob, Hua Xie, Fengjuan Chen, Anmin Nie, Tiancheng Pu, Miles Rehwoldt, Daiwei Yu, Michael R. Zachariah, Chao Wang,† Reza Shahbazian-Yassar,† Ju Li,† Liangbing Hu†

*These authors contributed equally to this work.
†Corresponding author. Email: binghu@umd.edu (L.H.); rsyassar@uic.edu (R.S.-Y.); liju@mit.edu (J.L.); chaowang@jhu.edu (C.W.)

Published 30 March 2018, *Science* **359**, 1489 (2018)
DOI: 10.1126/aan5412

This PDF file includes:

Materials and Methods

Carbon nanofibers (CNF) and metal precursor loading

Electrospun polyacrylonitrile (PAN) fibers were carbonized to create a carbon nanofiber (CNF) support for the carbo-thermal shock (CTS) experiments reported herein. PAN was purchased from Sigma-Aldrich and dissolved in dimethylformamide (DMF) with a concentration of 8wt% before electrospinning at a voltage of 15 kV, a spinning distance of 10 cm, and a feed rate of 1 mL/hour. The electrospun fibers were collected on a rotating drum (speed of 80 rpm). The PAN nanofibers were first stabilized at 533K for 5 hours in air and then carbonized at various temperatures (873 K, 1073 K, 1273 K) for 2 hours in argon. Although the CNF-873K has a higher defect concentration to disperse nanoparticles, the sample requires a higher voltage and power to induce CTS (sometimes beyond the external power source's voltage/power limit depending on the sample's size). CNF-1273K is highly crystalline (less defects) and demonstrates poor nanoparticle dispersion capabilities. CNF-1073K acted as the ideal carbon support in this study due to its defect density for nanoparticle dispersion and ease of applying an electrical pulse within the limits of the external power source. In this work, CNF-1073K is the carbon support used unless stated otherwise.

For aqueous precursor solutions, the CNF films were dipped into the mixed metal salt solutions (0.01 mol/L for each element), placed under vacuum for 30 minutes, and then suspended in a 60°C oven to dry. For ethanol-based precursor solutions, the mixed solutions (0.05/n mol/L for each element, where n is the total number of elements) were directly dropped onto the suspended CNF film with a loading of ~120 $\mu L/cm^2$ and left to dry at room temperature. In general, the ethanol-based solutions result in more uniform loading (and particle dispersion) owing to improved wettability to carbon. These precursor-loaded CNF films were used directly for the rapid, high temperature CTS method.

Rapid, high temperature CTS method

The CTS process was achieved by electrically-triggered Joule heating of precursor-loaded CNF films in an argon-filled glovebox. The aforementioned samples were suspended on glass slides by connecting each CNF film to two copper electrodes with silver paste. A Keithley 2425 SourceMeter acted as the external power source with a temporal resolution down to 1 ms and a current source up to 3.15 A. A thermal shock was applied to the CNF film using the sweep function from Keithley where the magnitude (temperature), duration (thermal shock time) and speed (ramp rate) of the electrical pulse are adjustable. A 55 ms electrical pulse was chosen as the ideal thermal shock duration and used to synthesize multimetallic nanoparticles in this work (unless noted otherwise). In short, this is due to the fact that a faster thermal shock (i.e. 5 ms) may result in partial lighting of the CNF sample due to the extremely short duration under high temperature. In this case, there is a limited amount of time for heat to dissipate throughout the entire sample, while longer heating durations (i.e. 1 s or longer) can result in larger particles due to slower kinetics and enhanced particle aggregation due to the prolonged time under high temperature.

Spectrum collection and fitting

Instead of using photodiodes or charge-coupled devices to capture the spectrum, a specifically designed, time-resolved pyrometer was used to capture the emitted light from

the sample during high temperature exposure (in operando) and deduce the ultrafast heating/cooling rates (schematic in Fig. S5). The system employs a 0.5 m spectrometer with a dynamic choice of 150, 600 and 1200 grooves/mm gratings that can disperse light at a resolution of 6.5, 3.2, and 0.8 nm/mm, respectively. The dispersed light is collected by a 32-channel photomultiplier tube (PMT) array, allowing examination over bandwidths of approximately 200 nm, 100 nm or 30 nm. The system offers a temporal resolution as low as 2.5 μs, enabling us to capture the fast switching process by the applied electrical pulse. The emission spectrum was captured by a 32-channel PMT and then fitted to the blackbody radiation equation (Eq. 1) to obtain a fitted parameter, T, which is a close approximation to the actual temperature reached during CTS:

$$B_\lambda(\lambda, T) = \gamma \frac{2hc^2}{\lambda^5} \frac{1}{e^{hc/\lambda k_B T} - 1} \quad \text{(Eq. 1)}$$

where k_B is the Boltzmann constant, h is the Planck constant, c is the speed of light, λ is the wavelength, and γ is a constant introduced for the fitting. Although carbon allotropes are not ideal blackbody materials, they show a stable emissivity in the measured wavelength range, which ensures the fitting accuracy.

Structural characterization

The microstructure and morphology of the prepared samples was observed by a scanning electron microscope (SEM) (Hitachi SU-70 FEG-SEM at 10 kV) and transmission electron microscopes (TEM) (JEOL 2100F FEG TEM/STEM operated at 200 kV, and JEOL TEM/STEM ARM 200CF equipped with high angle annular dark field (HAADF) and annular bright field (ABF) detectors). A 22 mrad probe convergence angle was used to perform STEM imaging. High angle annular dark field (HAADF) images were acquired using the JEOL ARM 200CF with a 90 mrad inner-detector angle. An Oxford X-max 100TLE windowless X-ray detector was used to collect the energy dispersive spectra (EDS).

Macroscopically, Raman measurements were performed on a Horiba Jobin-Yvon using a 532 nm laser and an integration time of 4 s (repeated 4 times). XPS was performed on a Kratos Axis 165 x-ray photoelectron spectrometer and analyzed by the CasaXPS software. X-ray diffraction (XRD) was performed using a D8 Advanced (Bruker AXS, WI, USA) with a scan rate of 3°/min. The metal contents of the CNF supported HEA-NPs were analyzed by inductively coupled plasma mass spectroscopy (PerkinElmer NexION 300D ICP-MS). The solutions were prepared by digesting the samples in aqua regia followed by dilution with 2% hydrochloric acid (HCl). The resultant solutions were analyzed directly by ICP-MS.

Catalytic ammonia oxidation tests

Catalytic oxidation of NH_3 was conducted in a fixed-bed flow reactor at atmospheric pressure. Typically, 10 mg of catalyst mixed with Al_2O_3 particles (40-60 mesh) was loaded into a quartz tube reactor (7 mm = inner diameter). The catalyst was heated to 500°C at a rate of 5°C/min under He (50 mL/min). At 500°C, the gas flow was switched to a forming gas containing 1% NH_3 and 2% O_2, balanced by He. The space velocity was adjusted to 120 L /(g_{cat}·h) by tuning the flow rate. The reaction was then carried out at various temperatures, which was increased stepwise from 500°C to 800°C. Note that a steady state

was reached before the product analysis. To determine the conversion of reactants and the yield of products, a FTIR spectrometer (Nicolet 6700, Thermo Scientific) equipped with a long path (5 m) gas cell and a MCT detector (with a resolution of 8 cm^{-1}) was used to analyze NH_3 (964 cm^{-1}), NO (1905 cm^{-1}), N_2O (2237 cm^{-1}), and NO_2 (1630 cm^{-1}). N_2 was detected via a gas chromatograph (GC) equipped with a BID detector (GC-2010 plus, Shimadzu) and a HP-POLT Molesieve column. The NH_3 conversion and product selectivities were calculated using the following equations:

$$NH_3 \text{ conversion} = \frac{[NH_3]_{inlet} - [NH_3]_{outlet}}{[NH_3]_{inlet}} \times 100\%$$

$$\text{Product selectivity (\%)} = \frac{\delta \times [\text{Product}]_{outlet}}{[NO]_{outlet} + [NO_2]_{outlet} + 2[N_2]_{outlet} + 2[N_2O]_{outlet}} \times 100\%$$

where $[NH_3]_{inlet}$ refers to the concentration of NH_3 fed into the reactor, and $[NH_3]_{outlet}$, $[NO]_{outlet}$, $[NO_2]_{outlet}$, $[N_2]_{outlet}$, and $[N_2O]_{outlet}$ refer to the corresponding species concentrations measured from the outflow of the reactor. In terms of product selectivity, δ = 1 for NO and NO_2, while δ = 2 for N_2 and N_2O.

Supplementary Text

Starting materials

Electrospun polyacrylonitrile (PAN) derived carbon nanofibers carbonized at 1073 K were used for this study unless otherwise noted. The carbon nanofiber (CNF) fiber mat shows uniform nanofibers (200-300 nm in diameter) with an open network structure as revealed by SEM (Fig. S1).

The CNF carbonization temperature is a very important processing parameter and also critically important for the nanoparticle size and dispersion via the CTS method. When the carbonization temperature is increased, the unstable defects are removed from the CNF, leading to higher crystallinity, higher conductivity, and lower defect concentrations. Fig. S2 studies the effect of carbonization temperature on the resultant CNF film's properties. Fig. S2a shows the Raman spectra for the carbonized CNFs. The broad D peak and G peak are indications of the disordered bonds and defects present in the prepared CNFs. Note that the D peak decreases as the carbonization temperature increases, which indicates the removal of defects during carbonization. It is also clear that increasing the carbonization temperature, increases the conductivity substantially due to a higher degree of crystallinity in the CNFs (Fig. S2b). Point mapping was used to identify the carbon content of the CNF films carbonized at different temperatures. Fig. S2c shows the increase of carbon content and removal of defects as the carbonization temperature increases. Fig. S2d is an elemental map (carbon, nitrogen, oxygen) of the CNF-1073K sample. XPS results show that the CNF-1073K sample has clear N and O defect peaks with a distribution of ~20%, confirming the existence of defects in the low temperature carbonized CNFs. From our experiments, CNF-1073K is the ideal carbon support for the CTS process due to its suitable resistance and defect density.

Microstructures before and after the CTS process

To effectively load the aqueous precursor salts onto the carbon support, we immersed the CNFs in a precursor solution and applied vacuum to assist the loading. For low element systems (1-3), a higher concentration of 0.05 mol/L led to more particles on the CNFs as shown in Fig. S3. After the 55 ms thermal shock, these crystallized and microsized precursors were decomposed and dispersed into uniformly sized and well-dispersed nanoparticles on the CNF sample.

We show the HAADF-STEM image and STEM elemental maps for the PtNi nanoparticles at low magnifications as well as for an individual nanoparticle (Fig. S4). Each magnification demonstrates uniform mixing of PtNi without phase or elemental segregation. This confirms alloy formation by CTS.

Ultrafast Joule heating setup and characterization

The precursor-loaded CNF sample was suspended on a glass substrate to avoid both sample contamination and damage to the substrate due to the high temperature CTS process. The sample was connected to copper electrodes by silver paste and an electrical pulse (i.e. an applied current) was applied to induce Joule heating. The spectrum collection was performed on a specifically designed online pyrometer (Fig. S5). Further details

regarding the setup and functions were described in the aforementioned Methods section. Briefly, the system employed a 0.5 m spectrometer (Sp-500i) with a dynamic choice of 150, 600 and 1200 grooves/mm gratings that can disperse light at a resolution of 6.5, 3.2, and 0.8 nm/mm. The dispersed light was collected by a 32-channel PMT array (H-7260), where the temporal spectra can be integrated and plotted as a function of time. By fitting the full spectrum collected at a specific time to the blackbody radiation equation (Eq.1), the fitted parameter T (i.e. approximate sample temperature) can be approximated. Note that the system offers a temporal resolution as low as 2.5 μs, which enables us to capture the fast switching process from the electrical pulse.

The collected spectra for the CTS method at shock durations of 55 ms and 5 ms are shown in Fig. S6. The 55 ms shock shows three steps: instant heating (i.e. a rapid heating rate), duration at high temperature, and fast cooling. Based on the temporal temperature profile for the 5 ms thermal shock, the heating/cooling process is nearly instantaneous (~10^5 K/s). This fast heating/cooling rate is rarely realized in conventional nanoparticle synthesis methods and provides some material/processing benefits: (i) carbon nanomaterials have a large surface to volume ratio that allows rapid heat dissipation; (ii) electrically-triggered Joule heating can have a temporal resolution down to milliseconds.

By using a high-speed video camera, we were able to capture the spatial temperature evolution in the CNF-based sample during a 55 ms CTS (Fig. S7). The sample showed relatively uniform lighting in the chamber reaching a temperature of ~2000 K.

Configurational entropy of mixing

The configurational entropy of mixing for multielement nanoparticles can be calculated according to following equation (Eq. 2) *(16)*:

$$\Delta S_{mix} = -R \sum_{i=1}^{n} X_i ln X_i \qquad \text{(Eq. 2)}$$

where ΔS_{mix} is the configurational entropy of mixing, R is the gas constant, X_i is the molar ratio of component i, and n is the total number of elements involved. As shown in Fig. S8, the maximum mixing entropy (random mixing in an equal ratio) shows a well-defined sublinear relationship; as the amount of alloying elements increases, the mixing entropy (ΔS_{mix}) also increases in a logarithmic fashion: from low entropy (ΔS_{mix} <1R) for unary and binary alloys, to medium entropy (1R< ΔS_{mix} <1.5R) for ternary and quaternary alloys, and high entropy alloys (ΔS_{mix} >1.5R), according to the classifications in high entropy alloys research *(16)*. The majority of conventionally synthesized nanoparticles are composed of a limited number of elements and thus, fall into the category of low entropy alloys. The top-down assembly processes (dip-pen lithography) can mechanically confine nanoparticles composed of 5 elements however, phase separation occurs within the MMNPs which drastically decreases their mixing entropy. By utilizing the CTS process, multimetallic mixing of numerous elements (up to 8) can be readily achieved, pushing the synthesis capabilities towards the high entropy region. Note that the term “high entropy alloy nanoparticles” (HEA-NPs) in this work denotes solid solution structures since the high entropy mixing liquid metal state is retained by rapid quenching. Thus, our definition of HEA-NPs is not directly dependent on the number of elemental constituents.

Microstructures of HEA-NPs

TEM images show the size distribution of nanoparticles synthesized by the carbo-thermal shock (CTS) method for Pt, PtNi, and PtPdNi (Fig. S9). The TEM images of high entropy mixing alloy nanoparticles (5-8 elements) are shown in Fig. S10.

STEM-EDS Spectra for HEA-NPs

We have collected the STEM elemental spectrum for HEA-NPs (Fig. S11-S16). Also, the EDS spectrum for an octonary HEA-NP (PtPdCoNiFeAuCuSn) confirms that the Cl present in the formed NP is negligible (Fig. S16). The full STEM spectrum and enlarged portion indicate that Cl is under the detection limit (<0.1%), which confirms the decomposition of Cl-based salts and the formation of metallic alloys by the high temperature CTS process.

Atomic structure analysis for HEA-NPs

The detailed atomic HAADF structure images are illustrated in Fig. S17. The atomic scale HAADF image for a PtNi nanoparticle (Fig. S17a) was determined to be along the [1-10] zone axis. The *d*-spacing of the two main lattice planes was measured to be 2.24 Å, which is nearly identical to the {111} planes of the FCC Pt metal crystal structure (Fm-3m, $a=b=c=$ 3.878, JCPDF 87-0647). The atomic scale HAADF image for the FeCoNi particle (Fig. S17b) was determined to be along the [001] zone axis. The *d*-spacing of the two vertical lattice planes was measured to be 1.78 Å, which represents the {200} planes of the FCC Co metal crystal structure (Fm-3m, $a=b=c=$ 3.544, JCPDF 15-0806). The atomic scale HAADF image for the octonary nanoalloy (Fig. S17c) corresponds to a [1-10] zone axis. Similarly, the d-spacing between the two lattice planes was 2.20 Å, indicative of the {111} planes of the FCC Pt metal crystal structure (JCPDF 04-0802). The corresponding EDS elemental maps also show that Pt encompasses a higher atomic percentage of the synthesized nanoparticle. Notably, consecutive twin boundaries (marked as a red arrow in the Fig. S17c) exist along the {111} planes. However, these defects may be beneficial as electro-catalytically active sites.

Fast Fourier Transform (FFT) analysis has also been performed on the twin boundary area (Fig. S18a). Three different sites along the twin boundaries marked with 1-purple, 2-blue, 3-green squares, respectively. Their corresponding FFT patterns show the FCC {111} planes and indicate that a single crystal FCC structure has been formed. The extra spots in the overlapped pattern correspond to the FCC {111} planes with twin boundaries. A higher magnification atomic HAADF image with FFT analysis for octonary HEA-NPs (PtPdCoNiFeAuCuSn) also shows a single-phase structure with the planes corresponding to the FCC [1-10] zone axis (Fig. S18b). In this case, the well-mixed nanoparticle consisting of 8 elements is single crystalline. As the eight elements are uniformly distributed in each atom column, which has been revealed by atomic EDS mapping, these elements are overlayed within the atomic columns, resulting the similarity in the scattering intensity.

Solid solution formation in HEA-NPs

1. Individual elemental mapping of nanoparticles:

As provided in the main text (Fig. 1C and Fig. 2C), the HAADF-STEM images, as well as the elemental overlay maps, confirm the formation of alloys without phase separation.

We also performed point-by-point EDS analysis on individual nanoparticles to demonstrate complete miscibility instead of elemental segregation. The point analysis on two individual particles (quinary PtPdCoNiFe) at each corner and at the center (5 points for each particle) exhibit a small compositional variation (<10%) at different sites, indicating the uniform distribution and solid solution formation throughout the HEA-NP (Fig. S19).

As a comparison, quinary MMNPs (AuAgCoNiCu) synthesized using scanning-probe block copolymer lithography (Science 352, 1565–1569 (2016))(*1*) results in near-equilibrium structures, where the metals immiscibility results in obvious phase separation. This behavior is drastically different from the high entropy solid solution MMNPs (i.e. HEA-NPs) synthesized by CTS.

2. Atomic-level characterization:

To verify the atomic level mixing of HEA-NPs with higher complexity (>2 and up to 8 elements), we obtained atomic resolution elemental maps (Fig. S20). On an atomic scale, the PtNi particle consists of FCC crystals with an even elemental distribution of Pt and Ni, confirming alloy formation of solid solution PtNi using our CTS method. This is also the case for AuCu and FeCoNi.

We also performed atomic scale analysis on an octonary HEA-NP (PtPdCoNiFeAuCuSn) (Fig. S21). The atomic maps demonstrate an even elemental distribution and formation of a solid solution composed of up to 8 dissimilar metals. Note that in the octonary HEA-NPs, each element has a much lower concentration and thus, the individual maps are not as clear for each atomic configuration.

Structural uniformity throughout the sample

Additional low magnification elemental maps at different sample areas for binary (PtNi), quinary (PtPdCoNiFe) and octonary (PtPdCoNiFeAuCuSn) HEA-NPs. However, it should be noted that at low magnifications, the quality of the STEM elemental maps degrades due to signal dilution for each element. The reasons are twofold: (1) the majority of the signal arises from the substrate (C, N, O) at low magnifications and (2) each nanoparticle is composed of 5-8 elements, which further dilutes the intensity of each element.

1. Low magnification STEM maps for binary PtNi:

Here we show the STEM elemental map for a binary (PtNi) alloy both at low magnification and higher magnification (i.e. only a few nanoparticles) (Fig. S22). Similar to the individual nanoparticle maps, each element remains uniformly distributed throughout each nanoparticle without obvious elemental isolation or segregation at both low and high magnifications. The result confirms the formation of alloy structures over a wide sample region.

2. Low magnification STEM maps for quinary HEA-NPs:

The following are low magnification STEM elemental maps for quinary HEA-NPs (PtPdCoNiFe) over a range of sample areas (Fig. S23). Every element is uniformly distributed throughout each nanoparticle without obvious elemental isolation or segregation. The uniform elemental distribution is consistent even at different sample regions. Thus, the formation of solid solution alloys is confirmed.

3. Low magnification STEM maps for octonary HEA-NPs:

The low magnification elemental maps for octonary HEA-NPs (PtPdCoNiFeAuCuSn) also show homogeneous elemental mixing within the mapped sample regions (Fig. S24).

4. STEM elemental maps on several individual nanoparticles:

The STEM elemental maps for several individual nanoparticles with better resolution (Fig. S25). Quinary HEA-NPs (PtPdCoNiFe) synthesized by the same 55 ms thermal shock at ~2000 K also formed a high entropy alloy structure. The elements are uniformly distributed throughout the nanoparticles, which confirms the formation of solid solutions by the CTS method.

For octonary HEA-NPs (PtPdCoNiFeAuCuSn), there are a lot of immiscible metal combinations, for example: Pt/Pd, Au/Pt, Au/Co, Au/Ni, *etc*. By conventional slow reduction steps, these immiscible combinations usually result in phase-separated heterostructures. In our CTS process, these immiscible elements can be formed into solid solution nanoparticles (i.e. HEA-NPs) by retaining the high entropy mixing liquid metal state (Fig. S26).

In short, the aforementioned STEM elemental maps of HEA-NPs at low magnifications and different sample regions prove both the formation and uniformity of the alloy structures synthesized by our CTS method.

XRD analysis

The determination of macroscopic structure uniformity was performed by XRD analysis. The XRD data for the binary PtNi system agrees well with reports in the literature. Our CTS method allows the synthesis of unrealized HEA-NP structures composed of completely immiscible elements. Since these HEA-NPs composed of 5-8 elements are synthesized for the first time in our work, there are no XRD standards in literature or in the XRD library to reference/compare to.

1. XRD profile of PtNi nanoparticles synthesized by our CTS method:

The SEM image of PtNi dispersed on CNF demonstrates size uniformity on a micrometer scale (Fig. S27a). The XRD profile of PtNi is shown and compared to the standard XRD peaks of Pt and Ni, respectively (Fig. S27b). Note that the single peak at 40°-41° corresponds to the (111) of PtNi as compared with the individual Pt and Ni standard peaks. The broad peak at 42.5° corresponds to the (100) of the CNF substrate. The (220) plane for PtNi is also visible in the XRD profile.

2. XRD profiles of quinary and octonary HEA-NPs synthesized by our CTS method:

The SEM images of quinary HEA-NPs and octonary HEA-NPs prove the uniform dispersion of these HEA-NPs on the micrometer scale (Fig. S28a and S29a). For quinary and octonary HEA-NPs, the XRD peaks are relatively weak and broad due to the elemental complexity of the synthesized solid solution particles (Fig. S28b and S29b). Regardless,

no noticeable secondary peaks were detected. The XRD peak within 41°-43° indicates that the synthesized structures are single-phase solid solutions instead of several separate intermetallic compounds with various structures. Both the microscopy and XRD results confirm uniformity of particle dispersion and structure on a micrometer/millimeter scale.

XPS analysis

The XPS analysis was performed on the 8 elements (PtPdCoNiFeAuCuSn) on CNFs before and after the CTS process (Fig. S30-S36). The characteristic peaks of Cl become negligible after the CTS process, indicating nearly complete precursor salt decomposition and the release of (gaseous) chlorine from the system. In the individual peak fitting, Fe is not specifically analyzed since the peak overlaps with Co.

Note that the characterization depth of XPS is about 5 nm, which is only on the top surface of the CNF film. For the elemental composition ratios, we will not specifically use XPS to verify the ratio. Instead, macroscopic ICP-MS and microscale STEM elemental maps were employed to determine the compositional ratios.

Ethanol-based precursor solutions

Initially, we used precursors dissolved in water as the precursor solutions. While the precursors are relatively uniform throughout the mapped region, there are several aggregates corresponding to the individual (Au and Pt) precursors (Fig. S37). These aggregates can cause compositional inhomogeneity throughout the sample. For a more precise precursor loading, we utilized ethanol to disperse the salt precursors since it has complete wettability with carbon. This approach will ensure uniform final nanoparticle compositions.

Fig. S38 displays the ethanol-based precursor solutions as well as SEM images of the (8 element) precursor-loaded CNFs. By microscopy, the precursor loading on the CNF film is confirmed to be uniform on a microscale level due to the lack of aggregates.

The SEM EDS maps for the precursor-loaded CNF films show uniform distributions of eight elements at different length scales: micrometers to hundreds of nanometers (Fig. S39). Through microscopy and elemental mapping, no obvious metal precursor aggregation/segregation can be identified across the fiber network. Thus, the precursor loading is uniform across the substrate, which is critical to well-distributed and compositionally accurate nanoparticles. Note that the SEM-EDS mapping confirms the uniform distribution of precursors at least on a micrometer scale without obvious aggregates or the existence of secondary structures.

We also performed XRD on the octonary precursors (Fig. S40). Based on the XRD results, the spectra displays sharp peaks that correspond to the specific salt precursors. Notably, the single peak at 16°-18° shows no peak splitting, which indicates uniform mixing of the precursors onto the CNFs. Typically XRD has a spot size on a millimeter scale. The XRD results for the precursor-loaded CNFs indicate that the precursors are uniformly loaded on a millimeter scale without obvious aggregates or the existence of secondary structures.

Compositional uniformity throughout the sample

We have carefully evaluated the elemental variation from one particle to the next within a given sample. The compositional variations are significantly smaller compared to the previous report (Science 352, 1565, 2016) *(1)*. A brief summary of the compositional variation for different HEA-NPs is shown below with a more detailed discussion afterward:

- Binary alloy (PtNi) varies ~5% among NPs at different regions;
- Quinary HEA-NP (PtPdCoNiFe) varies ~10% among NPs at different regions;
- Octonary HEA-NP (PtPdCoNiFeCuAuSn) varies ~10-20% at different regions.

1. Elemental variations among quinary HEA-NPs:

For each sample region, we verified the compositional distribution of the nanoparticles on both an individual level as well as at low magnification. The composition of nanoparticles within the mapped region is statistically uniform, with only minor variations (Fig. S41). Across different sample regions, the variations become slightly larger compared to the nanoparticles within a given region. The compositional variance between sample areas may be caused by the slight variations in precursor loading.

We also summarized the compositional variations in quinary HEA-NPs (PtPdCoNiFe). Overall, the compositions are uniform with variations for most elements below 10% among nanoparticles in different regions. Since the CTS process occurred in 55 ms without using any additional steps for compositional control, we consider that this level of uniformity is outstanding.

- Region 1: the average composition is Pt (29.82±1.28%), Pd (20.72±1.11%), Co (24.48±1.09%), Ni (17.30±0.94 %), Fe (7.70±0.24%); variations for each element are: Pt (4.3%), Pd (5.4%), Co (4.4%), Ni (4.8%), Fe (3.1%).
- Region 2: the average composition is Pt (31.90±2.73%), Pd (21.18±1.06%), Co (23.58±1.22%), Ni (15.90±1.19 %), Fe (7.42±0.42%); variations for each element are: Pt (8.5%), Pd (5.0%), Co (5.2%), Ni (7.5%), Fe (5.7%);
- Region 3: the average composition is Pt (26.97±0.83%), Pd (21.64±1.04%), Co (24.97±0.83%), Ni (19.28±0.43 %), Fe (7.17±0.52%); variations for each element are: Pt (3.1%), Pd (4.8%), Co (3.3%), Ni (2.2%), Fe (7.2%);
- Overall: the average composition is Pt (28.91±2.89%), Pd (19.92±2.10%), Co (24.77±1.67%), Ni (19.04±1.88%) Fe (7.38±0.75%); variations for each element are Pt (10%), Pd (10.5%), Co (4.7%), Ni (9.9%), Fe (10.1%).

Through Fig. S42, it is clear that the quinary HEA-NPs synthesized by our CTS method have much better compositional uniformity and retains the initial amount of elements (5 vs. 4) compared to the aforementioned lithography-based technique (~10% variations for CTS vs. >50% variations for lithography).

The compositional uniformity of the HEA-NPs synthesized by our CTS method can be attributed to the high temperature mixing process and the frequency of the particle diffusion and splitting events that occur during the high temperature shock duration. During the 55 ms high temperature synthesis, each metal is actively diffusing and splitting to form a mixed liquid metal state. The subsequent quenching step freezes the composition of the mixed structure to form solid solutions, ensuring the size and composition uniformity within the sample.

2. Elemental variations among octonary HEA-NPs:

We also performed uniformity analysis for octonary HEA-NPs (PtPdCoNiFeCuAuSn) (Fig. S43). In short, the compositional variations for the octonary HEA-NPs are similar to the previous discussion on quinary HEA-NPs: (1) the nanoparticle compositions are statistically uniform within each mapped region, and (2) for a totally different sample region, the compositional variations slightly increase.

We have summarized the variations in the octonary HEA-NPs (PtPdCoNiFeCuAuSn). Overall, the composition is uniform with slightly increased variations (i.e. 10-20%) for most elements among nanoparticles at different regions. Note that these values are still considerably lower than the previous lithography-based study (>50%) *(1).*

- Region 1: the average composition is Pt (18.98±1.23%), Pd (17.20±1.36%), Co (12.78±2.63%), Ni (13.78±2.63%), Fe (10.05±0.89%), Cu (7.78±2.37%), Au (15.78±3.36%) Sn (3.73±1.00%); the variations for each element are Pt (6.5%), Pd (7.9%), Co (20.6%), Ni (23.9%), Fe (8.8%), Cu (30.5%), Au (21.3%), Sn (27.0%).
- Region 2: the average composition is Pt (20.90±1.75%), Pd (14.83±1.65%), Co (12.78±2.26%), Ni (12.93±3.32%), Fe (10.18±1.00%), Cu (8.90±1.94%), Au (14.95±4.38%), Sn (4.53±0.92%); the variations for each element are Pt (8.4%), Pd (11.1%), Co (17.7%), Ni (25.7%), Fe (9.9%), Cu (21.8%), Au (29.3%), Sn (20.3%).
- Region 3: the average composition is Pt (15.88±0.49%), Pd (16.25±0.87%), Co (11.25±2.09%), Ni (11.95±2.39%), Fe (9.43±0.69%), Cu (10.10±0.58%), Au (20.53±3.15%), Sn (4.83±0.59%); the variations for each element are Pt (3.1%), Pd (5.3%), Co (18.5%), Ni (20.0%), Fe (7.4%), Cu (5.7%), Au (15.4%), Sn (12.2%).
- Overall: the average composition is Pt (18.58±2.45%), Pd (15.90±1.40%), Co (12.00±2.02%), Ni (12.50±2.46%), Fe (9.90±0.86%), Cu (9.19±1.61%), Au (17.55±3.81%), Sn (4.46±0.84%), and the variations for each element are Pt (13.2%), Pd (8.8%), Co (16.8%), Ni (19.7%), Fe (8.7%), Cu (17.6%), Au (21.7%), Sn (18.8%).

In short, the uniform compositions arise from the high temperature heating process, which enables homogeneous mixing of different elements in the liquid metal state at high temperature. After rapid quenching, the uniformly mixed liquid metal state is retained to form solid solution nanoparticles (i.e. HEA-NPs) with compositional control.

Composition study of HEA-NPs by CTS

We have performed both microscale STEM elemental mapping and macroscale ICP-MS and XPS to determine the elemental ratio of the synthesized nanoparticles. The compositions revealed by statistical STEM elemental maps agree well with the macroscale ICP-MS result. Note that we focused on binary (PtNi), quinary (PtPdCoNiFe) and octonary (PtPdCoNiFeAuCuSn) HEA-NPs for the compositional studies described below.

1. STEM elemental maps of individual nanoparticles:

Since STEM elemental maps yield localized information with statistical significance, we ran statistics on several STEM elemental maps and compared our results to ICP-MS. Typical STEM elemental maps for binary, quinary and octonary HEA-NPs are shown at low magnifications, which display a uniform elemental distribution and confirm the formation of high entropy alloy nanoparticles.

PtNi nanoparticles. The synthesis of alloy PtNi nanoparticles is evident from the following STEM elemental maps (Fig. S44). After checking several sites, nanoparticle size and compositional uniformity were confirmed with the following features. (1) The compositional ratio of Pt:Ni is around 74:26 instead of 1:1 based on the initial precursor loading ratio. This discrepancy arises from the preferential evaporation of metals with higher vapor pressures when exposed to high temperature. Since Pt has a much lower vapor pressure (at least 3 orders of magnitude) compared to Ni, Pt evaporates less than Ni and occupies a larger percentage of the final nanoparticle composition. Detailed analysis of how vapor pressure affects the nanoparticle composition can be found in next section. The brief conclusion is that after the CTS process, usually noble metals compose a larger portion of the final nanoparticle composition compared to non-noble metals due to preferential metal evaporation of more volatile elements at high temperature. (2) The variations of composition for each element is about 1% for Pt and 3% for Ni, which demonstrates compositional uniformity within the PtNi alloy.

Quinary HEA-NPs. Similar to the PtNi alloy, we have characterized quinary HEA-NPs (PtPdCoNiFe) over multiple areas. The typical STEM elemental maps confirm high entropy mixing within the alloy nanoparticles without noticeable elemental segregation or phase separation (Fig. S45). We have the following observations. (1) The compositional ratio of the quinary HEA-NP fits well with the aforementioned metal evaporation sequence (based on vapor pressure). Pt still has the largest ratio due to its low vapor pressure, then Pd, Co, and Ni have similar vapor pressures (and therefore similar compositional ratio), followed by Fe which has the highest vapor pressure (and lowest ratio). (2) Compared with PtNi, both the size and compositional variations are slightly larger: the average composition is Pt (28.91±2.89%), Pd (19.92±2.10%), Co (24.77±1.67%), Ni (19.04±1.88%), Fe (7.38±0.75%); the compositional variations for each element are Pt (10%), Pd (10.5%), Co (4.7%), Ni (9.9%), Fe (10.1%). (3) The increased variations can be explained by the particle dispersion mechanism (catalytic carbon metabolism) for the CTS process. Elements with higher catalytic activity will result in more particle fusion/fission steps to occur at high temperature to improve both size and compositional uniformity. For PtNi, it contains a larger portion of noble metals than the quinary PtPdCoNiFe, which may result in better uniformity in terms of nanoparticle size and composition due to enhanced catalytic effects. (4) It should be noted that the compositional variations in the quinary PtPdCoNiFe HEA-NPs are comparably smaller than quinary MMNPs (AuAgCoNiCu) synthesized by the reported lithography-based technique with a composition variation of ~50% (Fig. S42).

Octonary HEA-NPs. We also performed similar STEM elemental map analysis for the octonary HEA-NP (PtPdCoNiFeAuCuSn) system, where alloys composed of 8 elements do not show elemental segregation or phase separation (Fig. S46). We have the following observations. (1) The compositional ratio of the octonary HEA-NPs also roughly follows the vapor pressure sequence, where noble metals contain a larger portion of the final nanoparticle composition than non-noble metals. (2) The particle size and compositional variance for the octonary HEA-NPs are slightly higher than the PtNi and quinary PtPdCoNiFe HEA-NPs due to the same aforementioned reasons (the number of noble metals with higher catalytic activities alters the particle size, composition, and dispersion). (3) The average composition is Pt (18.58±2.45%), Pd (15.90±1.40%), Co

(12.00±2.02%), Ni (12.50±2.46%), Fe (9.90±0.86%), Cu (9.19±1.61%), Au (17.55±3.81%), Sn (4.46±0.84%); the composition variations for the octonary HEA-NPs are Pt (13.2%), Pd (8.8%), Co (16.8%), Ni (19.7%), Fe (8.7%), Cu (17.6%), Au (21.7%), Sn (18.8%). (3) Compared to the lithography-based technique with variations of ~50% for 5 elements, our compositional variations are still much smaller even with up to 8 dissimilar metals, which lends itself to the metrics of our CTS method.

The statistical analysis gathered from STEM elemental maps confirms: (1) the formation of high entropy alloy nanoparticles and (2) the low compositional variance for HEA-NPs prepared by the CTS method. Overall, the fluctuation in composition falls within ~20%. By statistical distributions, the synthesized nanoparticles are considered uniform in composition, especially compared to previous reports in the literature.

2. ICP-MS and STEM map comparison:

ICP-MS was performed and the results are in good agreement with the aforementioned statistical STEM results (Table S3). The general trend for the final composition of HEA-NPs prepared by the CTS method is that noble metals compose larger portions of the nanoparticles compared to non-noble metals. This is primarily due to the difference in vapor pressure between noble and non-noble metals at high temperature, which results in preferential metal evaporation of particular metal species. The effect of vapor pressure on the final nanoparticle composition (as well as approaches to precisely control composition) is explained in detail in the following section.

Compositional control strategies

Based on the compositional analysis, the elemental compositions of HEA-NPs are not exactly the same as the molar ratio of the precursors (which may depend on vapor pressure). However, we have proposed and developed strategies to control the composition more reliably.

The following are our observations and understanding of the CTS process:

- There are two major steps in the CTS method. In principle, the first step, i.e. precursor loading on the conductive support, can be precisely controlled. The second step, i.e. high temperature thermal shock, is most likely to cause the precursor ratio discrepancies.
- In the second step (thermal shock), we found that the metal evaporation (vapor pressure) of the metals plays an important role.
- Metals with high vapor pressures (usually non-noble metals) will evaporate much more than metals with low vapor pressure (noble metals). This results in final particles composed of a larger amount of noble metals by atomic percentage.
- Note that the vapor pressure for chlorine is about 3-4 orders of magnitude higher than both types of metals and thus, there is a negligible amount of chlorine left on the sample from XPS (Fig. S30) and STEM mapping results (Fig. S16).

We also proposed the following strategies to tune nanoparticle compositions:

- Noble metals usually have a much lower vapor pressure, which allows more precise compositional control over particles predominantly composed of noble

metals. Thus, HEA-NPs composed of only noble metals were synthesized and investigated.

- Non-noble metals usually have a much higher vapor pressure. In principle, we can evaluate the evaporation rate (loss of metals) based on the metal's vapor pressure (or partial pressure, as a function of temperature) and then compensate for this loss by adjusting the initial precursor loading. We have experimentally proven this concept using binary alloys such as PtNi.
- Tunability may be even easier if the experiment is done on a "closed" substrate (e.g. 2D graphene sheets) that can effectively trap the metal vapor within the structure to maintain a more reliable elemental ratio.

1. The role of vapor pressure for the incorporated metals:

During the high temperature heating process, non-noble metals can preferentially evaporate due to increased vapor pressure at high temperatures. According to *Vapour pressure equations for the metallic elements: 298--2500K (37),* the theoretical vapor pressure for each metal in the bulk and single element states can be estimated by the following equation:

$$\log\left(\frac{p}{atm}\right) = A + \frac{B}{T} + C * \log(T) + D/T^3$$

where *p* is the vapor pressure, *atm* is the atmospheric pressure, *T* is the temperature, and *A, B, C,* and *D* are fitting parameters. By using existing parameters for *A-D (37),* we have drawn the temperature-dependent vapor pressure curves (Fig. S47).

It is clear that the vapor pressure can be broken into three parts: (1) the gaseous chlorine (Cl_2), which has the highest vapor pressure (10^5 Pa, which is at least 3-4 orders of magnitude higher than all other metals); (2) metals with high vapor pressures (Co, Ni, Fe, etc; $10\sim10^2$ Pa); (3) metals with low vapor pressures (Ir, Ru, Pt, Rh; $\sim10^{-3}$ Pa). At high temperature, the Cl_2 gas is the first to escape from the system, followed by the non-noble metals with high vapor pressures and to a lesser extent, the noble metals with low vapor pressures.

During the high temperature CTS process, the only possible loss of metals occurs through high temperature metal evaporation. Accordingly, high vapor pressures relate to higher evaporation rates and therefore higher loss for these metallic elements, which causes compositional discrepancies for the synthesized HEA-NPs (especially when the HEA-NP design consists of more non-noble metals with relatively higher vapor pressures).

In summary, the aforementioned vapor pressure is the primary factor that determines the amount of each metallic element present in the final nanoparticle composition. Note the actual vapor pressure of the elements within the synthesized HEA-NPs can be different from the theoretical values due to the following factors:

Elements in HEA-NPs are in a high entropy mixing state instead of single elements and thus, the (partial) vapor pressure for alloys can be very different from each specific element.

These elements are all involved in the catalytic carbon metabolism reaction on the carbon surface instead of pure physical evaporation.

2. ICP-MS results compared with the vapor pressure effect:

We have also used ICP-MS to determine the composition of the HEA-NPs synthesized by our CTS method (summarized in Table S3). Since metal evaporation is an overall phenomenon, ICP-MS serves as an ideal technique to indicate and evaluate the compositional evolution for the CTS process.

For binary PtNi alloys, the composition of the ICP-MS result is Pt:Ni = 72.8 : 27.1. In the final composition, Pt is almost 3 times higher than Ni. This can be explained by the vapor pressure effect, where Pt has a much lower vapor pressure (at least 3 orders lower) than Ni.

As shown in Fig. S48, the compositional ratio for quinary HEA-NPs (PtPdCoNiFe) increases and follows the sequence [Fe (10%), Pd (18.3%), Ni (21%), Co (24.8%), Pt (26%)], which is also the sequence of decreasing vapor pressure. Namely, a higher vapor pressure metal corresponds to a lower elemental ratio in the final HEA-NP (PtPdCoNiFe) composition. This experiment further indicates that vapor pressure plays a key role in the final composition of HEA-NPs.

We also investigated the octonary HEA-NPs (PtPdCoNiFeAuCuSn) with an actual compositional sequence of Pt>Au>Pd>Co>Ni>Cu>Fe>Sn (20.3%, 18.75%, 17.7%, 10.6%, 10.26%, 9.4%, 9.55%, 3.53%, respectively). In this case, the evaporation sequence is roughly followed, where metals with lower vapor pressures constitute larger percentages of the final composition. It should be noted that the ratios of Au and Pd are slightly larger than expected based on the theoretical values, even though the vapor pressures for Pd and Au are similar to Co and Ni. As stated before, the disturbance of the theoretical vapor pressure sequence may arise from the difference in catalytic activity. Since Au and Pd possess enhanced catalytic properties, these noble metals are more actively involved in the catalytic metabolism reaction that occurs on the carbon surface during the CTS process, which possibly decreases the evaporation of noble metals.

3. Strategies to tune HEA-NP composition:

Comparatively, the first step of the two-step CTS method (solution-based precursor loading) has a greater level of control. Specifically, excellent conformal precursor coatings have been demonstrated on CNF substrates using ethanol-based solutions. In the second step of the CTS method, the main factor in terms of compositional control is the metal loss due to evaporation. We therefore envision the following strategies to tune composition, which are supported with additional experimental data:

(a) Direct compositional control of HEA-NPs composed of noble metal elements

Noble metals have much lower vapor pressures and higher catalytic properties compared to non-noble metals, which results in negligible metal evaporation and more involvement in the catalytic carbon metabolism to facilitate particle dispersion. For example, we synthesized quinary HEA-NPs composed of purely noble metals (Pt, Pd, Ru, Rh, Ir) with an initial precursor ratio of 1:1:1:1:1 to determine compositional uniformity. Each of the five elements has relatively similar ratios (0.92:0.89:0.94:1.09:1.16) after synthesis, which indicates remarkable compositional tunability for entirely noble metal HEA-NPs (Fig. S49).

(b) Indirect compositional control by precursor compensation of non-noble metals

For non-noble metals (which are usually low cost), the relatively high vapor pressures correspond to greater metal loss via evaporation at high temperature. To compensate for

this loss, the initial precursor ratio can be altered (i.e. add more non-noble metal precursors). Note that this compensation approach is a common strategy in high temperature synthesis, where volatile elements are involved.

We used PtNi as the model system to investigate how to adjust the precursor ratio to compensate for metal loss (Ni) in the high temperature CTS synthesis method. The target ratio for Pt and Ni is 1:1. We adjusted the precursor ratio (Pt salt vs. Ni salt) to be 1:1, 1:1.5, 1:2, 1:3, 1:3.5 (i.e. adding more Ni to the initial precursor solution to compensate for Ni loss) (Fig. S50). Previously, from the ICP-MS results, the synthesized PtNi nanoparticles without precursor compensation (i.e. the initial ratio of 1:1) results in roughly Pt_3Ni (0.728:0.271) due to preferential Ni evaporation. After adding more Ni to the precursor solution, the Ni concentration in the final product increased linearly. The linear trend guided us to design a 1:1.6 initial precursor ratio, which resulted in a final ratio that is very close to the 1:1 target (exact ratio of 0.95:1).

(c) Compositional control using a "closed" matrix (e.g. 2D materials as a substrate)

As shown in the following schematic, metal evaporation readily occurs in the 1D CNF substrate due to the open fiber network/structure, which allows chlorine gas to easily escape (Fig. S51a). It is, therefore, reasonable to find alternative methods to reduce/prevent evaporation by using a more "closed" system, such as 2D reduced graphene oxide (RGO) films (Fig. S51b). Since RGO has a very large aspect ratio (nanometer thick sheets with micrometer lateral sizes) and has been acknowledged for its impermeability *(38)*, RGO can effectively reduce/prevent metal loss by evaporation during the CTS process. Additionally, RGO is the oxidized derivative of graphene and thus, contains surface-bonded functional groups and defects. As described in our work (i.e. discussion on the role of defects on different thermally reduced CNF films as well as the comparison between defective CNFs and crystalline CNTs), defects are crucial to effectively disperse nanoparticles on a given substrate. Thus, RGO is also deemed a suitable defective substrate to achieve uniform particle distributions.

As an example, we used a 2D carbon substrate composed of RGO sheets to synthesize PtNi nanoparticles using identical CTS parameters (55 ms, ~2000 K). Uniformly distributed PtNi can be found on the RGO sheets (Fig. S52a). The STEM elemental maps also confirm the formation of PtNi alloys. In the CTS process, the RGO sheets act as a cover to reduce/prevent the evaporation of Ni, which results in nearly a 1:1 ratio of PtNi compared to a 3:1 ratio for the open, 1D CNF support (Fig. S52b, c). Therefore, a 2D carbon support can be utilized as an alternative substrate for the CTS method to achieve better compositional control.

As demonstrated for HEA-NPs on 1D CNF supports, we can also employ the same compensation approach to achieve target ratios among different elements for other types of supports (2D RGO, *etc*). Note that this approach is a common strategy in high temperature synthesis, where volatile elements are involved.

<u>Control experiments: nanoparticles on more crystalline CNFs and CNTs</u>

We hypothesized that the defect concentration is the fundamental reason for the effective dispersal of metallic nanoparticles on the carbon support. To verify this, control experiments were conducted using synthesized nanoparticles on CNFs with different

degrees of crystallinity. The low temperature carbonized CNFs (CNF-873K and CNF-1073K) have more defects than CNFs carbonized at high temperature (CNF-1273K) (Fig. S2). As shown in Fig. S53, increasing the carbonization temperature causes the synthesized nanoparticles to become larger and less uniform in terms of dispersion. This result confirms that defects enable uniform dispersions on CNFs.

We further studied nanoparticle dispersion (using AuNi as the model material) on crystalline carbon nanotubes (CNTs) that contain a greatly reduced amount of defects (control experiment) (Fig. S54). The crystalline CNTs have a much lower defect content compared to the CNFs, as indicated by both Raman and XPS results. As expected, the particles are not well dispersed on CNTs and instead form aggregates due to the crystalline carbon surface. This result confirms that the surface defect concentration is important for particle dispersion.

All the experimental results shown above clearly demonstrate that defects are crucial for particle dispersion in our CTS method. For substrates lacking defects, the particles can only coarsen without forming fine nanoparticles.

Control experiments: catalytic activities of metal species

In addition to the substrate/defect effect, we gathered experimental data to support the catalytically-induced particle dispersion mechanism by examining particle dispersion behaviors among different metals. As shown in Table S4, it is known that Au and Cu are Group 11 metals with very similar physical properties and non-reactive/non-wetting behavior with carbon (wetting angles at 138° and 139° near their melting points, respectively) (*Wettability at high temperatures (1999), vol. 3.*) *(22).* Au and Cu also have similar vapor pressures at the same temperature. According to conventional melting and nucleation theory and the similarity of physical properties between Au and Cu, these metal nanoparticles should behave similarly and only coarsen on carbon after the high temperature shock.

However, as shown in Fig. S55, Cu and Au behave drastically different even though the same synthesis protocol (55 ms high temperature shock with the CNF from the same batch) was employed:

- Each formed relatively distributed nanoparticles instead of particle coarsening yet, the Au NPs seem more evenly dispersed on the CNF;
- The NP size distributions are drastically different. Specifically, the Cu particles are very large (~56 nm), while Au exhibited relatively tiny particles (~13 nm) that are uniformly dispersed on the carbon substrate.

Considering the physical property similarities of Au and Cu (Table S4), such a difference in size distribution indicates that the underlying particle dispersion mechanism during the CTS method is beyond a simple, physical melting-and-nucleation mechanism. Besides physical properties, Au and Cu have a discrepancy in terms of catalytic activity towards the carbon metabolism reaction [C+O*=CO (gas)], where Au has higher catalytic performance than Cu *(39).* Accordingly, it is reasonable to infer that the metal's catalytic activity may play a critical role in terms of nanoparticle dispersion.

This catalytically-driven particle dispersion mechanism was further proven by the dispersion of Pt nanoparticles on CNFs, where even smaller and more uniformly distributed

nanoparticles are readily achieved (Fig. S56). Note that Pt has higher catalytic activity than Au and Cu, which coincides with nanoparticle dispersions being highly dependent on the catalytic activity of the metal species.

Extending from single elements to multi-element alloys, we also verified such a mechanism in the alloy formation of AuCu (Fig. S57). The combination of AuCu shows a uniform dispersion with a particle size (~24 nm) within the range of individual Au and Cu nanoparticles (Fig. S55). It is worth noting that the combination of Au and Cu results in a much smaller particle size distribution compared to pure Cu, which indicates that alloying with higher catalytic elements can help disperse the lower catalytically active elements.

Therefore, from the aforementioned results, the nanoparticle dispersion mechanism in the CTS process is highly related to the following: (1) the number of surface defects on the carbon substrate and (2) the catalytic activities of the metal species. Specifically, higher defect concentrations and the use of metals with higher catalytic activities results in smaller nanoparticle sizes and a more uniform distribution on the conductive substrate.

In situ mass spectroscopy

The in situ mass spectra were used to record the release of gas phases from both bare CNF and CNF with AuNi nanoparticles during the CTS process. In this case, a molecular beam sampling system with a reflectron time-of-flight mass spectrometer (MBMS) was employed at elevated pressures (1 atm) (Fig. S58a). The CNF-based sample was put into the end of a 10-mm diameter quartz tube while ambient atmosphere was maintained by a constant inlet and outlet flow of argon gas. Both CNF and CNF-AuNi films were ignited by the electrically-triggered Joule heating process. The gas product(s) during the CTS process were released into an intermediate region of relatively low pressure (~10^{-3} Torr), and into the E-gun (70 eV) ionization chamber (~10^{-6} Torr). This creates a molecular beam that enables the preservation of the sample with enough time to reach the mass spectrometer detector. Roughly 3.5 seconds of time-resolved data were captured utilizing a 600 MHz Teledyne LeCroy Oscilloscope at a sampling rate of 1 mass spectra per millisecond (1 kHz).

The in situ mass spectra data (MBMS) (Fig. S58b-c) reveals the release of gaseous species (especially CO) from both the bare CNF and CNF-AuNi samples. The temporal evolution of CO in the CNF and CNF-AuNi samples demonstrates that the AuNi nanoparticles facilitate a faster and larger response of CO compared to bare CNFs at high temperature. Note that liquid metals are good catalysts, e.g. for the vapor-liquid-solid process, which verifies the enhanced catalytic carbon metabolism reaction (C+O*=CO↑) for CNF-AuNi compared to bare CNF. The carbon 'metabolism' reaction involves C (fuel), O* (oxidizer) and metal (catalyst), which correlates the effect of O* (i.e. surface defects) and the metal's catalytic activity on the final nanoparticle size and dispersion.

Note that the production of CO_x (MBMS data) alone cannot exclude droplet diffusion across the carbon support without splitting. However, the following experimental observations and analysis combined with the MBMS data confirm the fission/fusion process (i.e. particle dispersion mechanism), instead of droplets diffusing across the carbon support:

1) The metals do not wet carbon at high temperatures *(22).* The metal particle droplets

will only coarsen on carbon to minimize surface energy and will not result in HEA-NPs (~10 nm) that are readily achieved from our CTS process.

2) If there is no fission involved in the CTS process, metals (e.g. Cu and Au) with similar melting temperatures and wetting angles should have similar nanoparticle sizes when an identical CTS process and CNF substrate is used. However, this is drastically different from our experimental observations (Fig. S55-S57).
3) Catalytic chemical reactions (i.e. C+O*=CO (gas)) can provide the driving force for particle fission to increase the metal surface area. Particle fission does increase the surface energy of the particles, but the energy loss in the catalytic reaction [C+O*=CO (gas) (ΔH= -110.5 kJ/mol)] is much higher. Thus, the overall process involving particle fission is energetically possible.
4) The catalytically-induced particle fission/fusion mechanism can explain the observed dependence of particle dispersion on both the defect concentration of the substrate and the catalytic activity of the metal species. Specifically, carbon, defects, and metals are all actively involved in the catalytic carbon metabolism reaction. Varying these factors affects the overall activity of the carbon metabolism and consequently, the particle fusion/fission steps alter the level of particle dispersion.
5) As analyzed later, the timescale for microsized particles (size of precursor and the resultant metal droplets) to diffuse across the particle-particle distance is >10 s, which is much longer than the 55 ms time used to achieve uniform nanoparticle dispersions.

Particle dispersion mechanism

We proposed the catalytic metabolism-induced 'particle fission and fusion' mechanism as the origin for the uniform dispersion of nanoparticles on oxygenated carbon by the CTS method. Here, particle fusion means several particles meet and coalesce into one particle, while particle fission refers to one particle splitting into several smaller particles. Briefly, the high temperature provides energy for particles to move around and undergo fusion, while the catalytic metabolism [C+O*=CO (gas)] provides the driving force for particle fission/splitting; the numerous particle fission/fusion events yield a dynamic steady state, where uniformly distributed nanoparticles form on the carbon surface after rapid quenching.

As shown in Fig. 3B, the metallic particles (e.g. binary AuNi) on crystalline (i.e. less defective) carbon will only coarsen at high temperature to reduce their surface energy as a thermodynamically favorable process. However, if the carbon contains defects, namely oxygenated carbon, the particles can be uniformly dispersed after the CTS process.

Step I: Salt decomposition. At high temperature, the salt precursors decompose and form liquid metals on carbon. The high temperature ensures total decomposition of the salt precursors and provides energy for these liquid metals to move around on the carbon surface.

Step II: Particle fusion and fission. The liquid metals actively move around on the substrate. However, growth is hindered by the defective sites present on the carbon support. The particles can undergo particle fission by interaction with O* on the carbon surface, which promotes the catalytic carbon metabolism reaction [C+O*=CO (gas)] at high temperature. Also, particle fusion occurs when particles meet and fuse. Catalytically-

driven particle fission is the key step to form uniformly distributed nanoparticles on the carbon surface, which is in stark contrast to a pure fusion and coalescence mechanism.

Step III: Dynamic steady state. Based on later analysis (Fig. S59), fission and fusion of ~10 nm metallic nanoparticles at 2000 K should occur much faster than a 0.1 μs timescale. Therefore, in a 55 ms shock process, it is estimated that the particles can make at least $>10^6$ random steps to ensure uniformity in both size and composition.

The existence of catalytic carbon metabolism during the CTS process is confirmed by in situ molecular beam mass spectra (Fig. S58). Enabled by catalytic carbon metabolism, carbon (C), defects (O*) and metals (catalysts) undergo solid-liquid-vapor catalytic reaction, which provides the driving force for particle fission to increase the metal surface area to catalyze the reaction. Particle fission does increase the surface energy of the particles, but the energy loss in the catalytic C+O*=CO (gas) (ΔH= -110.5 kJ/mol) reaction is much higher. Thus, the overall process involving particle fission is energetically favorable. In literature, particle splitting/fission has been proven to occur for supported metallic nanoparticles involving the catalytic reactions *(23-26)*.

Without the supply of fuel (C) and oxidizer (O*), at high temperatures, the metal particles will only coarsen on carbon to minimize their surface energy, which follows conventional high temperature alloying/wetting knowledge.

Timescale analysis for the CTS process

1. The timescale for catalytically-driven particle fission/fusion:

Based on the systematic calculations shown in "*Changing Shapes in the Nanoworld" (28),* fission and fusion of metallic nanoparticles at 800 K should occur at a microsecond timescale (Fig. S59a). For a ~10 nm spherical nanoparticle, which contains roughly 30,000 atoms [log(N) ~ 4.48, where N is the number of atoms in the sample], the relaxation time (t_{eq}) is on the order of ~100 μs. It should be noted that the CTS process occurs at a much higher temperature (~2000 K) and thus, the relaxation time should be at least 3-4 orders of magnitude faster than at 800 K. As shown in Fig. S59b *(30),* the estimated surface diffusivity of metals at 2000 K (1E-4 cm^2/s) is ~3-4 orders of magnitude higher than at 800 K (6E-8 cm^2/s). Therefore, it is expected that the timescale for shape change to occur at 2000 K should be around 0.01-0.1 μs. Note that we used 0.1 μs as the timescale for later analysis.

2. The timescale for random diffusion of precursor elements:

Note that the size of the salt precursor (and the resultant metal droplets) is in the range of 1-10 μm. For a metal droplet with a size of 1 μm (log(N)=10.48) or 10 μm (log(N)=13.48), the timescale for random diffusion is $\sim 10^{3.8}$ s (~6,300 s) and $10^{7.7}$ s (~50,118,723 s), respectively, based on extrapolations of the relaxation time curve at 800 K.

At 2000 K, the timescale of random diffusion would be 3-4 orders of magnitude faster, corresponding to ~10 s or 50,000 s for 1 μm and 10 μm droplets, respectively. Note that this is still a significantly longer amount of time than the 55 ms duration of our CTS synthesis. Therefore, random diffusion of the precursor elements is NOT the underlying mechanism.

3. The timescale for droplet movement across the carbon surface in our fission-fusion process:

The liquid metal droplets move by caterpillar-like "peristaltic motion" that involves elongation and shrinkage of each particle to harvest O*, which occurs on a comparable kinetic timescale as the fission and fusion events. Thus, if peristaltic motion takes 0.1 μs (as calculated above) and consequently, the particle moves by a distance of 10 nm (the particle size) in a random direction, then a 55 ms shock duration would correspond to 550,000 random steps. In this case, the mean migration/diffusion distance would be 10 nm $\times (550{,}000)^{1/2}$ = 7.4 μm, which is larger than the distance between precursor particles. This is a sufficient distance to uniformly disperse the 10 nm nanoparticles on the CNFs from the original precursors.

Ultrafine and well-dispersed HEA-NPs

The proposed particle dispersion mechanism relies on defective substrates and (catalytically active) metals to promote more vigorous carbon metabolism reactions and thus, achieve smaller and narrower particle sizes/distributions.

By using a CO_2 activation treatment (1023K for 3 h in CO_2) on the CNFs to create more surface-bound defects, quinary HEA-NPs (PtFeCoNiCu) can be synthesized with a smaller size distribution (5.30 nm ± 1.31 nm) compared to the same quinary nanoparticle composition (PtFeCoNiCu) on the initial CNF substrate (11.3 nm ± 2.2 nm), as shown in Fig. S60.

Further improvements in terms of nanoparticle size distribution can be achieved by using catalytically active metal combinations (PtPdIrRhRu) on the same defective substrate, CO_2-activated CNFs (CA-CNFs). TEM and HAADF images display the ultrafine and well-dispersed quinary HEA-NPs (PtPdIrRhRu) formed on CA-CNFs by CTS (Fig. S61). Therefore, the combination of (1) CO_2 activation to increase the surface-bound defect concentration and (2) the use of only metals with high catalytic activity (Pt, Pd, Ir, Rh, Ru) leads to additional enhancements in particle dispersion and size distribution (3.28 nm ± 0.81 nm)

In addition, we also confirmed the high entropy solid solution formation of these quinary nanoparticles by STEM elemental mapping (Fig. 3D in the main text). Uniform particle dispersion and high entropy mixing at a low magnification are also shown in Fig. S62, which confirms particle uniformity over a larger sample area.

Time-dependent size distribution

The time-dependent size distribution was also confirmed with the AuNi nanoparticle system (Fig. S63). Note that longer high temperature durations will result in larger diameter nanoparticles.

As defects play a key role in the dispersion of the synthesized nanoparticles, prolonged high temperature durations will remove numerous defects and lead to nanoparticle aggregation. The results from Raman spectra, conductivity measurements, and the change in carbon content of the CNF-PtNi films after 5 ms, 55 ms, 1 s, and 10 s

shock durations reinforce the fact that increased crystallinity (decreased defect concentration) occurs as the shock time increases (Fig. S64).

Cooling rate-dependent nanostructures

By tuning the cooling rate of the CTS process, the resultant nanostructure can be adjusted owing to diffusion-limited kinetics. Fig. S65 shows rate-dependent nanostructured systems (Au-Ni and Cu-Co) synthesized with various cooling rates (~10^5 K/s, ~10^3 K/s, ~10 K/s). Based on the cooling rate, the nanoparticles are in a solid solution or phase-separated structure. Fig. S65c summarizes the synthesized nanoparticles at each cooling rate.

The detailed atomic HAADF images of AuNi with various cooling rates (10^5 K/s vs 10 K/s) are shown in Fig. S66. The atomic scale STEM-HAADF image of the AuNi solid solution nanoparticle is along a [1-10] zone axis. In this case, the cooling rate was ~10^5 K/s and the d-spacing of the main lattice planes was 2.22 Å. This correlates to the {111} planes of the *fcc* metallic Au metal crystal structure (Fm-3m, a=b=c=4.079, JCPDF 04-0784) and *fcc* metallic Ni metal crystal structure (Fm-3m, a=b=c=3.524, JCPDF 04-0850). A twin boundary also exists along the {111}. With a rate of ~10 K/s, the AuNi nanoparticle phase separates ([1-10] zone axis; 2.30 Å interplanar distance (in the upper region); matches well with the {111} of Au) (Fm-3m, a=b=c=4.079, JCPDF 04-0784). In the lower region, the measured spacings (2.06 Å and 1.80 Å) are very close to the (111) and (002) planes of the Ni metal crystal structure (Fm-3m, a=b=c=3.524, JCPDF 04-0850).

Besides the demonstration of rate-dependent nanostructures, it was found that both slow heating (~10 K/s heating and instant cooling) and cooling (instant heating and ~10 K/s cooling), the resultant nanoparticles suffer from serious aggregation problems (Fig. S67). Besides, these nanoparticles are stuck within the CNFs after slow and prolonged heating, which is likely due to carbon scavenging by the catalytic carbon metabolism reaction (C+O*=CO↑). In this case, the surface O* depletes during the long CTS duration at high temperature. These control experiments indicate thermal shock is a unique and important process to achieve effective and tunable nanoparticle dispersions.

We have studied the defect changes in CNFs using different cooling rates (Fig. S68). The Raman spectra show no obvious changes in defect density until a cooling rate of 10 K/s. Specifically, the CNF shows a very sharp G peak and a suppressed D peak, which indicates a drastic increase in crystallinity of the CNFs using a ~10 K/s cooling rate. The loss of defects results in particle agglomeration (Fig. S67). The conductivity and carbon content also show a similar trend where a cooling rate of ~10 K/s produces CNF films with enhanced conductivity values and a higher carbon content. Note that defects are removed under prolonged high temperature exposure.

Catalytic ammonia oxidation by quinary HEA-NPs

Nitric acid is an important bulk chemical used as a feedstock for the production of fertilizers, nylon, explosives and many specialty organic compounds *(32).* Pure platinum gauze served as the first-generation catalyst for the Ostwald process. Later, pure platinum was replaced by platinum-rhodium alloys, in which the rhodium content (5–10%) was

introduced to increase the thermal stability of platinum gauze *(33).* After a serious operational problem related to platinum losses [caused by the formation of volatile platinum oxides (PtO_2)], palladium was introduced together with some other minor metals (e.g. Ru, Re) to suppress the formation of PtO_2 under the reaction conditions *(34).* Despite the extensive efforts on the exploration of new catalysts, PtPdRh-based multimetallic alloys still serve as the main catalysts in modern industrial endeavors. Typically, the oxidation of ammonia in the Ostwald process is operated at 800-950°C for complete conversion of ammonia (NH_3), yielding 94–96% NO_x ($NO + NO_2$) and 4–6% by-products (N_2O and N_2). Substantial interests have been attracted to the development of advanced catalysts for the selective oxidation of ammonia to nitrogen oxides, targeting improved selectivity towards the desired NO_x, lower reaction temperatures and/or the use of less precious metals.

In this work, we aim to demonstrate our high entropy alloy nanoparticles as advanced catalysts for the ammonia oxidation reaction. High entropy alloys have shown superior structural stability and high resistance to corrosion and creep, due to four distinct features/effects *(16, 18):*

(1) High entropy effect, which helps stabilize the solid solutions thermodynamically;

(2) Sluggish diffusion effect, which prevents phase separation and elemental segregation to occur even at high temperatures;

(3) Severe lattice distortion, which leads to slow kinetics for diffusion and deformation and thus, increases strength and structural stability;

(4) The cocktail effect, which enhances the properties of HEA by alloying and synergistic effects from the interactions among all elemental constituents.

Using the CTS method, PtPdRhRuCe quinary alloy nanoparticles were prepared on CNFs with a mass loading of 21.7% Pt, 4.68% Pd, 1.30% Rh, 0.34% Ru and 0.23% Ce (the rest is substrate) (denoted as PtPdRhRuCe HEA-NPs). This compositional design is derived from industrial-grade catalysts that contain PtPdRh. Specifically, each element has the following purpose: Pt (as the dominate active sites), Pd (to decrease cost, increase structural stability, facilitate the reduction of intermediates such as Pt-O, and resist the formation of Rh oxide), and Rh (to increase the thermal stability under high temperature operation). The addition of Ru and Ce serve the following purposes: to decrease cost even further, to improve the oxygen storage capabilities, and to increase oxygen mobility *(35, 36).* Herein, by utilizing our unique CTS method, we were able to synthesize solid solution quinary nanoparticles (i.e. HEA-NPs) with uniform sizes and high surface area which is critical to achieve superior performance for the ammonia oxidation reaction.

1. Microstructure of the quinary HEA-NPs used for ammonia oxidation:

Fig. S69 shows the SEM and TEM images of the prepared catalysts (same composition, substrate, and loading) via the CTS method and the wet impregnation method. Uniform quinary particles (~20 nm) are well-distributed throughout the PtPdRhRuCe HEA-NP sample, which confirms excellent particle formation and dispersion on the CNF support by CTS. Unlike the CTS method, the PtPdRhRuCe MMNP samples prepared by wet impregnation show aggregations (poor dispersion) on the CNFs since the precursors were exposed to a (relatively) low temperature and slow reduction process.

Note that the MMNPs synthesized by wet impregnation have poor contact/adhesion (i.e. metals do not wet carbon well) since only a small amount of particles are present on the CNFs after the sonication process (for TEM sample preparation). However, HEA-NPs synthesized by the CTS method exhibit excellent particle adhesion and retention after the sonication process. This indicates that unlike wet impregnation, the CTS process produces HEA-NPs that bind very well to the carbon substrate. The reason for this may originate from the unique particle dispersion mechanism of CTS: at high temperature, all nanoparticles were actively involved in the catalytic carbon metabolism reaction and closely interact with the carbon substrate to ensure good contact/adhesion.

2. STEM elemental map comparison of both quinary MMNPs (PtPdRhRuCe):

Fig. S70 shows the STEM elemental maps of the aforementioned samples synthesized by completely different methods (CTS vs wet impregnation with a slow reduction process). From the STEM maps, it is clear that our PtPdRhRuCe HEA-NP sample formed high entropy solid solution nanoparticles while the control PtPdRhRuCe MMNPs sample suffered from severe phase separation between Pt and Pd. Even though the salt precursors are decomposed or reduced, the tendency for the metal atoms to retain a mixed state during a slow and low-temperature reduction procedure is unfavorable and thus, results in phase-separated nanoparticles for the control sample.

The composition of quinary PtPdRhRuCe is also determined by macroscopic ICP-MS and microscale statistical TEM analysis (Table S5). These two compositions agree well with each other and resemble the original elemental design.

3. STEM map after the ammonia reaction:

We also checked the integrity of the quinary HEA-NPs after the high temperature catalytic reaction using STEM elemental mapping (Fig. S71). These quinary HEA-NPs (PtPdRhRuCe HEA-NPs) still possess the original high entropy solid solution structure; each element remains uniformly distributed throughout the nanoparticles synthesized by the CTS method without obvious phase/element separation/segregation. Note that after the high temperature reaction, Ce is oxidized, which is expected since Ce is a non-noble metal that is not as oxidation-resistant as other noble metals. This result confirms the stability of the HEA-NPs synthesized by the CTS method even after catalytic reaction at high operation temperatures.

4. Catalytic performance of a cheaper combination of quinary HEA-NPs (PtPdRhCoCe):

Additionally, in order to reduce the cost of the catalyst further, we employed the CTS method to prepare one more catalyst (5 element composition) system by replacing ~37.5% of Pt with Co and eliminating Ru, i.e., PtPdRhCoCe quinary alloy nanoparticles with a mass loading of 17.2% Pt, 4.1% Pd, 1.1% Rh, 4.1% Co and 0.7% Ce (the rest is the carbon substrate) (denoted as PtPdRhCoCe HEA-NPs). The catalytic performance of this cheaper catalyst was thus evaluated, with metrics shown in Fig. S72a. It should be noted that NH_3 was completely converted throughout the investigated temperature range (500–800°C). The selectivity towards the desired products ($NO + NO_2$) achieved 90% at 600°C, which is even higher than the aforementioned PtPdRhCoCe HEA-NPs sample ($NO+NO_2$

selectivity = 49.8% at 600°C). The durability of the PtPdRhCoCe HEA-NPs was explored via long-term (30 h) experimental testing (Fig. S72b). The catalytic performance of the PtPdRhCoCe HEA-NPs catalysts remained stable under prolonged reaction conditions. Specifically, both the NH_3 conversion and the product selectivity showed no degradation for 30 h at 700°C.

5. Performance comparison with literature:

Further comparisons of the PtPdRhRuCe HEA-NPs and PtPdRhCoCe HEA-NPs catalysts to other alloy-based catalysts reported in literature confirm the advantage of the CTS method in synthesizing catalytically active high entropy alloy nanoparticles. Specifically, superior catalytic performance for the ammonia oxidation reaction can be achieved even at reduced precious metal loadings under similar reaction conditions or at even lower reaction temperatures (Table S6). In short, these synthesized high entropy alloy nanoparticles exhibit substantial improvements in catalytic performance by being highly efficient (5-6 times less precious metal loading), catalytically active (100% conversion), and achieving product selectivity (>99%) for ammonia oxidation to NO_x. The HEA-NPs synthesized by the CTS method show great potential as multifunctional and highly efficient catalysts.

6. Some future applications of ultra-fine HEA-NPs supported on a carbon matrix:

Using the CTS method, uniformly distributed HEA-NPs can be synthesized in an efficient and scalable manner with control over composition, size and structure (solid solution, phase-separated). These HEA-NPs can be applied for a wide range of industrial applications, such as catalytic oxidative coupling of methane (OCM), catalytic car exhaust treatment and selective ammonia oxidation to NO_x ($NO+NO_2$) etc., as elaborated below.

Catalytic oxidative coupling of methane. Catalytic oxidative coupling of methane (OCM) is an alternative, economic and environmental approach to directly convert methane into more valuable products (ethylene, propylene, aromatics, *etc*) *(40)*. Comprehensive statistical analyses on catalyst synthesis, composition, and performance towards the OCM reaction revealed that metal oxides and their binary and ternary combinations are beneficial in achieving high catalytic performance *(41)*. Specifically, analytic efforts have shown that high-performance binary and ternary catalysts composed of Mg and La are desired. Typically, alkali (Cs, Na) and alkaline-earth (Sr, Ba) metals are used as dopants to increase the selectivity of C2-hydrocarbons (ethane, ethylene, and acetylene), whereas dopants such as Mn and W have positive effects on catalytic activity *(41)*. To-date, thermal decomposition, precipitation, impregnation, sol-gel, and spray pyrolysis methods have been employed to synthesize these catalysts however, due to the thermodynamic/kinetic limitations of each approach, it is difficult to create homogeneous dispersions of multiple metals, especially at high catalyst loadings (>10 wt%). In this regard, our CTS method is an ideal and alternative method to synthesize supported HEA-NPs catalysts that possess a homogeneous elemental distribution for a range of catalytic applications, such as catalytic oxidative coupling of methane.

Catalytic car exhaust treatment. Three-way catalysts (TWCs) have been widely applied in stoichiometric-burn gasoline-powered vehicles to reduce tailpipe emissions, which consists of hydrocarbons (HC), carbon monoxide (CO) and nitrogen oxides

(NO_x).*(42)* Traditionally, platinum-, palladium-, and rhodium-based (PtPdRh) ternary catalysts are installed in the catalytic convertor to reduce tailpipe pollutant emissions. However, the traditional PtPdRh ternary catalyst is only capable of eliminating all pollutants at high temperatures, typically above 400^{o}C *(43)*. Starting in 2017, US federal regulations have mandated significant improvements in fuel economy, and thus, demand catalysts to function at low temperatures (<150^{o}C; deemed the 150^{o}C challenge) *(44)*. Ceria/zirconia (CeO_2/ZrO_2) mixed oxides have become an essential component in TWC catalysts due to their unique oxygen storage and release properties, which can enhance the intrinsic catalytic activity of PtPdRh and minimize overall fuel usage *(42)*. Therefore, PtPdRhCeZr catalysts synthesized by our CTS method can be selectively oxidized (i.e. the non-noble metals, Ce and Zr, would preferentially oxidize to create ceria/zirconia within the HEA-NPs). If successful, this CTS platform could create a TWC that could meet the new legislation requirements for vehicle emission control.

Selective ammonia oxidation to NO_x ($NO+NO_2$). This is the reaction we chose to demonstrate our high-entropy alloy nanoparticles for. In the current work, we have demonstrated two HEA-NPs catalysts with less Pt and higher performance in the selective oxidation of ammonia to nitrogen oxides (see detailed results above and in Fig. 5 in Maintext). Since we can achieve arbitrary alloy combinations of dissimilar metals, there is still great potential in terms of designing and optimizing the catalysts (e.g. completely eliminating Pt) with our CTS method.

Scalability of our CTS method

We have carried out additional experiments in order to justify the scalability of the reported CTS method for the synthesis of HEA-NPs. The following list summarizes how we addressed scalability:

- CTS is a simple, two-step method: (a) solution-based loading of precursors and (b) rapid heat treatment, both of which are scalable (see below for detailed discussion).
- We have extended the CTS method from carbon nanofiber (CNF) films to 3D bulk substrates (e.g. carbonized wood), which demonstrated a 100-fold increase in nanoparticle production without sacrificing the quality of the nanoparticles.
- The CTS method can be extended from Joule heating to non-contact radiation heating, which may enable roll-to-roll production and can be further expanded to a flow-synthesis process (as long as the merits of rapid heating can be achieved).

1. Features of our CTS method and demonstration of its potential scalability:

Our rapid, high-temperature carbo-thermal shock method offers promise in terms of scalable HEA-NP synthesis. A typical CTS synthesis procedure is two steps:

Solution-based salt precursors are conformally coated on the carbon surface. Specifically, certain solvents (e.g. ethanol) lead to enhanced wettability on carbon and overall, a more uniform dispersion of precursors. Experiments also show that the same precursor salts used months later yielded similar nanoparticle sizes, compositions, and structures. Thus the precursor solutions can be recycled (important for industrial manufacturing) and exhibits reproducibility in terms of the synthesized nanoparticles.

The precursor-loaded carbon film is then joule heated to ~2000 K rapidly followed by

ultrafast quenching. Uniformly distributed HEA-NPs are formed in situ on the carbon surface. The entire process takes ~55 milliseconds with a quenching rate of ~10^5 K/s.

From a manufacturing point of view, the CTS method has the following advantages:

- Step 1 (precursor loading) is completely scalable; Step 2 is fast (only 55 ms) and thus, comparable with roll-to-roll processes (similar to radiation heating as described later).
- The process can be done with 3D substrates with a much higher loading of precursors; in this case, a high yield of HEA-NPs can be produced (details in the next section on 3D wood-based carbon).
- The maximum temperature (up to 3000K) is much higher than the decomposition temperature of nearly any metal salt, which can lead to "mixing" of many types of metals.
- The fast and tunable cooling rate is capable of producing both: equilibrium phase-separated structures (slow cooling) and high entropy solid solution structures (rapid quenching).
- The fabrication process shows universality, i.e. the same setup can be used to synthesize HEA-NPs with different compositions by altering the precursors deposited on the carbon substrate.
- The in situ formed HEA-NPs on supports have direct applications (e.g. for ammonia oxidation).
- Therefore, we consider our CTS as a scalable process with excellent tunability in terms of nanoparticle composition, structure, and elemental ratios. Our CTS method offers a combinatory approach that can be widely used in materials synthesis/design.

2. Extension of our CTS method from CNF films to 3D bulk substrates (e.g. carbonized wood)

When a 3D carbon support is used, a much higher mass loading of precursors can be achieved, which leads to a 100-fold increase in nanoparticle production. For this purpose, we chose carbonized wood (Fig. S73) due to the following advantages:

Wood-based carbon has a unique microstructure with open channels in the thickness direction (>500 μm), which enables rapid and uniform precursor loading throughout the sample.

The open channels are connected horizontally by the sidewall pits, which leads to 3D interconnected pathways for gas diffusion.

Wood is low cost and the most abundant biomass.

The low tortuosity and interconnected structure ensure a uniform loading of precursors throughout the wood, which results in uniform deposition of HEA-NPs. Quinary HEA-NPs (PtPdRhRuCe) were synthesized within carbonized wood. As shown by the SEM images, HEA-NPs are uniformly distributed throughout the wood sample (Fig. S73). This finding was determined by checking several spots on the carbonized wood samples along the thickness direction. It is apparent that uniform nanoparticle sizes and distributions are achieved throughout the 3D substrate by CTS. Thus, the wood carbon substrate substantially increased the effective particle production of HEA-NPs.

When the thickness of the wood carbon increases from 500 μm to 5000 μm (5 mm),

the precursor loading increases from 60 μmol/cm^2 to 600 μmol/cm^2, respectively (Fig. S74). Consequently, the amount of synthesized HEA-NPs on the wood carbon is ~10 mg/cm^2 and ~100 mg/cm^2, which corresponds to a 10-fold and 100-fold increase compared to the CNF films (6 μmol/cm^2 and ~1 mg/cm^2). We also acquired STEM elemental maps to confirm the high entropy mixing of these HEA-NPs synthesized within the wood substrate. Note that all 5 elements are uniformly distributed throughout the synthesized nanoparticles (Fig. S74b). This is similar to the HEA-NPs synthesized on CNFs via the CTS method that shows high entropy mixing (Fig. S74c). Thus, regardless of the conductive substrate, high entropy alloy structures can be readily achieved.

In short, we have effectively increased the production of HEA-NPs by 100-fold by replacing the CNF film with a 3D carbonized wood substrate without sacrificing the nanoparticle quality.

3. Extension of the CTS method from Joule heating to radiation heating, which may enable roll-to-roll production:

The essence of the CTS method for HEA-NP synthesis is three-fold: (1) high temperature, (2) short duration and (3) fast quenching. While electrical Joule heating is an ideal strategy for precise control of temperature, duration and cooling rate, other rapid heating strategies (radiative heating, aerosol-spray, microwave heating, *etc*) are also possible as long as the merits of the CTS process are maintained. Specifically, all methods should minimize the high temperature duration.

The CTS method itself can be extended to rapid radiative heating for scalable/continuous manufacturing by eliminating electrode and contact fabrication, which is normally required for the Joule heating process. We envision roll-to-roll manufacturing of HEA-NPs on a carbon support can be achieved through radiation-based heating (Fig. S75a). The precursor loading can be easily achieved through a "coating-drying" method. As the moving film passes through the heating zone, it experiences thermal shock in a similar manner to the Joule heating process. Rapid heating (or thermal shock duration) can be controlled by the sample transfer process through the hot zone. Specifically, the duration is a function of the heating zone length and sample transfer speed ($t = L/v$), which are parameters that can be easily controlled on an assembly line.

As a proof of concept, Pt nanoparticles can be synthesized through rapid radiative heating of a CNF film using a radiative heating source (Fig. S75b-f). The CNF film loaded with salt precursors was placed on top of a carbon felt, which is heated to high temperature via Joule heating for 1 second and then quenched. Instead of directly heating the sample via Joule heating, the CNF film experienced rapid radiative heating using a heating source positioned below the substrate. Densely populated nanoparticles were synthesized in situ on both sides of the film (thickness of ~30 μm), which indicates the effectiveness of radiation-based heating as well as the good thermal conduction of the CNF networks (Fig. S75e-f).

The aforementioned improvements in terms of substrates (e.g. 3D wood-based carbon) and scalable, rapid heating methods are not exclusive. Further potential in terms of scalable CTS processes can be envisioned as long as the merits of the process remain intact.

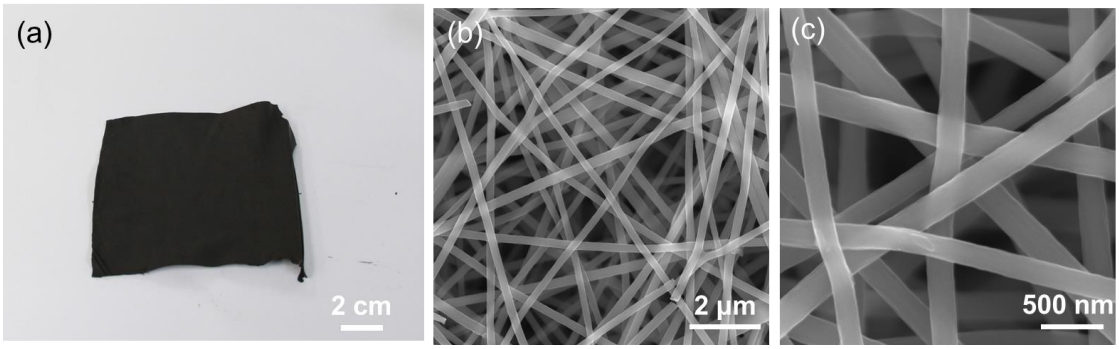

Fig. S1.

CNFs used as the carbon support. (a) Digital image and (b-c) SEM images of PAN-derived carbon nanofibers, showing uniform nanofiber sizes and an open network structure.

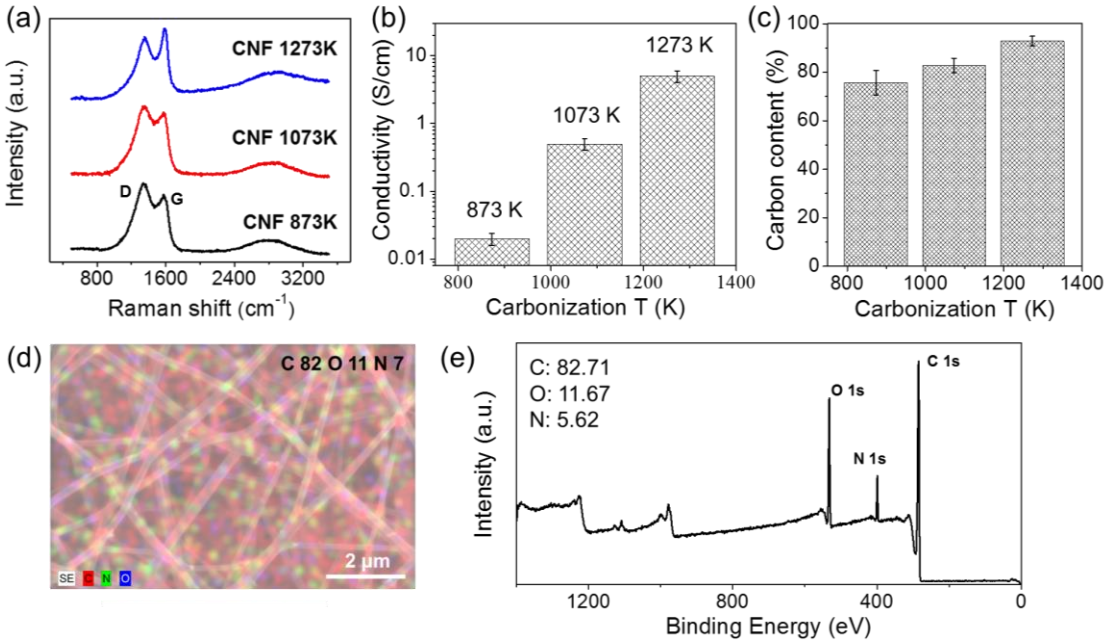

Fig. S2.

Properties of CNF with different carbonization temperatures. (a) Raman spectra and (b) conductivity of CNF films carbonized at different temperatures: 873 K, 1073 K, and 1273 K. (c) Carbon content in CNFs carbonized at different temperatures, identified by point maps via SEM. (d) Elemental map of the carbon, nitrogen, and oxygen and (e) XPS profile of CNF carbonized at 1073 K.

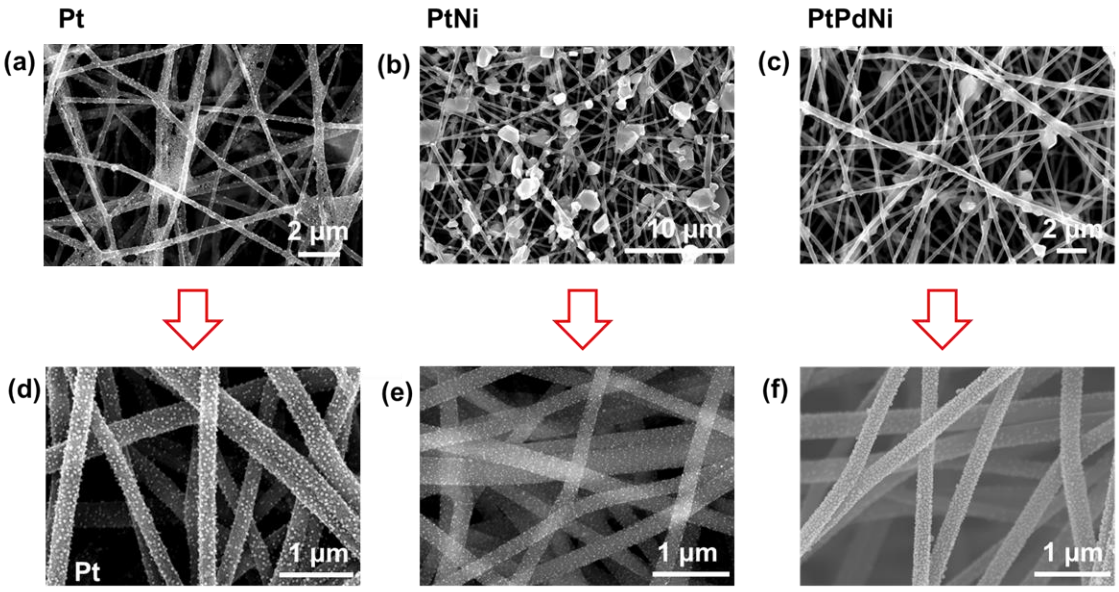

Fig. S3.

SEM images of the decorated CNF microstructure before and after CTS: (a) Pt, (b) PtNi, and (c) PtPdNi precursors on CNFs before CTS as well as the synthesized (d) Pt, (e) PtNi, and (f) PtPdNi nanoparticles after CTS.

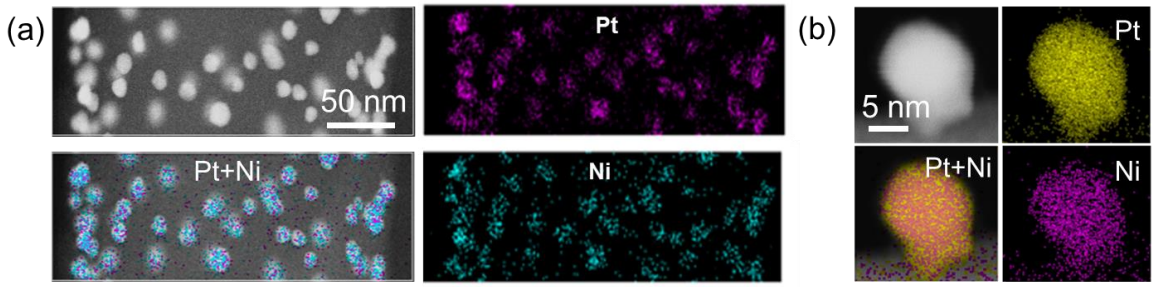

Fig. S4.

Alloy formation of PtNi at (a) low magnification, and (b) on an individual nanoparticle level. Each magnification level confirms the uniform distribution of each element (Pt and Ni) as well as the formation of alloyed structures.

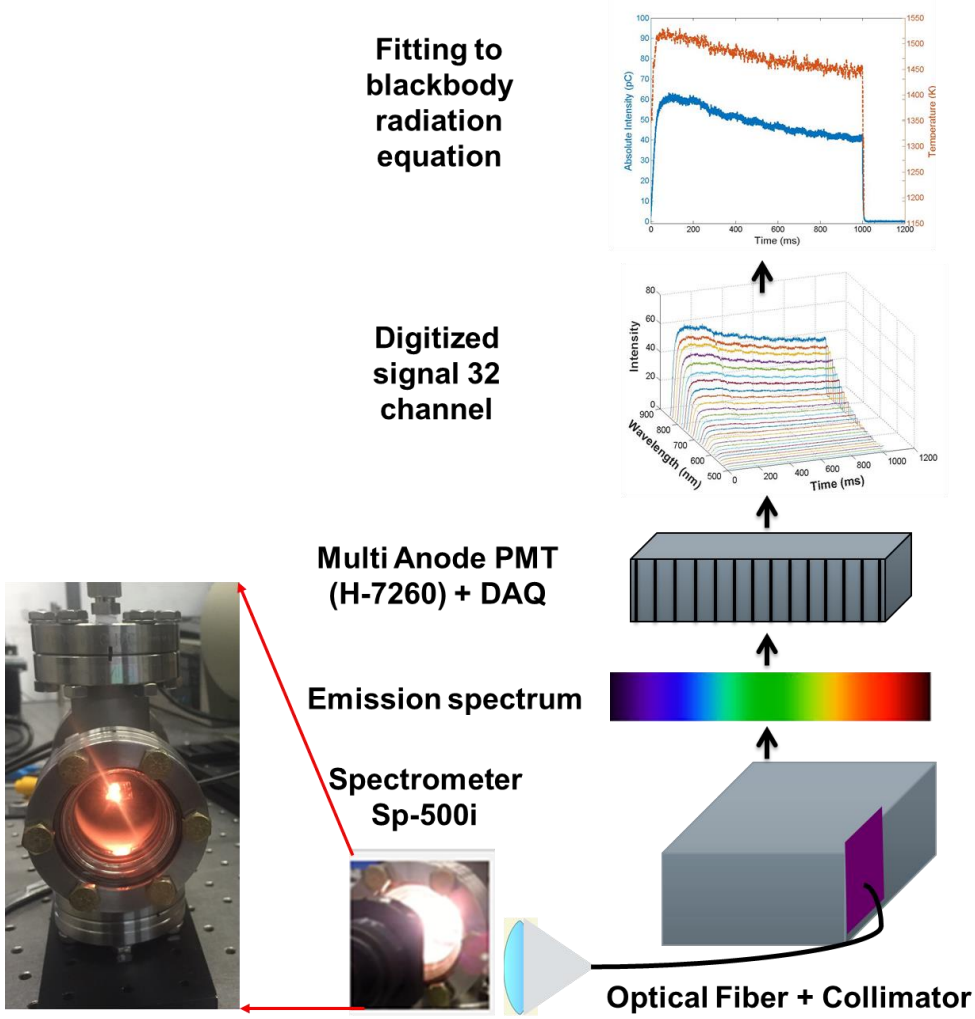

Fig. S5.

Schematic configuration of a time-resolved pyrometer for spectrum collection during the rapid, high temperature CTS process.

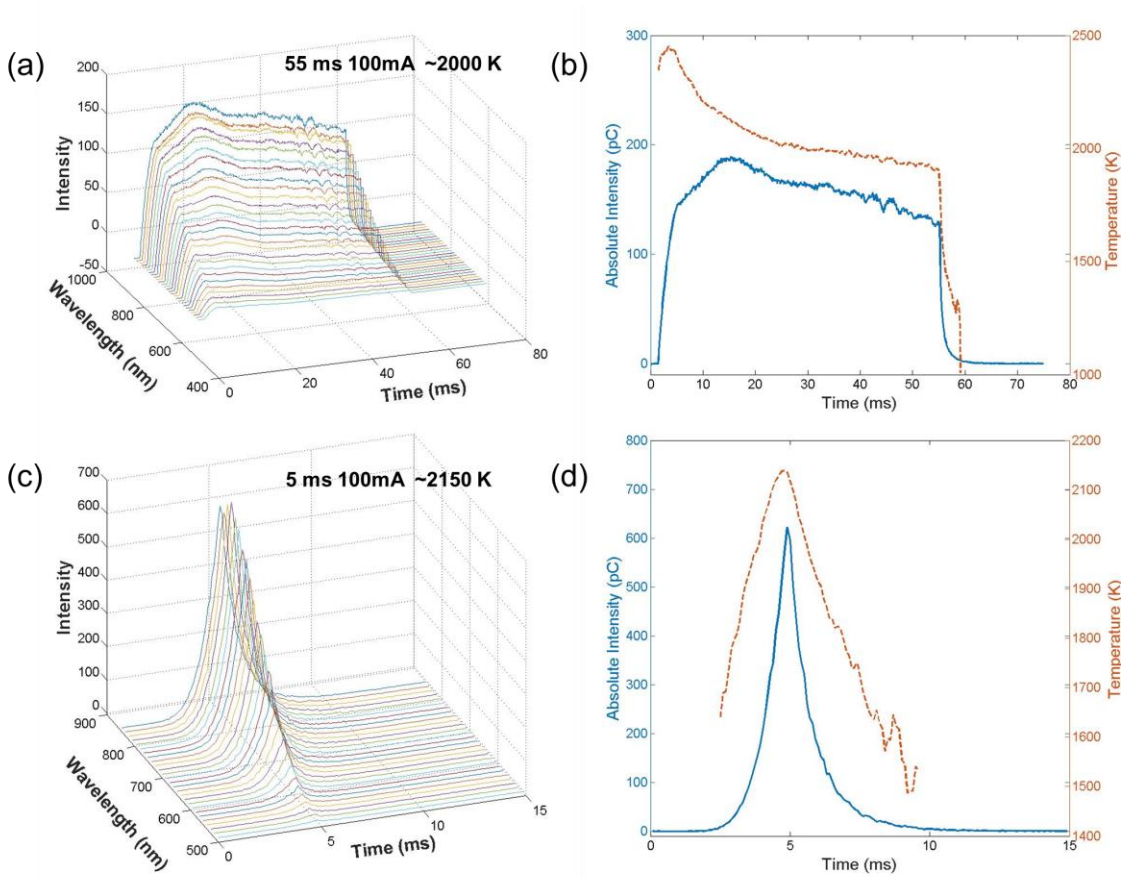

Fig. S6.

Temporal lighting spectra and temperature fitting for the CTS method with various shock durations: (a-b) 55 ms pulse and (c-d) 5 ms pulse. These spectra were fitted to the blackbody radiation equation to acquire an approximate sample temperature.

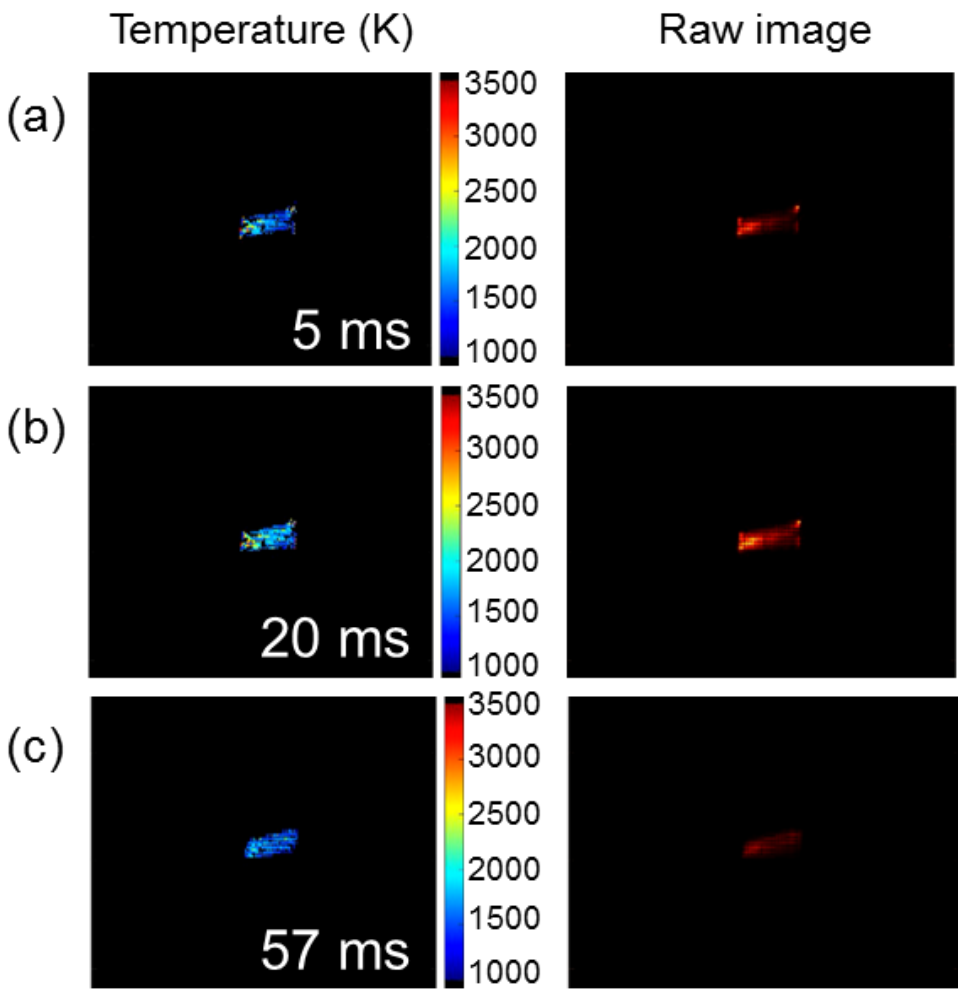

Fig. S7.

Spatial temperature evolution captured by a high-speed camera during a 55 ms thermal shock. (a-c) Temperature distribution in the CNF-based sample as well as the raw lighting images captured by the high-speed video camera at 5 ms, 20 ms, and 57 ms, respectively.

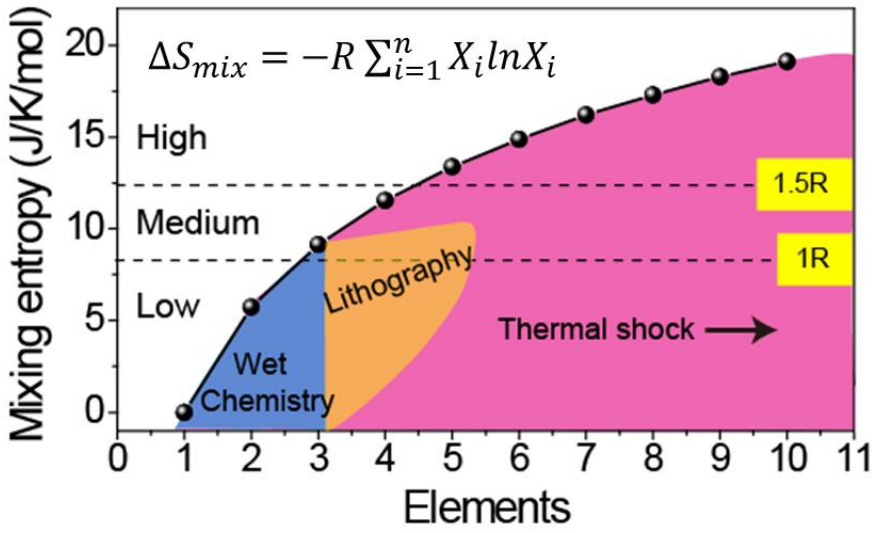

Fig. S8.

Calculation of configurational entropy of mixing and simple classification of low, medium, and high entropy regions*(16)*. MMNPs synthesized by different methods fall into different entropy regions (based on the classical definition of high entropy alloys).

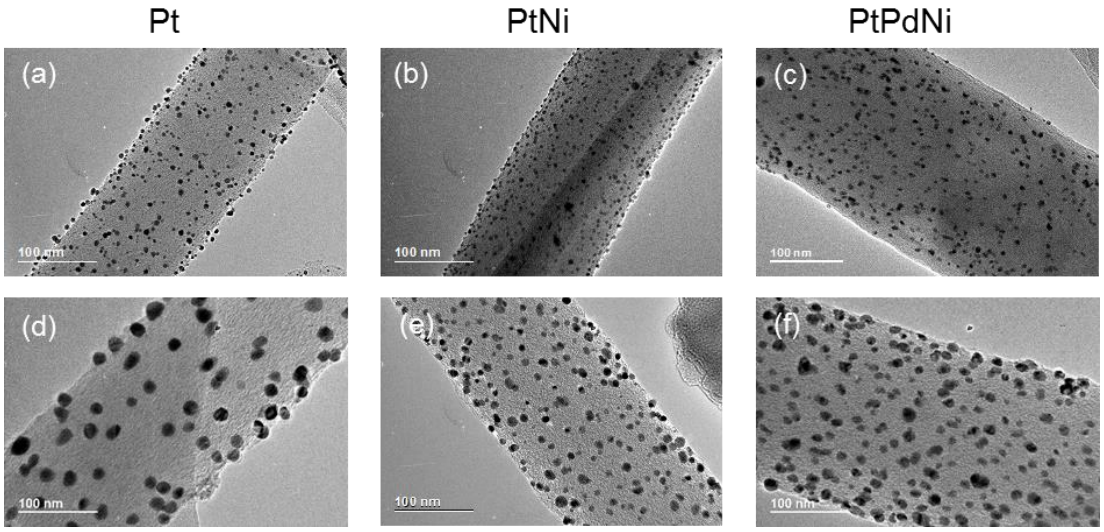

Fig. S9.

TEM images of 1-3 element nanoparticles on CNFs with different loading concentrations. Pt, PtNi, and PtPdNi with a precursor concentration of (a-c) 0.01 mol/L and (d-f) 0.05 mol/L per composition, respectively.

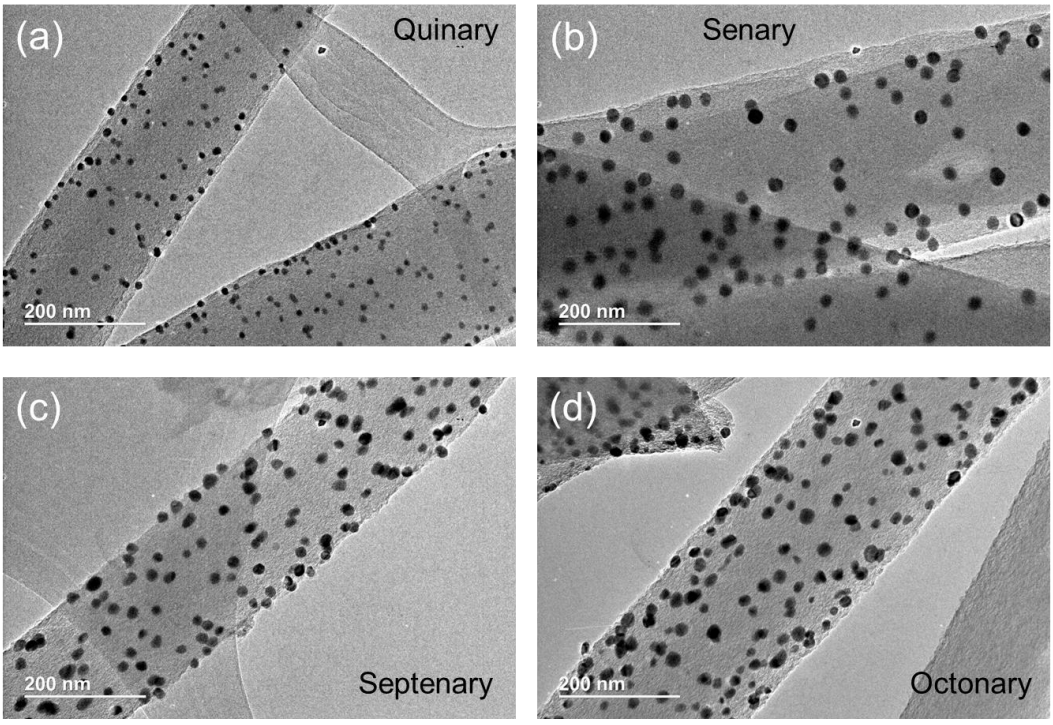

Fig. S10.

TEM images of high entropy nanoalloys (quinary, senary, septenary and octonary nanoparticles) composed of 5-8 elements, respectively. (0.01 mol/L each composition)

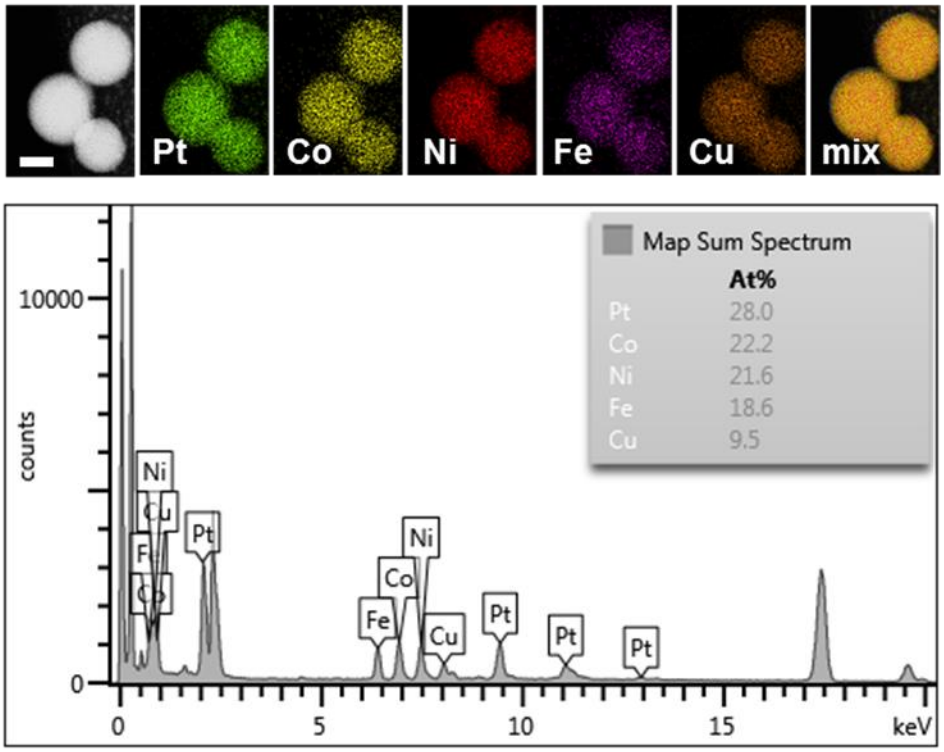

Fig. S11.
STEM elemental maps and corresponding spectrum for quinary PtCoNiFeCu.

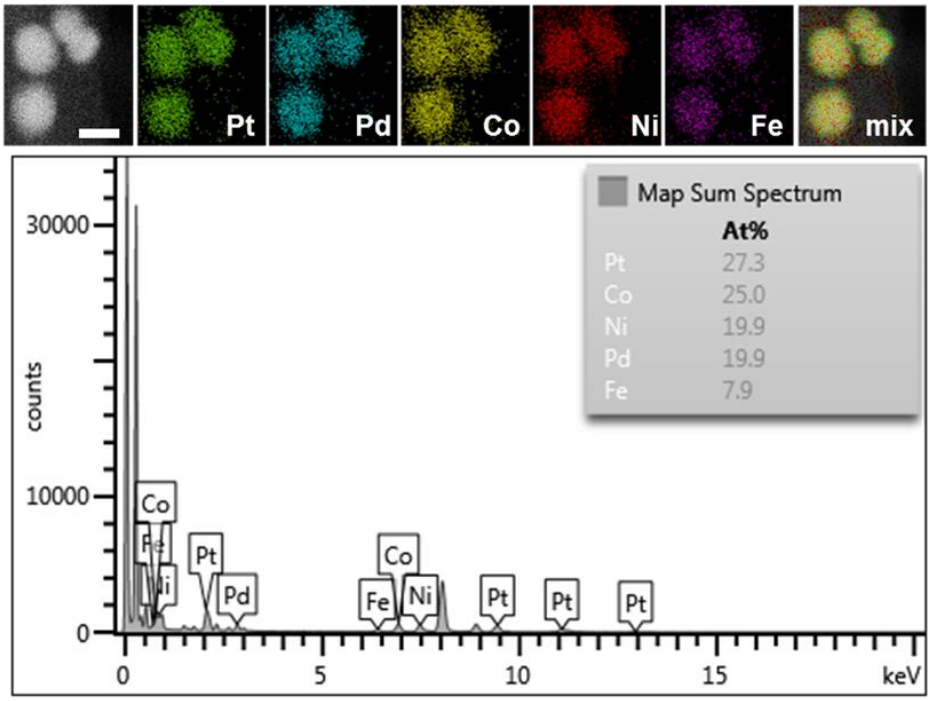

Fig. S12.
STEM elemental maps and corresponding spectrum for quinary PtPdCoNiFe.

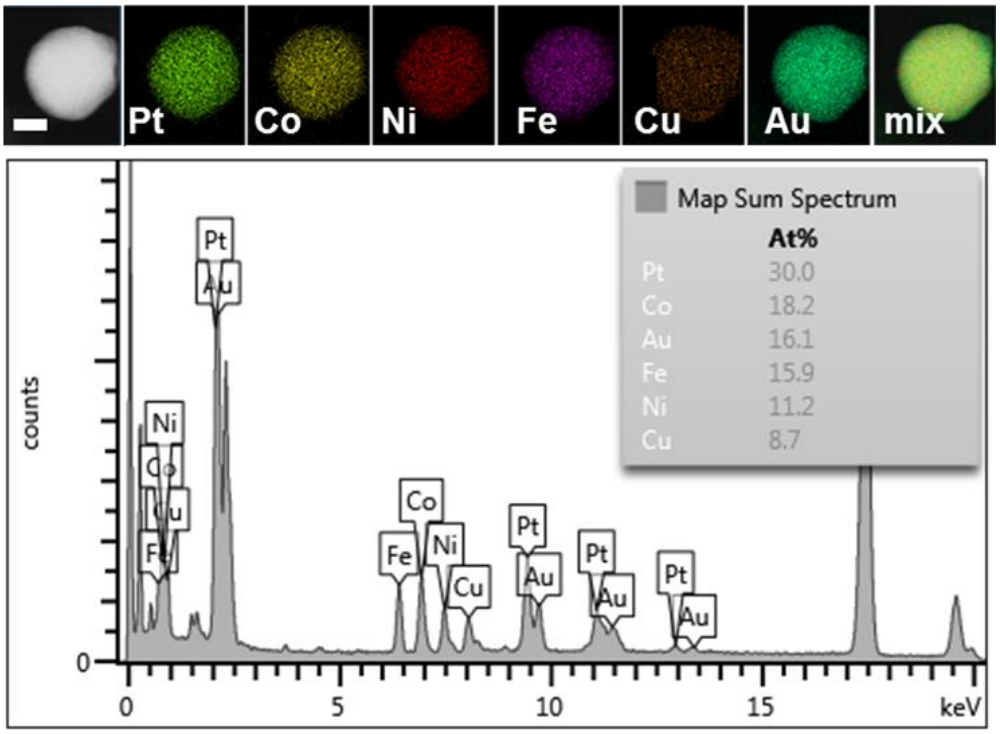

Fig. S13.
STEM elemental maps and corresponding spectrum for a senary PtCoNiFeCuAu.

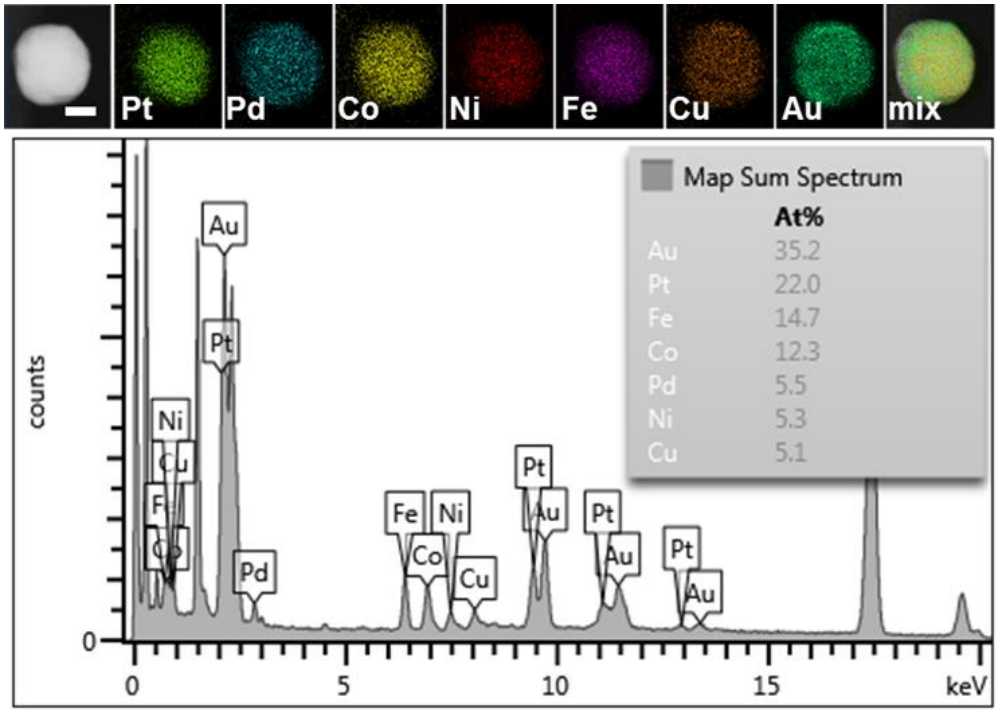

Fig. S14.
STEM elemental maps and corresponding spectrum for a septenary PtPdCoNiFeCuAu.

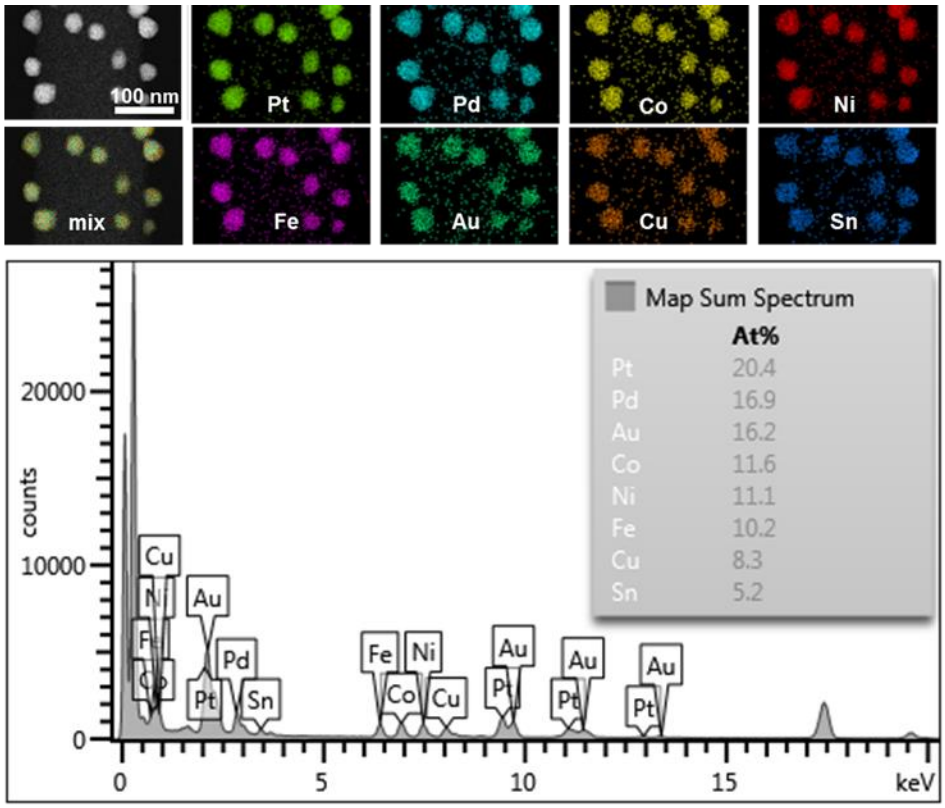

Fig. S15.

STEM elemental maps and corresponding spectrum at a low magnification for octonary HEA-NPs (PtPdCoNiFeAuCuSn).

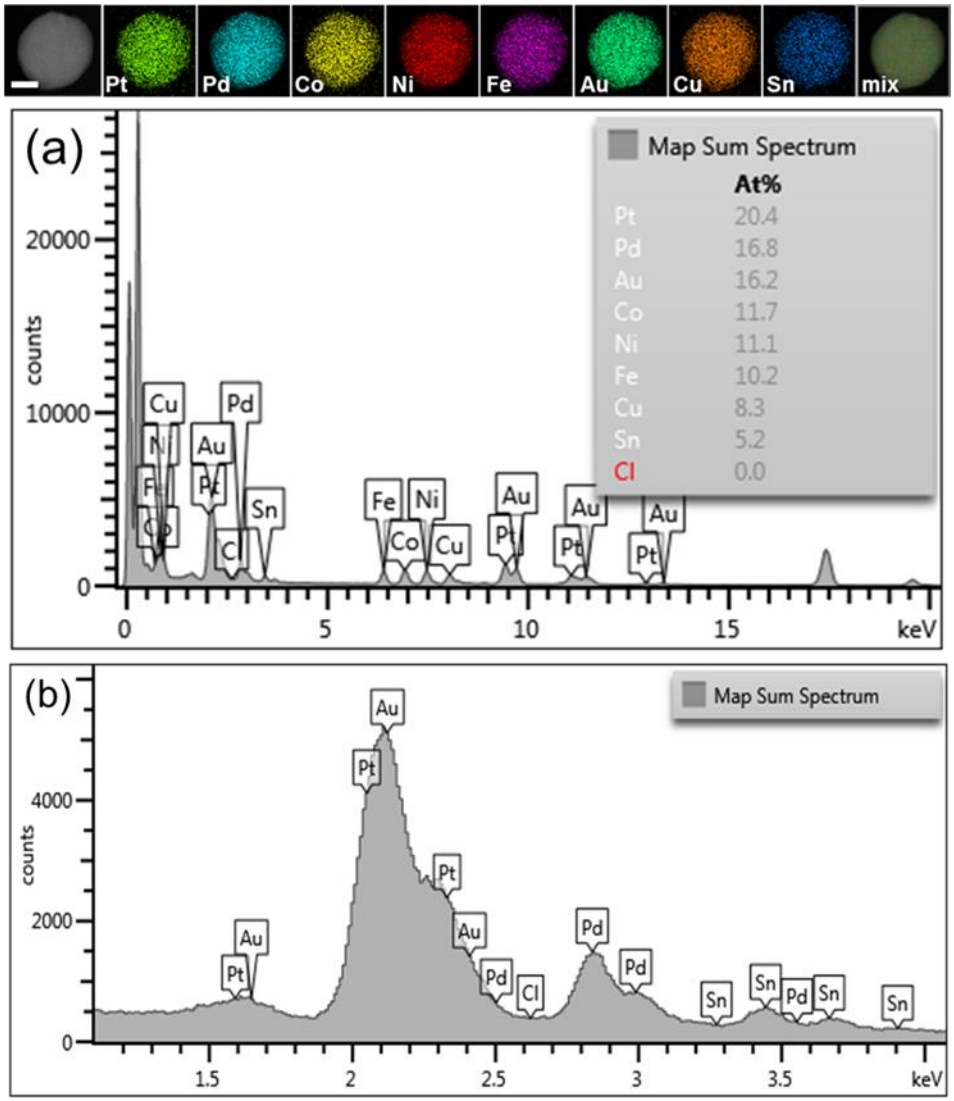

Fig. S16.

STEM elemental spectrum of an 8 element HEA-NP including Cl (from the initial precursor salt). (a) Full spectrum with elemental ratios of all 8 metals and Cl. (b) Enlarged region of the same spectrum in (a) however, the amount of Cl is below the detection limit.

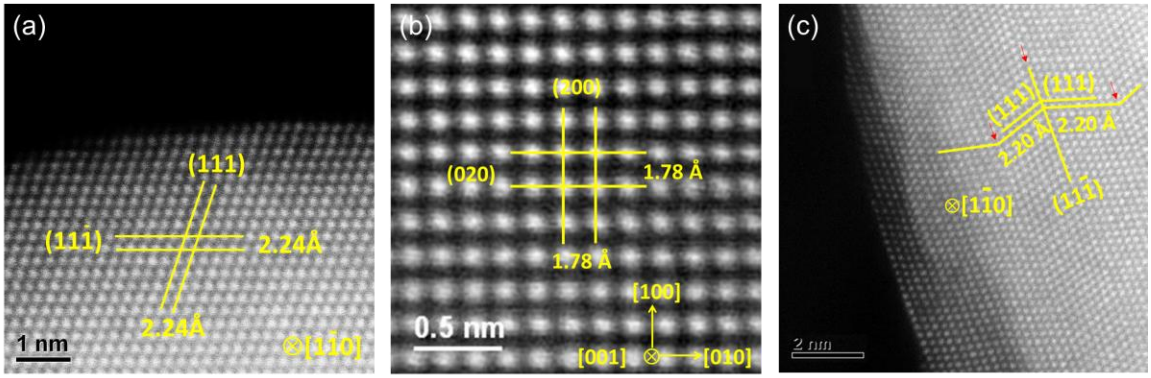

Fig. S17.

Atomic HAADF images of HEA-NPs for (a) PtNi, (b) FeCoNi, and (c) octonary PtPdCoNiFeAuCuSn nanoparticles. They are alloyed into FCC structures achieved by the CTS method.

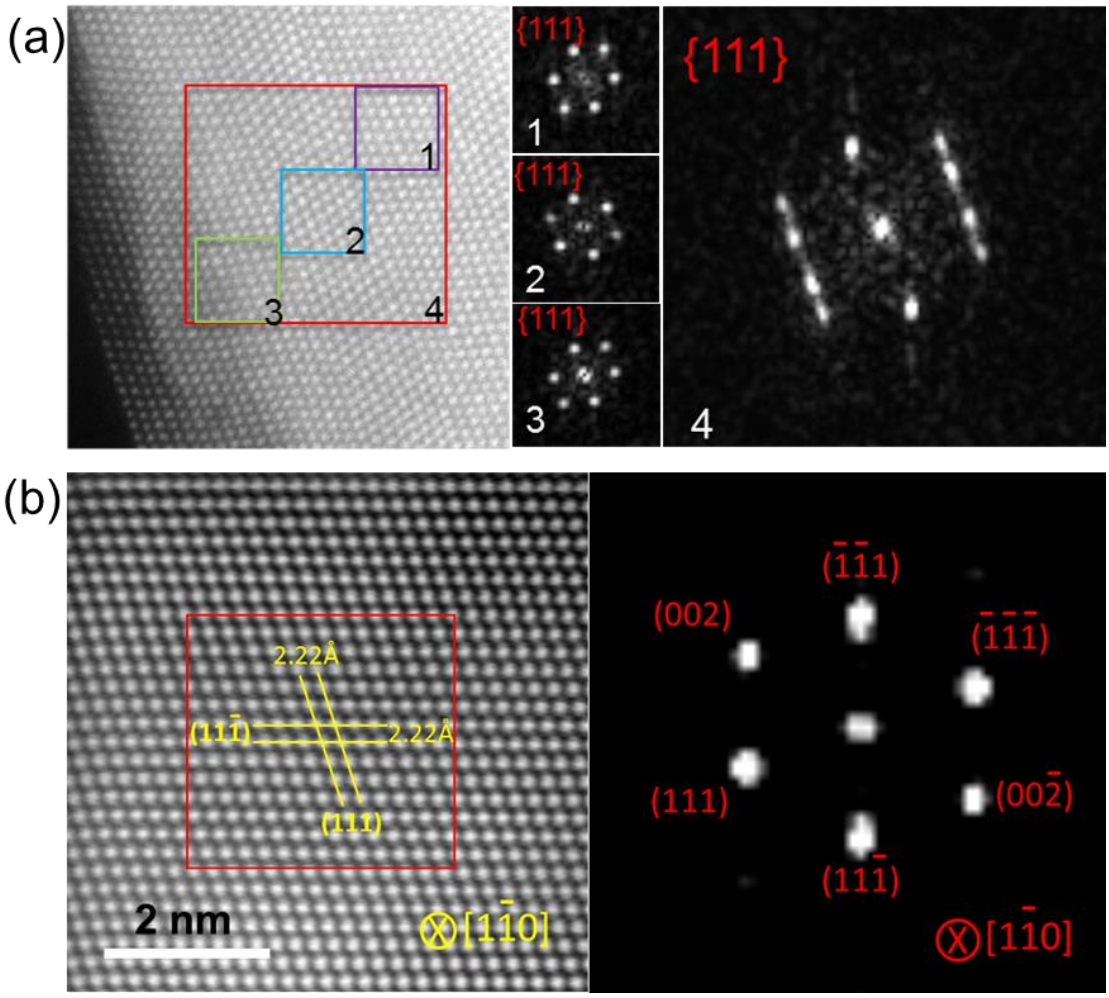

Fig. S18.

(a) FFT analysis of the above HAADF image for an octonary HEA-NP on an area (box 4) that contains twin boundaries as evidenced by analyses in boxes 1, 2, and 3. (b) A higher magnification atomic HAADF image of the octonary HEA-NP & FFT analysis of the red area.

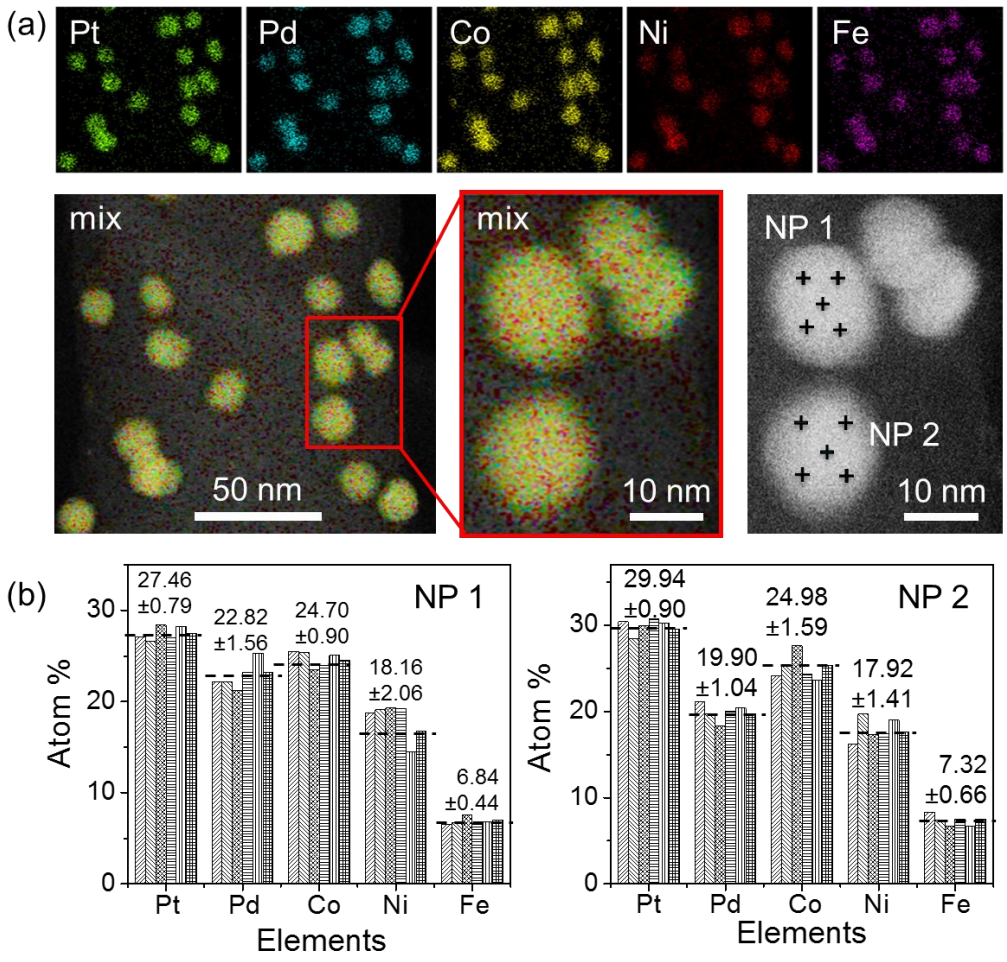

Fig. S19.

(a) Elemental maps for quinary HEA-NPs (PtPdCoNiFe) and the position of the point maps on individual nanoparticles. (b) Point-by-point elemental maps of PtPdCoNiFe, showing uniform distributions of each element throughout the entirety of both nanoparticles.

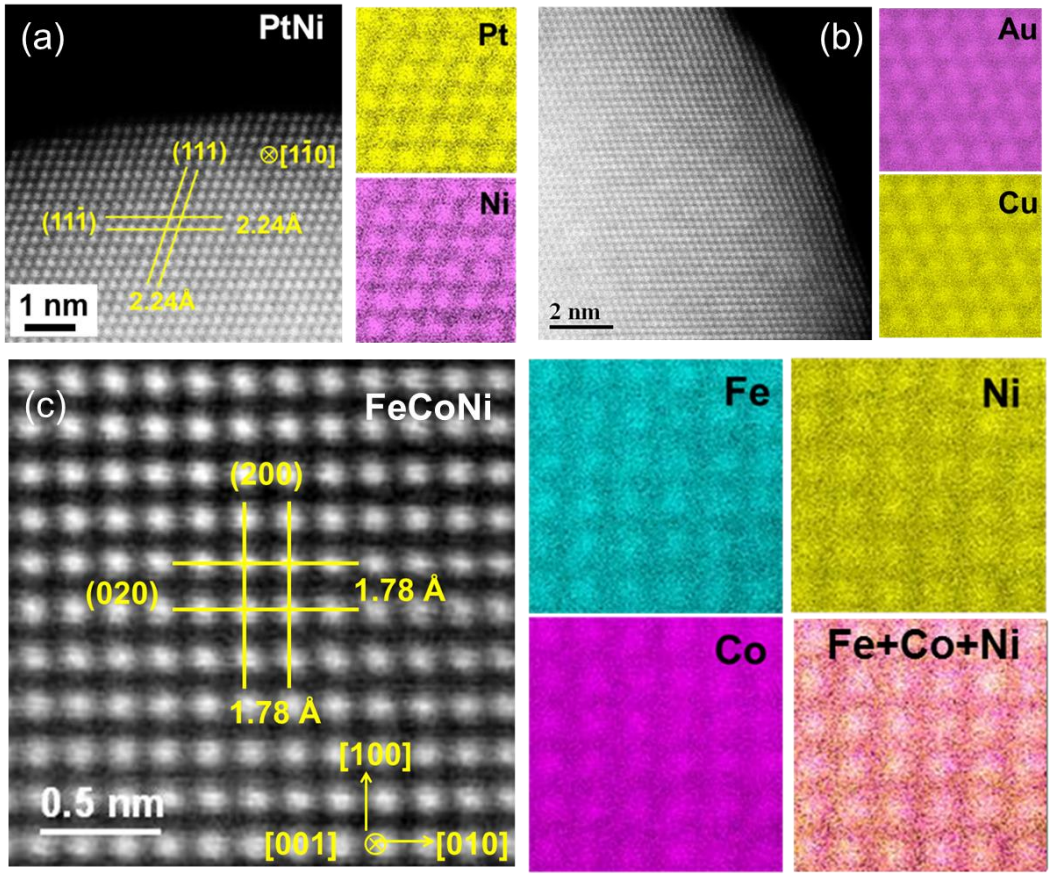

Fig. S20.

Atomic-scale HAADF-STEM images and STEM elemental maps for binary and ternary HEA-NPs (PtNi, AuCu, FeCoNi). These elemental maps show uniform elemental distribution within the mapped region at an atomic scale.

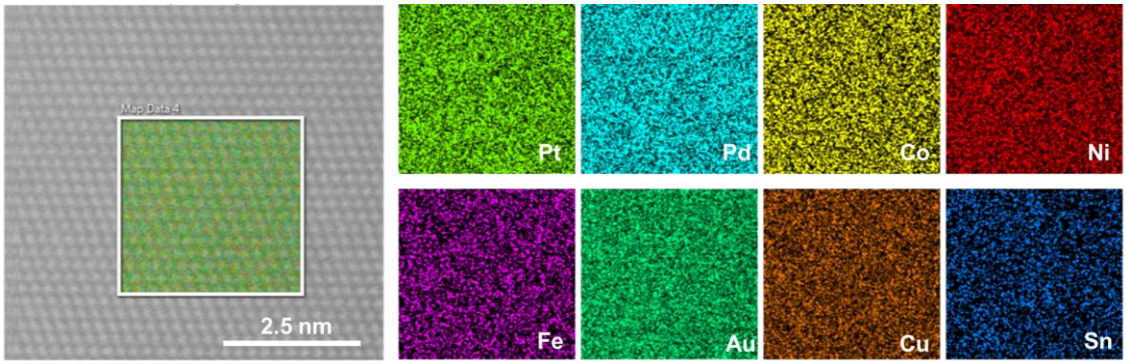

Fig. S21.

Atomic-level STEM elemental maps of an octonary HEA-NP (PtPdCoNiFeAuCuSn), which demonstrates uniform distributions of each element within the mapped region.

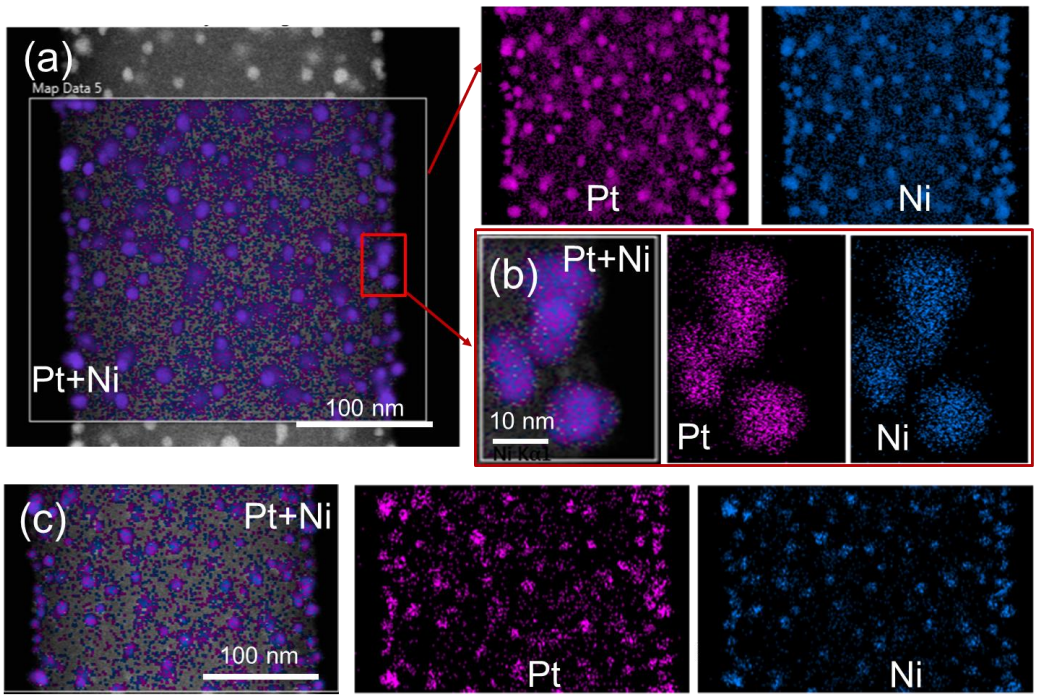

Fig. S22.

STEM elemental maps of binary (PtNi) alloys at (a) low magnification and (b) for a few nanoparticles. (c) Low magnification elemental maps at different sample regions, which demonstrates the compositional uniformity of the alloy nanoparticles via the CTS method.

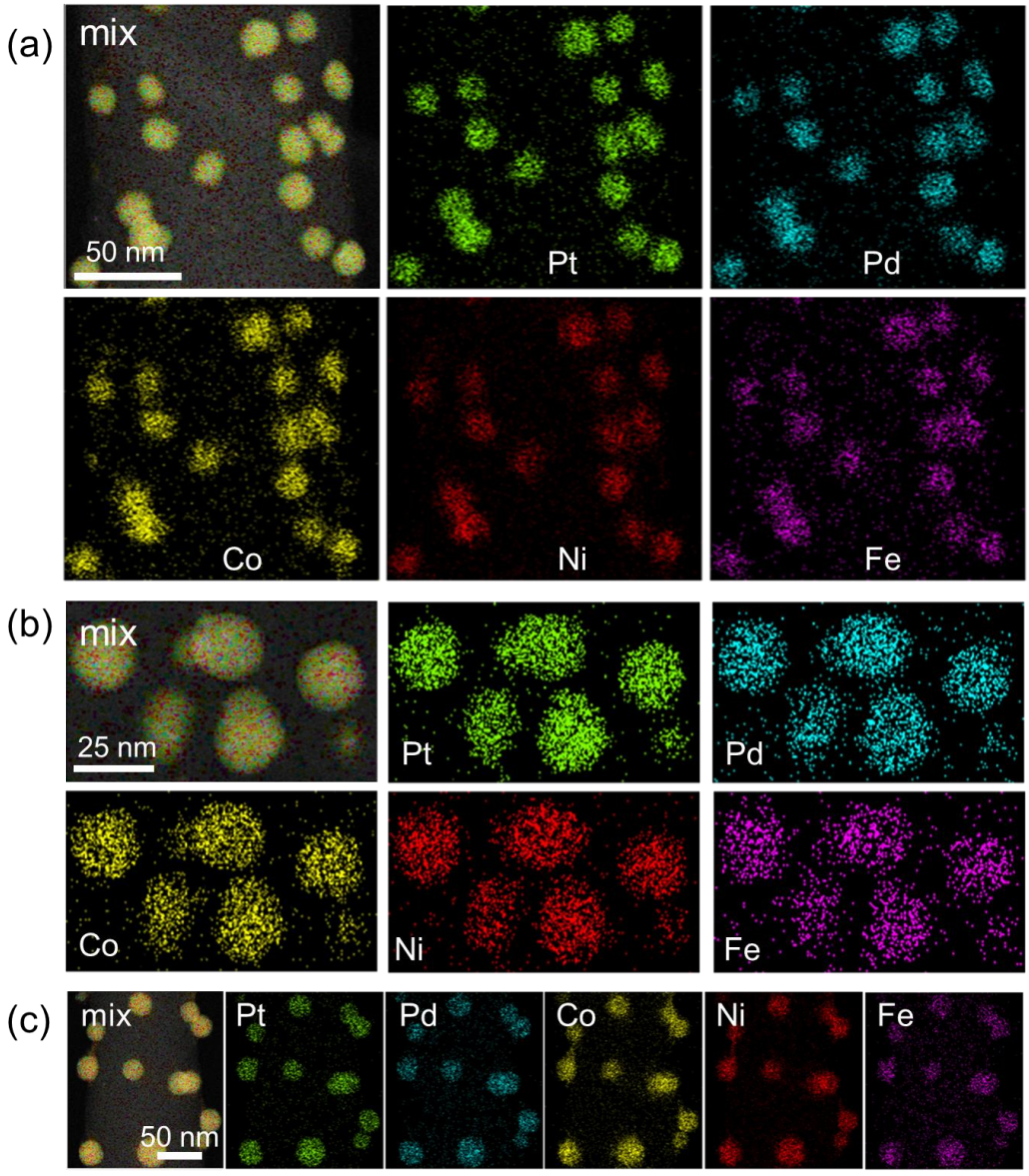

Fig. S23.

(a)-(c) STEM elemental maps of quinary HEA-NPs (PtPdCoNiFe) at low magnifications, which demonstrates the compositional uniformity of alloy nanoparticles synthesized via the CTS method.

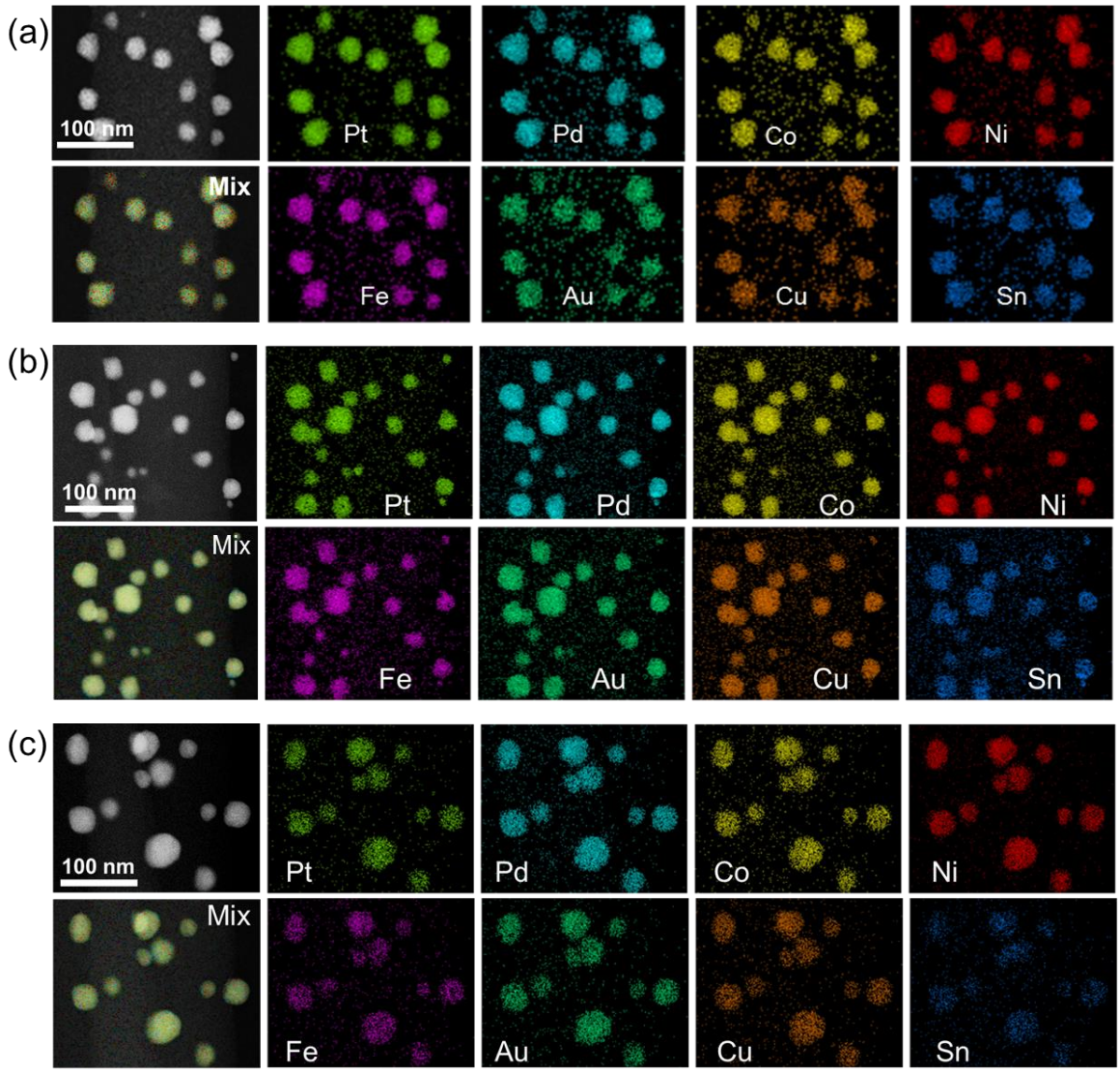

Fig. S24.

(a)-(c) STEM elemental maps of octonary HEA-NPs (PtPdCoNiFeAuCuSn) at low magnifications at different sample regions. Solid solution nanoparticles are readily achieved via the CTS method.

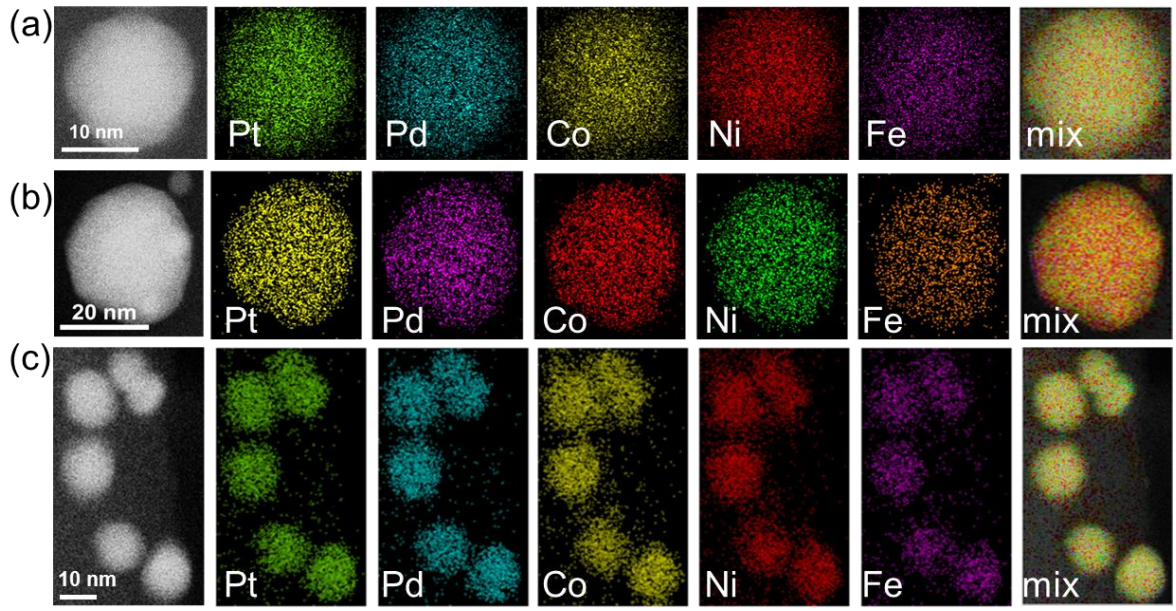

Fig. S25.

(a)-(c) STEM elemental maps of quinary HEA-NPs (PtPdCoNiFe) at different sample regions. There is a uniform distribution of elements throughout the nanoparticles, which confirms alloy formation.

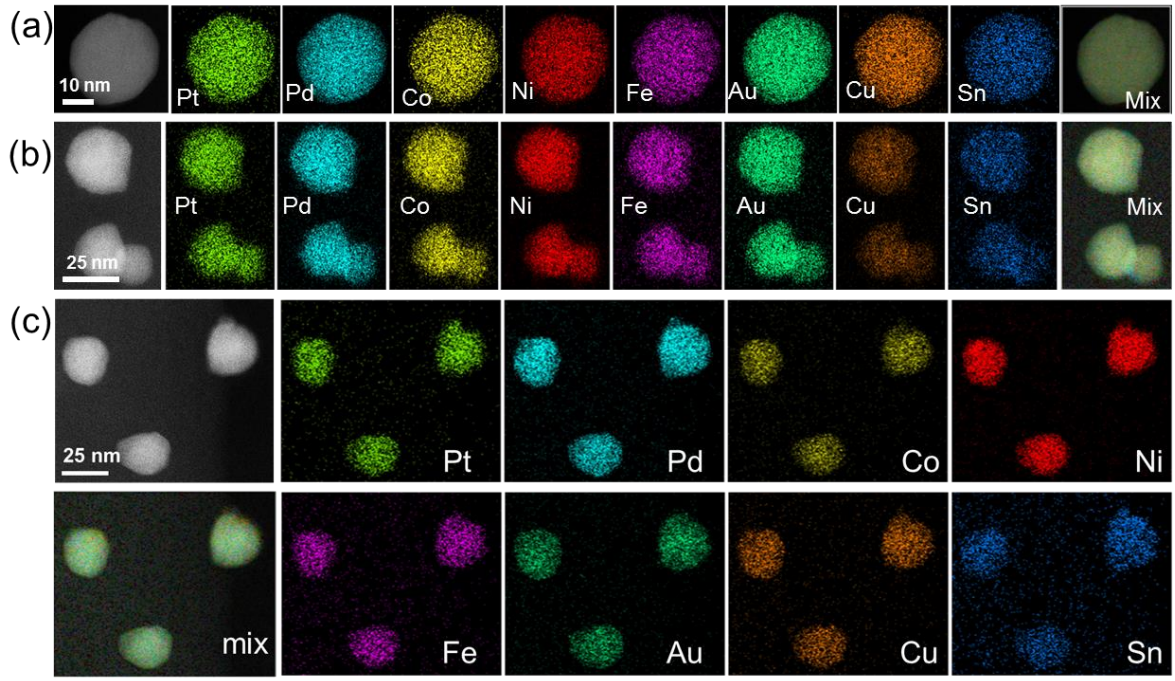

Fig. S26.

(a)-(c) STEM elemental maps of octonary HEA-NPs (PtPdCoNiFeAuCuSn) across different areas of the CNF sample. Similar to the quinary case, solid solution octonary nanoparticles show an even elemental distribution and thus, the formation of high entropy alloy nanoparticles.

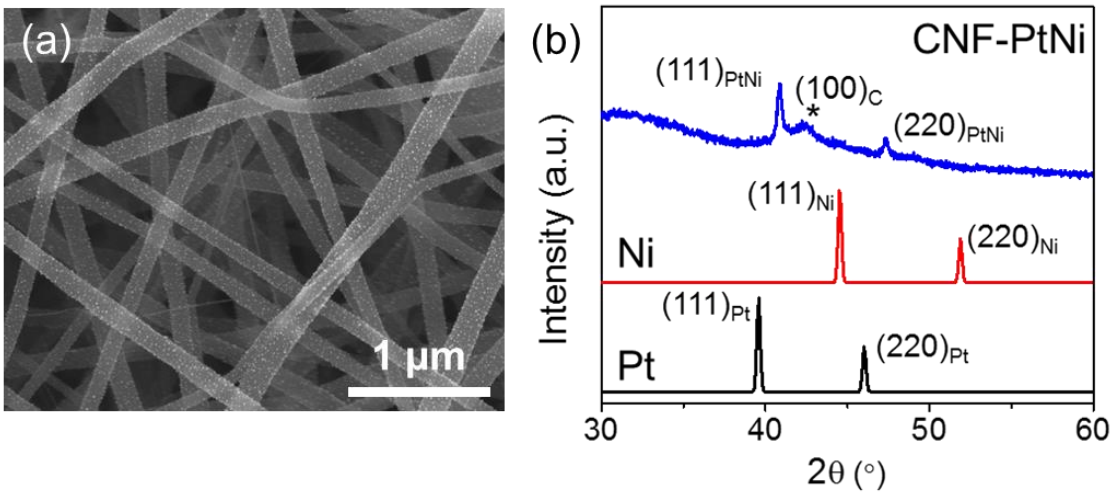

Fig. S27.

(a) SEM and (b) XRD pattern of binary alloy PtNi on CNFs. The SEM image shows the uniformly dispersed PtNi on CNF (on a micrometer scale). XRD confirms the binary PtNi are single-phase alloy structures by comparing to Pt and Ni XRD standards.

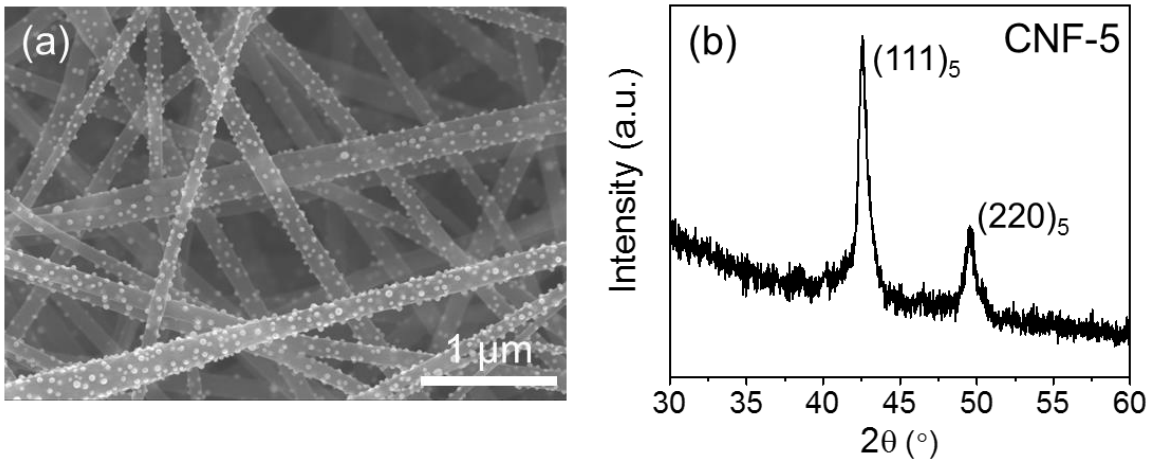

Fig. S28.

(a) SEM and (b) XRD pattern of quinary HEA-NPs (PtPdCoNiFe) on CNFs. The SEM image shows the uniform dispersion of nanoparticles on a micrometer scale. The XRD profile confirms the HEA-NPs are in single-phase structures without phase separation or intermetallic formation due to the absence of peak splitting (millimeter scale).

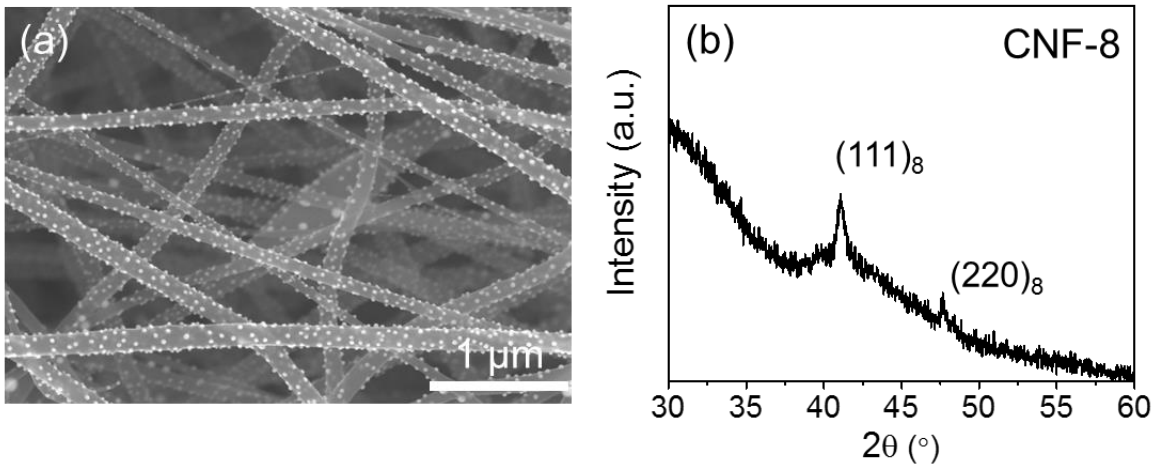

Fig. S29.

(a) SEM image and (b) XRD pattern of octonary HEA-NPs (PtPdCoNiFeAuCuSn) on CNFs. Similar to quinary HEA-NPs, the microscopy and x-ray results also prove uniformity in terms of particle dispersion and structure.

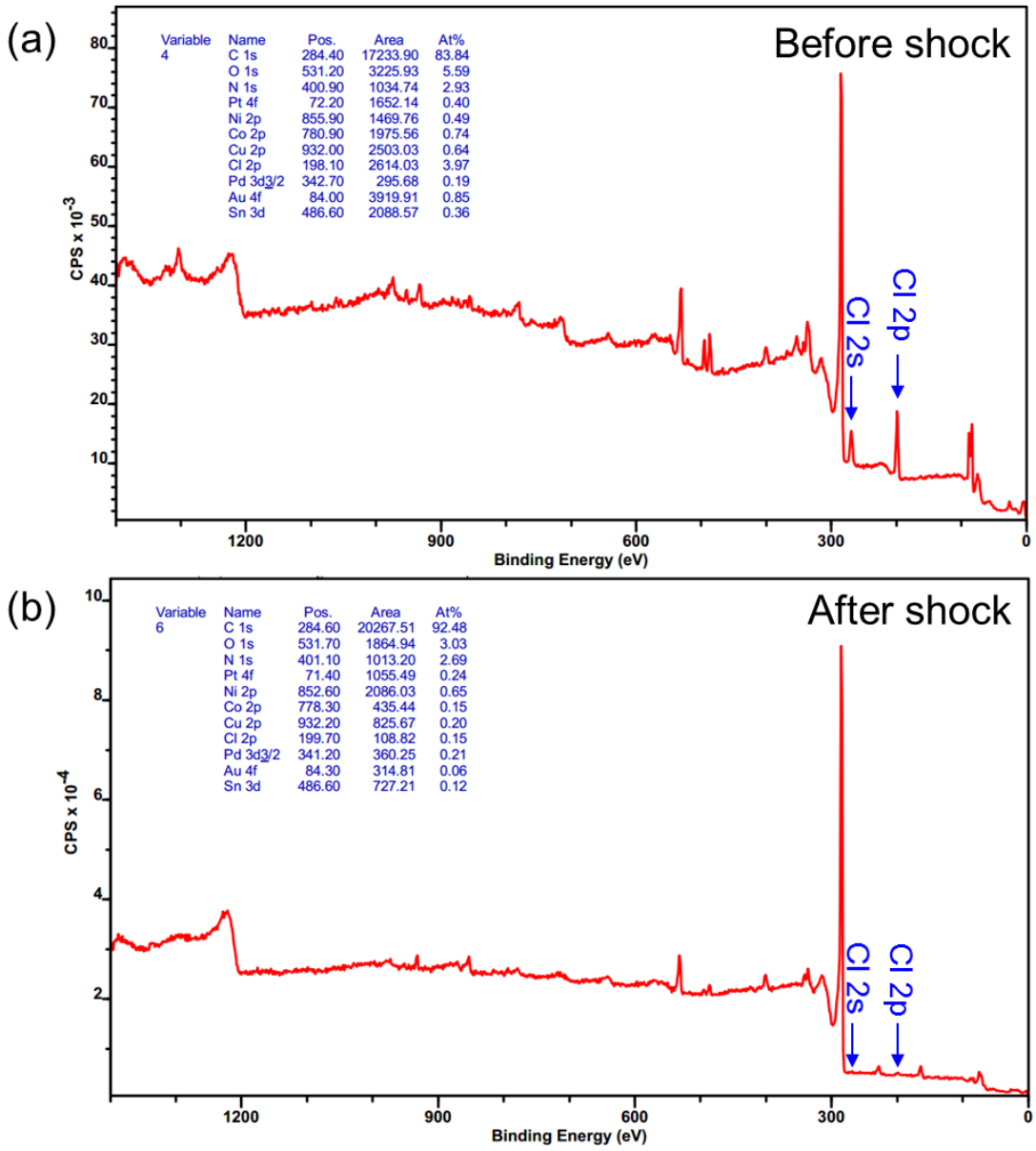

Fig. S30.

XPS spectra of 8-element (PtPdCoNiFeAuCuSn) precursor-loaded CNFs (a) before and (b) after the CTS process. The Cl peak becomes negligible after thermal shock as indicated by the arrows. From the fitted ratio, the Cl content dropped from ~4% to 0.15% due to the CTS process.

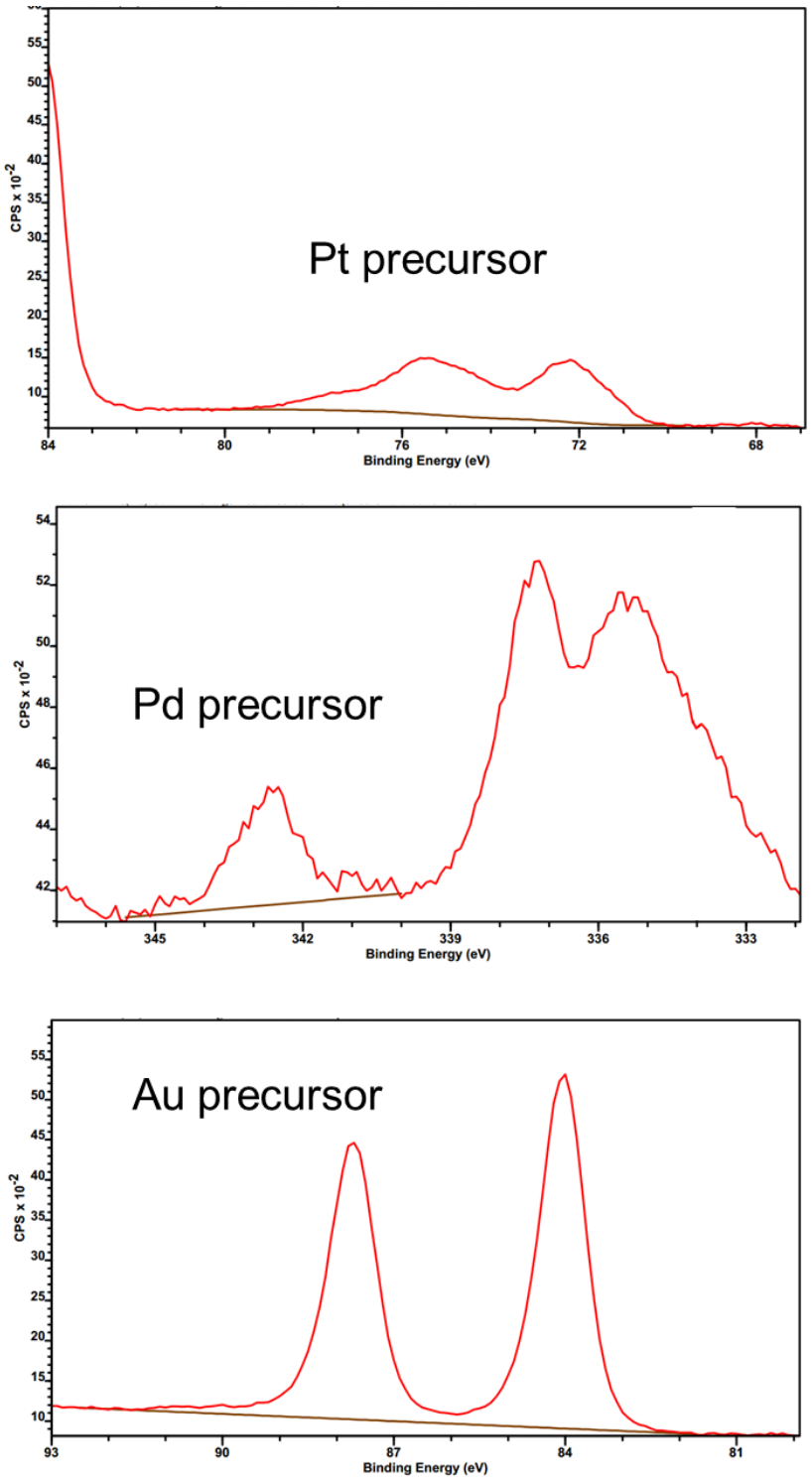

Fig. S31.

Characteristic XPS peaks for Pt, Pd, and Au from the 8 elemental precursors on CNFs before the thermal shock. The oxidized bonding states are apparent from these specific precursors.

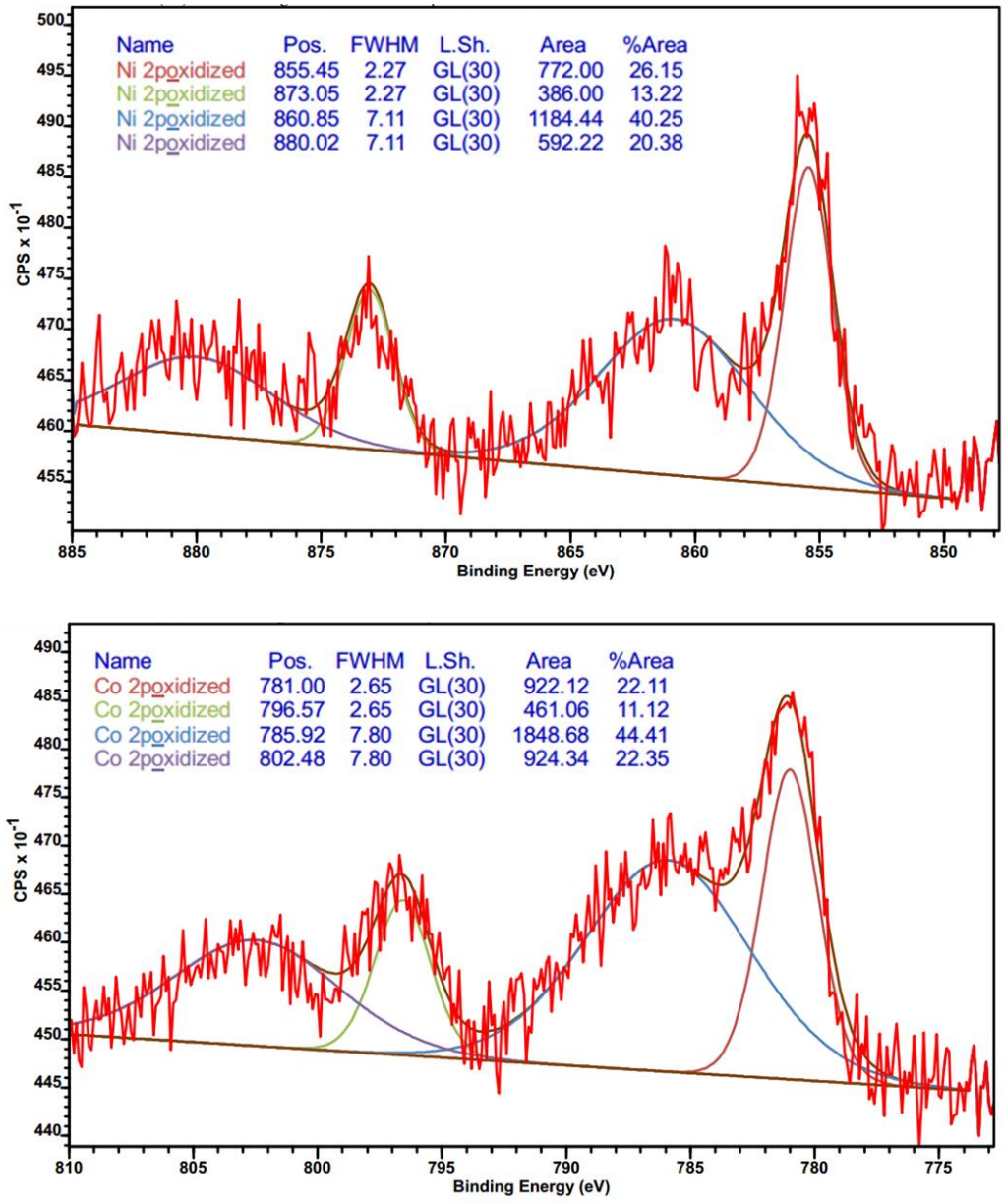

Fig. S32.

Characteristic XPS peaks for Ni and Co (with corresponding oxidized bonding states) from the 8 elemental precursor mixture on CNFs before the thermal shock.

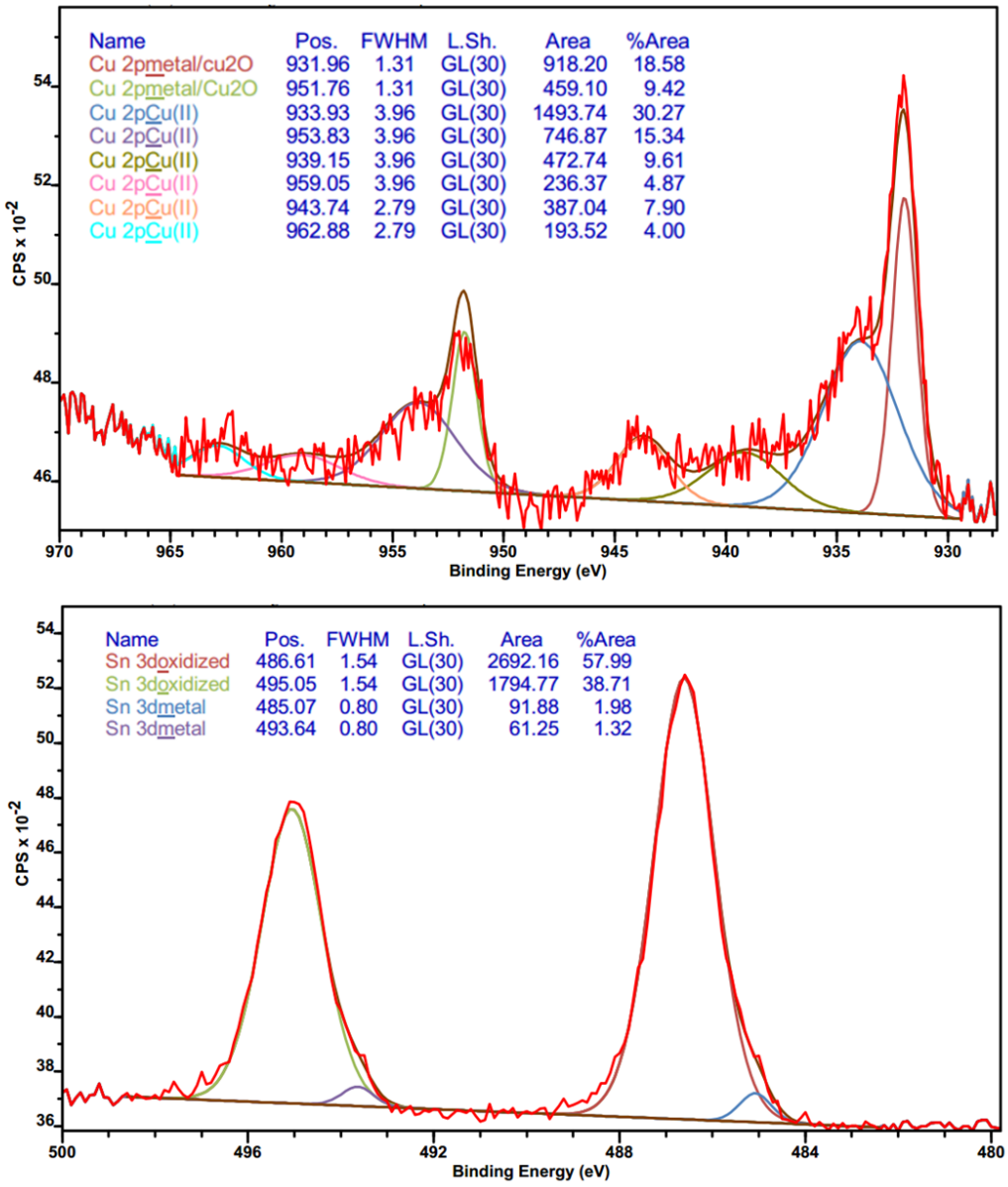

Fig. S33.

Characteristic XPS peaks for Cu and Sn (with corresponding oxidized bonding states) from the 8 elemental precursor mixture on CNFs before the thermal shock.

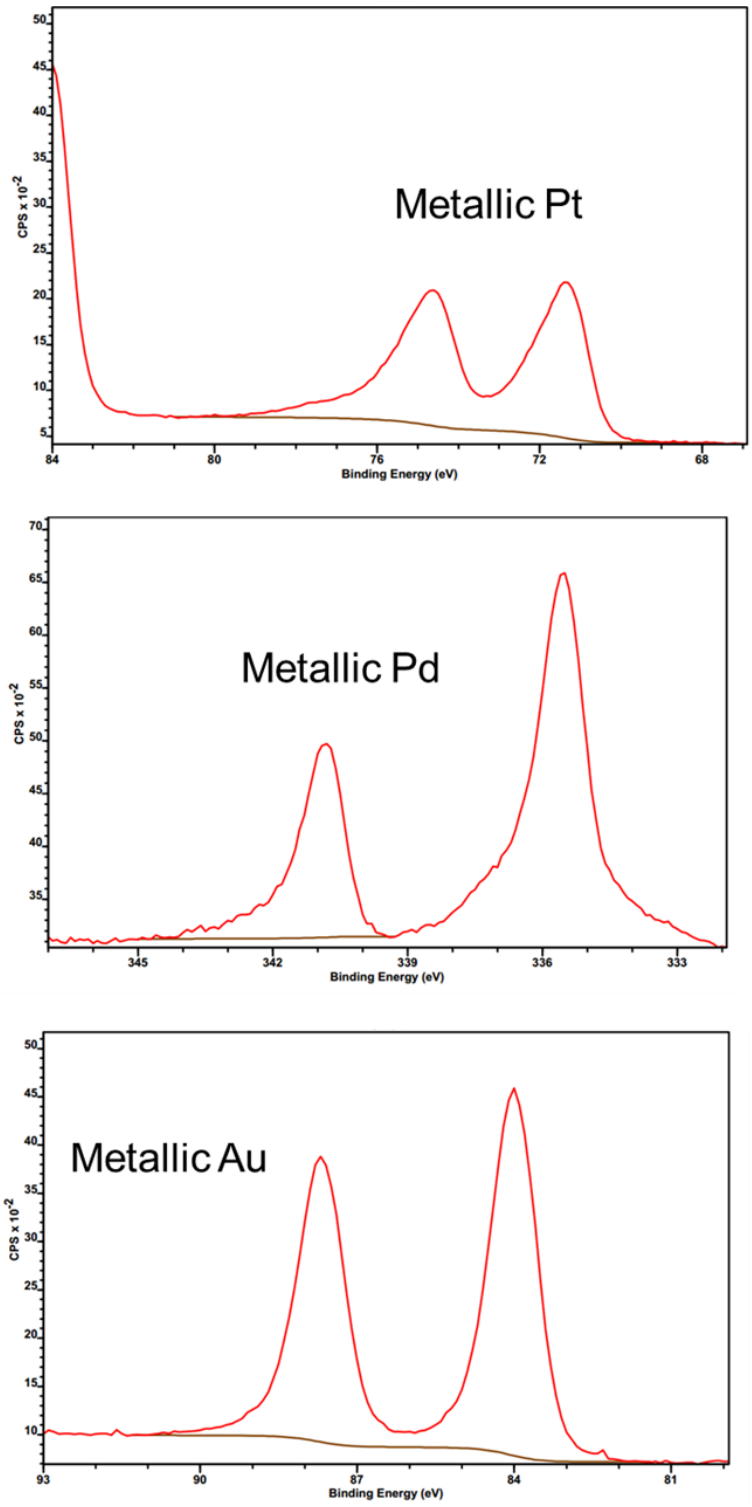

Fig. S34.

Characteristic XPS peaks for metallic Pt, Pd, and Au present in the octonary HEA-NPs (**after thermal shock**), which shows the formation of metallic bonding states.

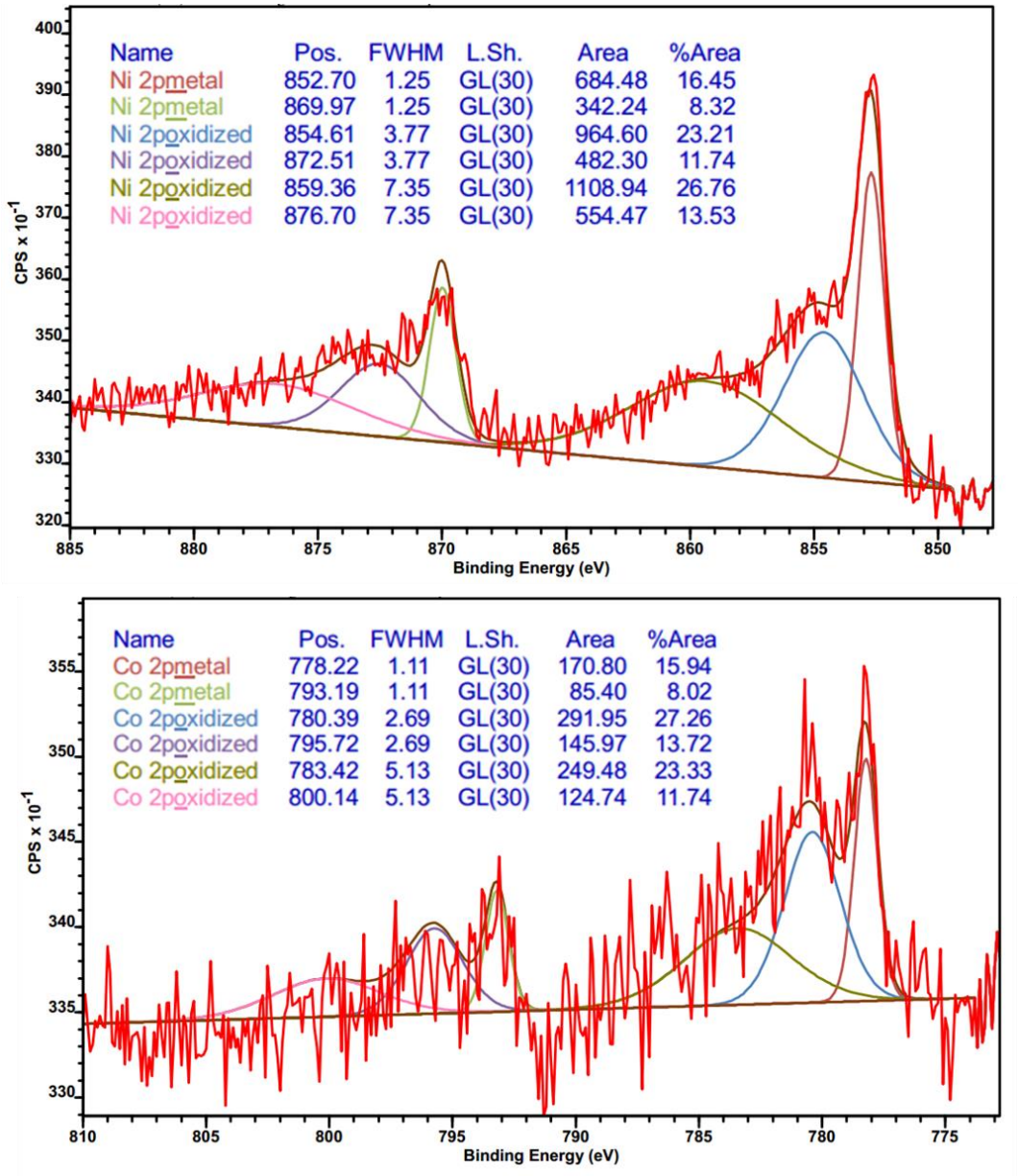

Fig. S35.

Characteristic XPS peaks for Ni and Co in the octonary HEA-NPs (**after thermal shock**), which shows the formation of mixed metallic bonding and oxidized bonding states. Although the sample was prepared in an argon filled glovebox (inert gas atmosphere), it was exposed to air after synthesis and thus, surface oxidation likely occurred for these non-noble metals.

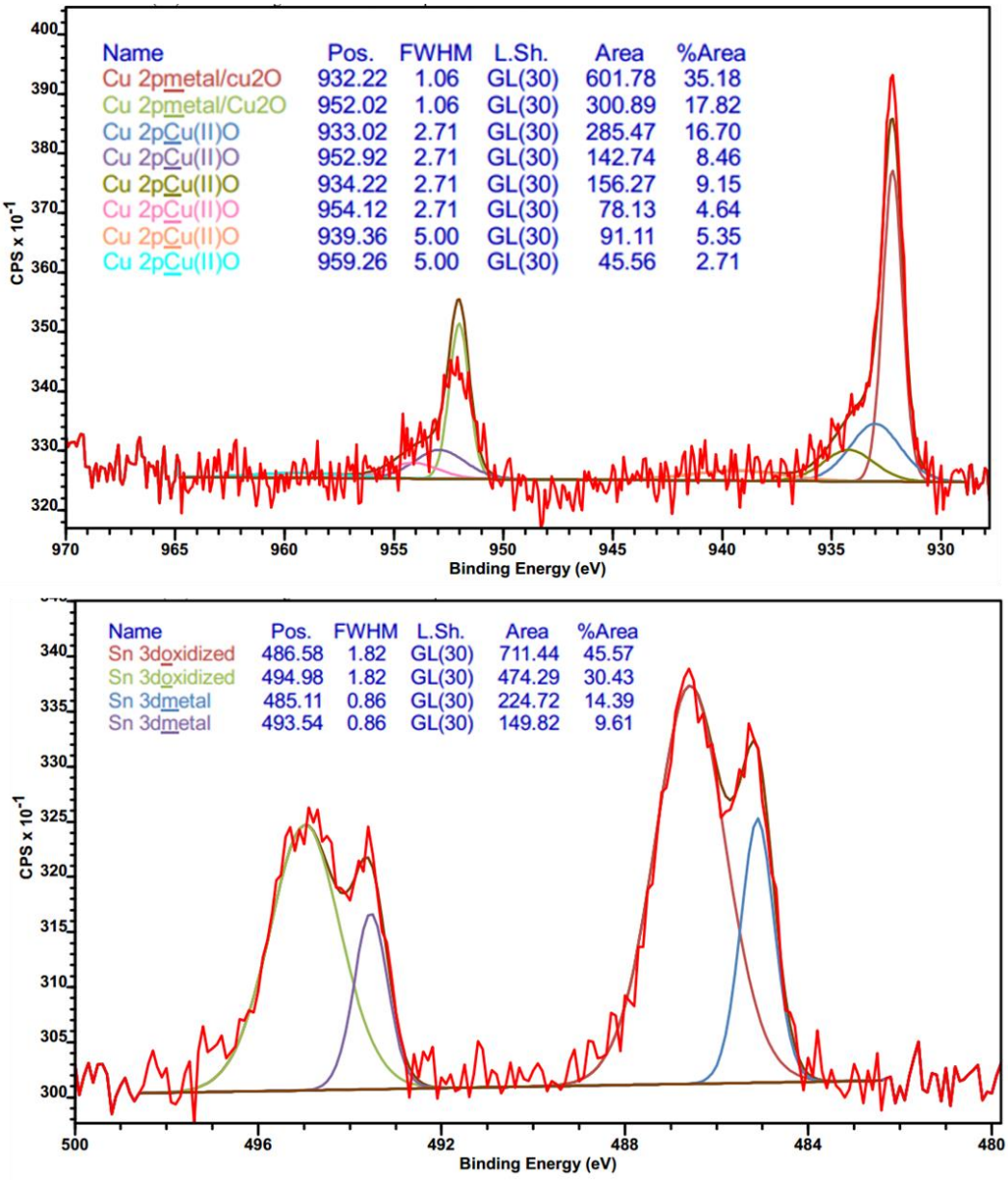

Fig. S36.

Characteristic XPS peaks for Cu and Sn in the octonary HEA-NPs (**after thermal shock**), which shows the formation of mixed metallic bonding and oxidized bonding states. The sample was exposed to air after synthesis and thus, surface oxidation likely occurred for these non-noble metals.

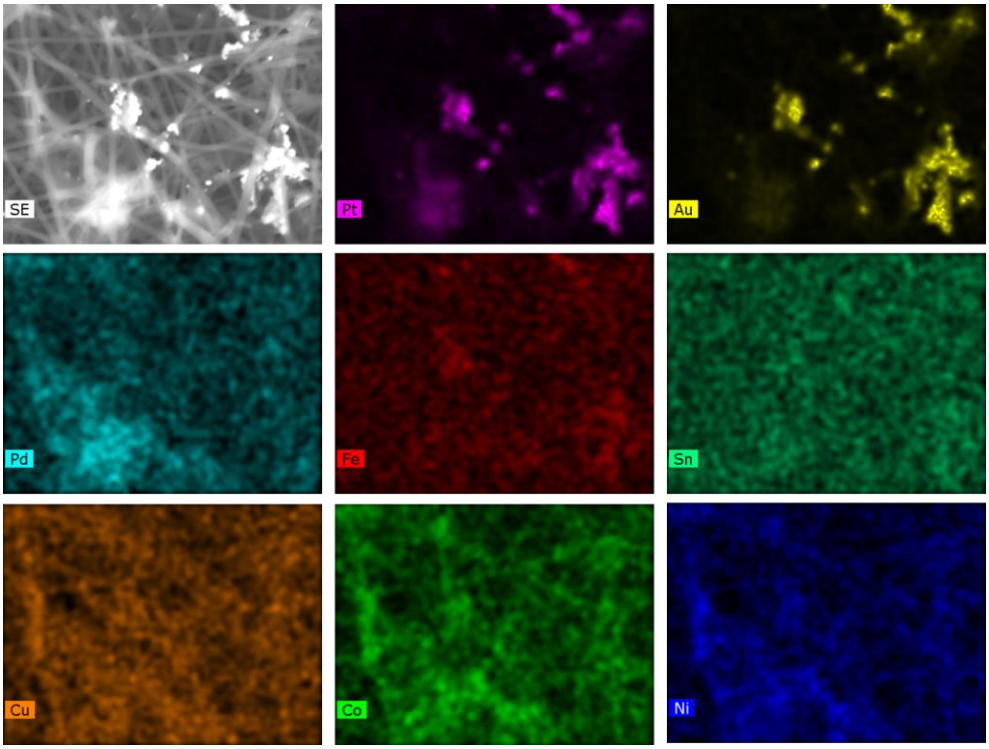

Fig. S37.
Elemental maps of the initial precursor-loaded CNF used to create an octonary nanoalloy.

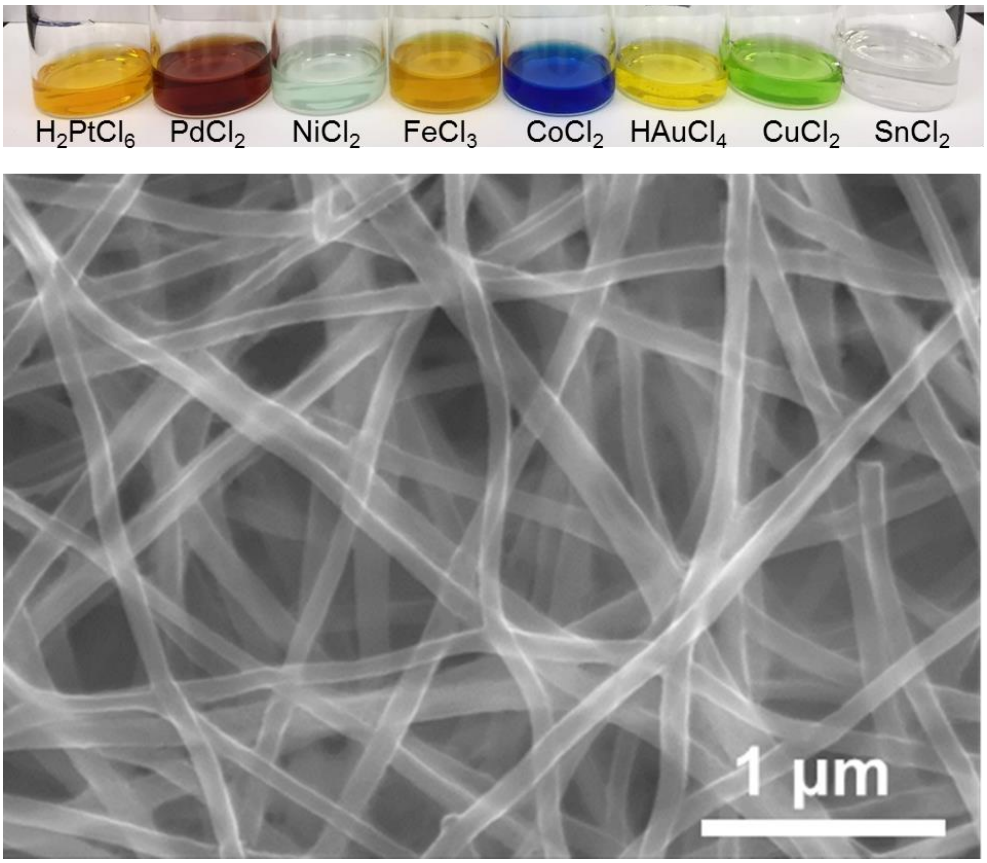

Fig. S38.

Ethanol-based 8 elemental precursor solutions used to synthesize octonary HEA-NPs on CNFs. The SEM image confirms the uniform precursor loading on CNFs, which is crucial to achieving the desired nanoparticle compositions via the CTS method.

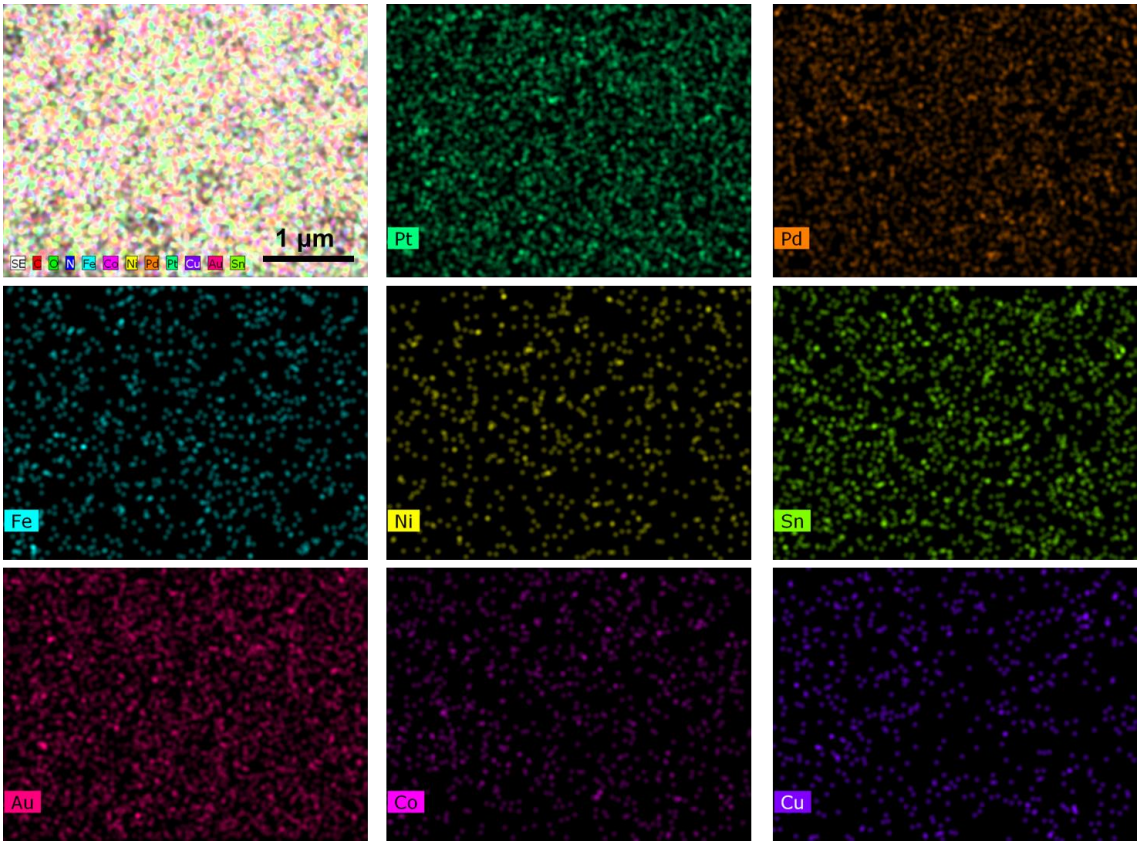

Fig. S39.
SEM-EDS maps of octonary precursors uniformly loaded onto a CNF film, which shows a uniform distribution of each salt precursor. No aggregates are apparent.

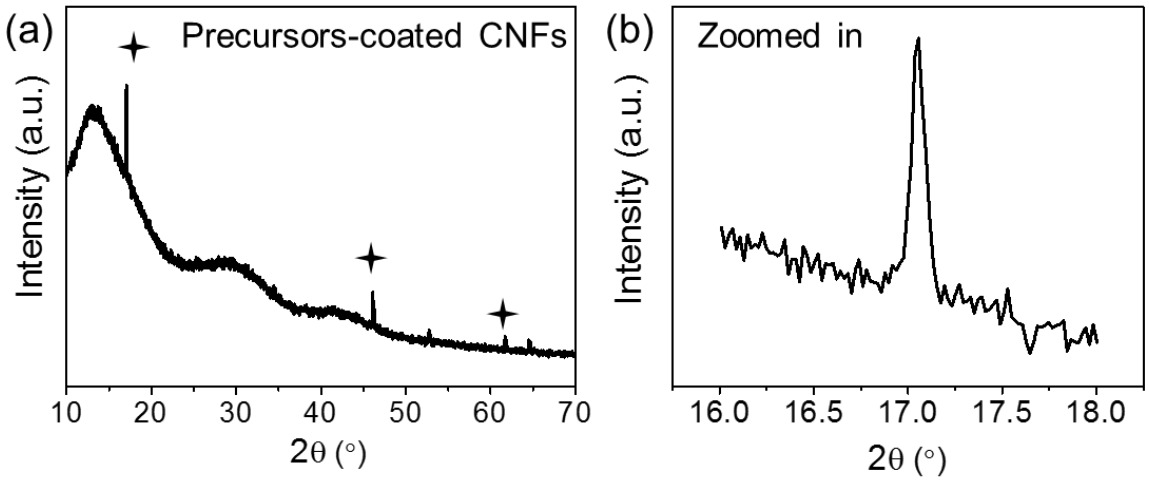

Fig. S40.

XRD profile of octonary precursors conformally coated on CNFs. (a) Overall spectra of the 8 elemental salt precursors loaded onto the CNF film and (b) a magnified view of the sharp peak at 16°-18°. The sharp peak is not split, which confirms a single-phase structure.

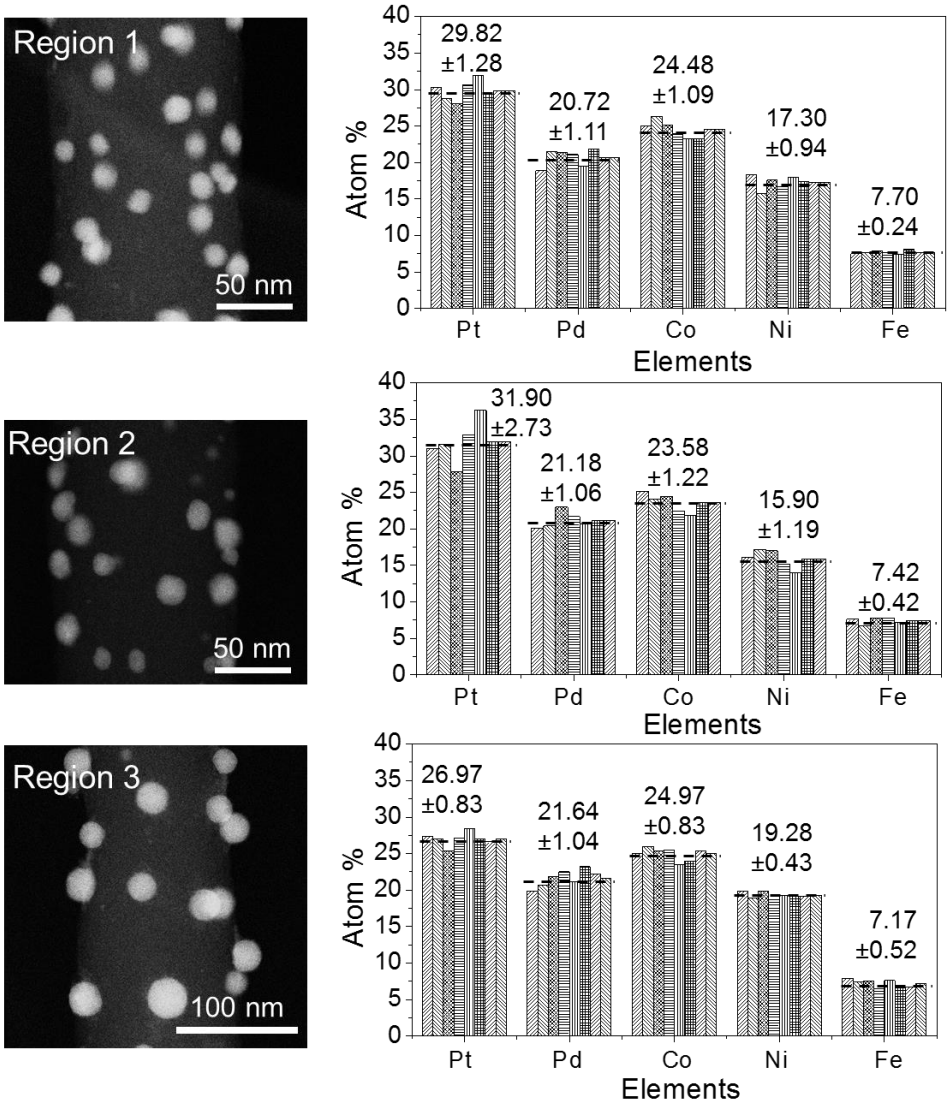

Fig. S41.

Atomic percentage distributions for quinary HEA-NPs (PtPdCoNiFe) at different sample regions. The variations for each element is roughly below 10%.

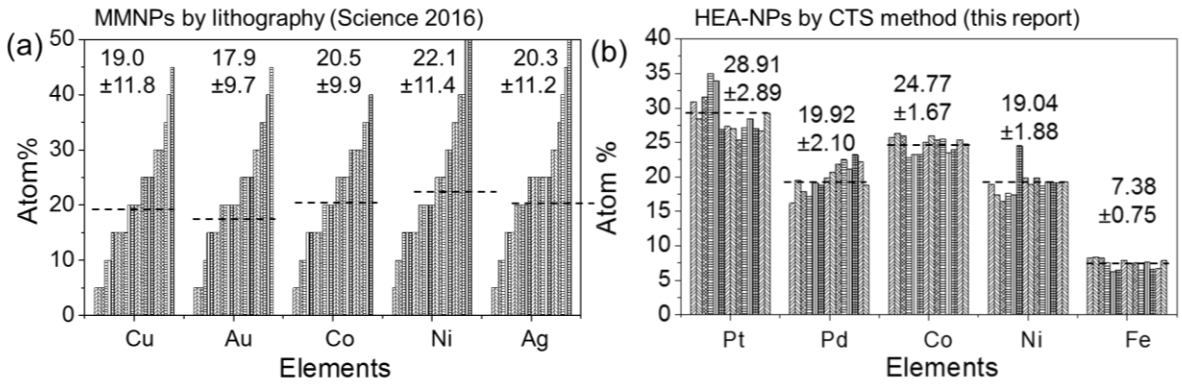

Fig. S42.

(a) Compositional comparison of quinary MMNPs synthesized by scanning probe copolymer lithography(*1*) and (b) quinary HEA-NPs synthesized by our CTS method. A more uniform elemental/compositional distribution is achieved using our CTS method.

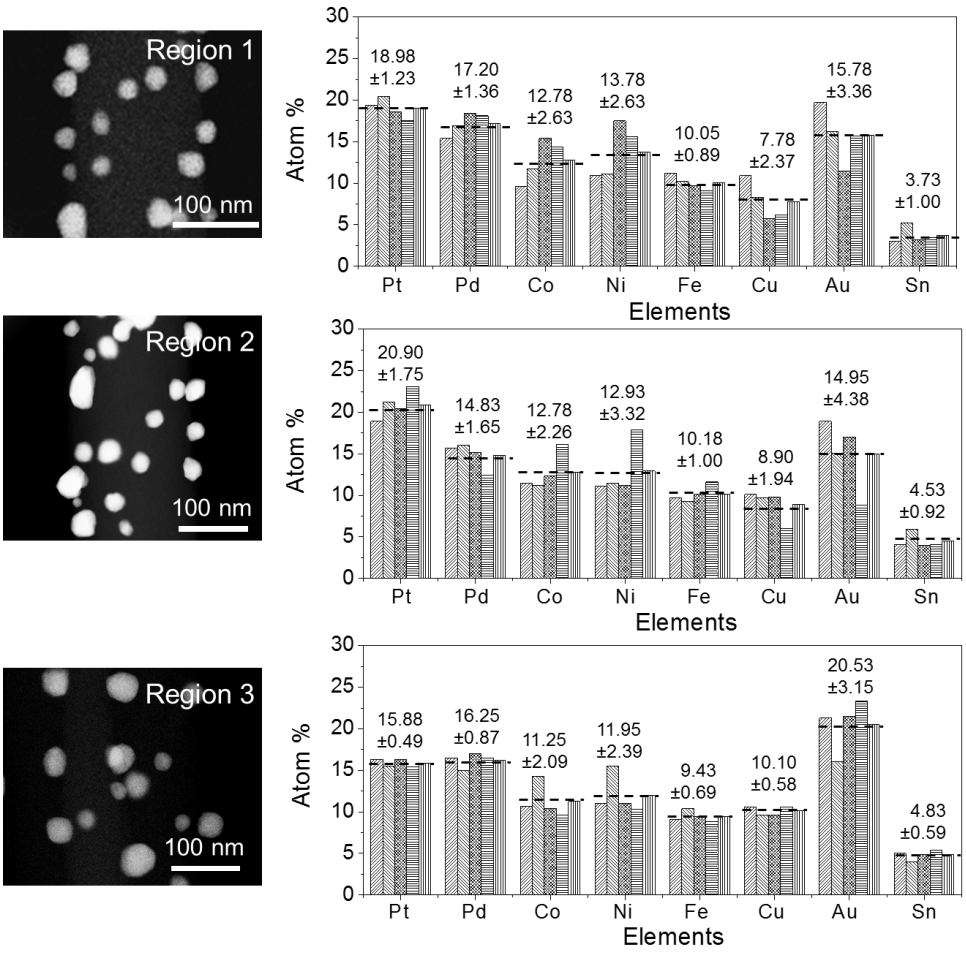

Fig. S43.

Atomic percentage distributions for quinary HEA-NPs (PtPdCoNiFe) at different sample regions, which confirms the compositional uniformity among nanoparticles synthesized by CTS.

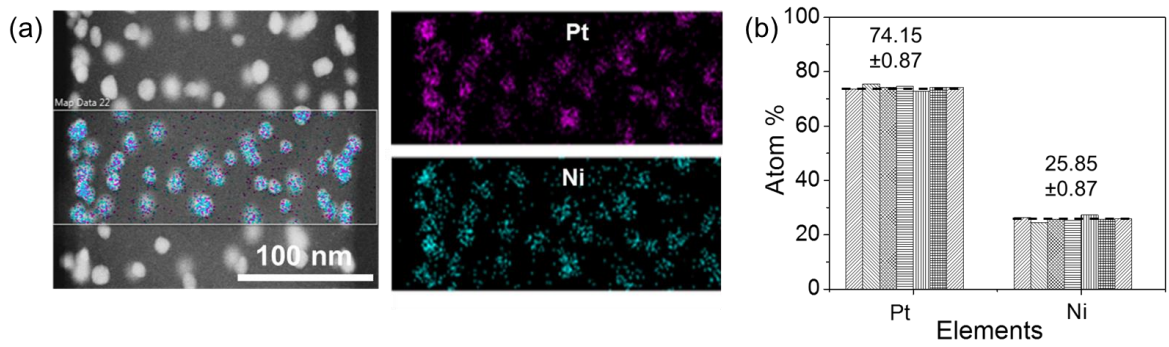

Fig. S44.

(a) Typical STEM elemental maps of PtNi nanoparticles, which illustrates the formation of alloyed structures. (b) Statistical analysis of STEM maps for PtNi at multiple sample regions with a <5% variation in composition.

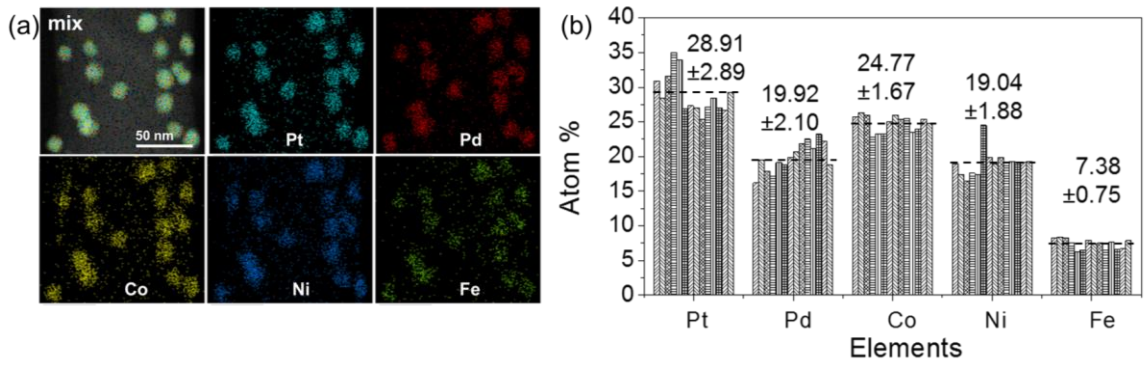

Fig. S45.

(a) Typical STEM elemental maps of solid solution alloy nanoparticles composed of five elements (PtPdCoNiFe). (b) Statistical analysis of the quinary HEA-NPs based on numerous STEM elemental maps. The variations for each element are about ~10%.

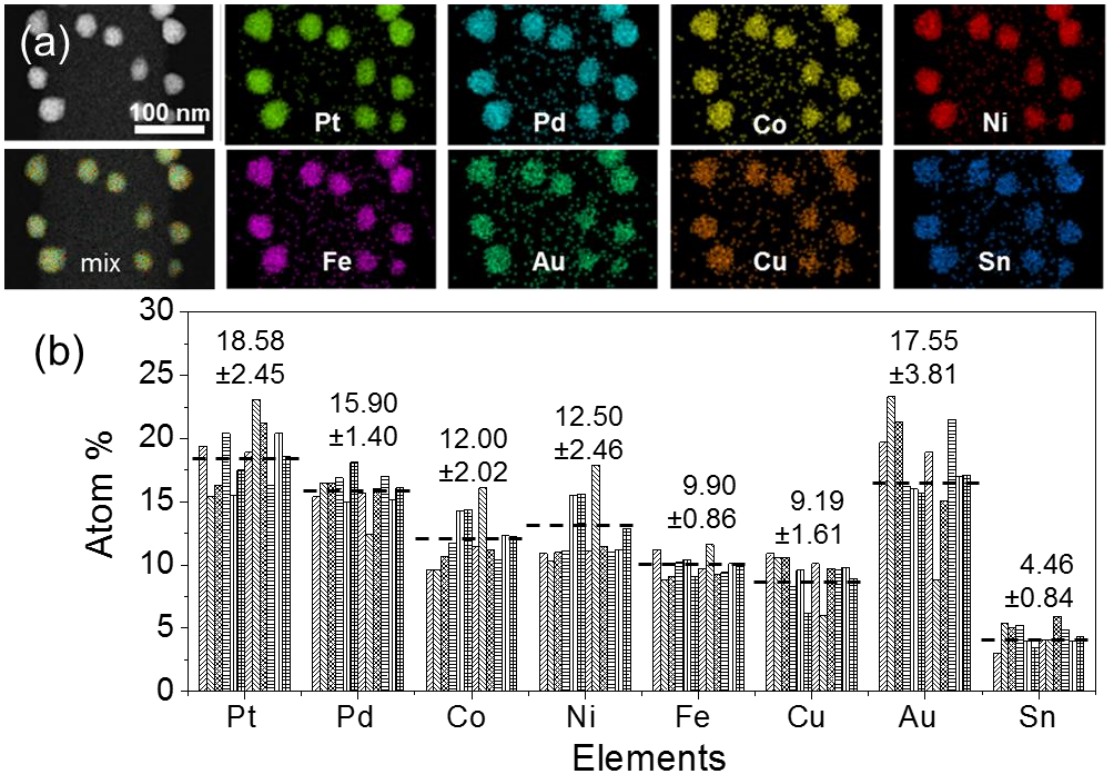

Fig. S46.

(a) Typical STEM elemental maps of octonary HEA-NPs (PtPdCoNiFeCuAuSn). Alloyed structures composed of 8 elements are readily achieved without elemental segregation or phase separation. (b) Statistical analysis using STEM maps for multiple regions of the octonary HEA-NP sample. The compositional variation remains small (~10-20%) with up to 8 dissimilar metals.

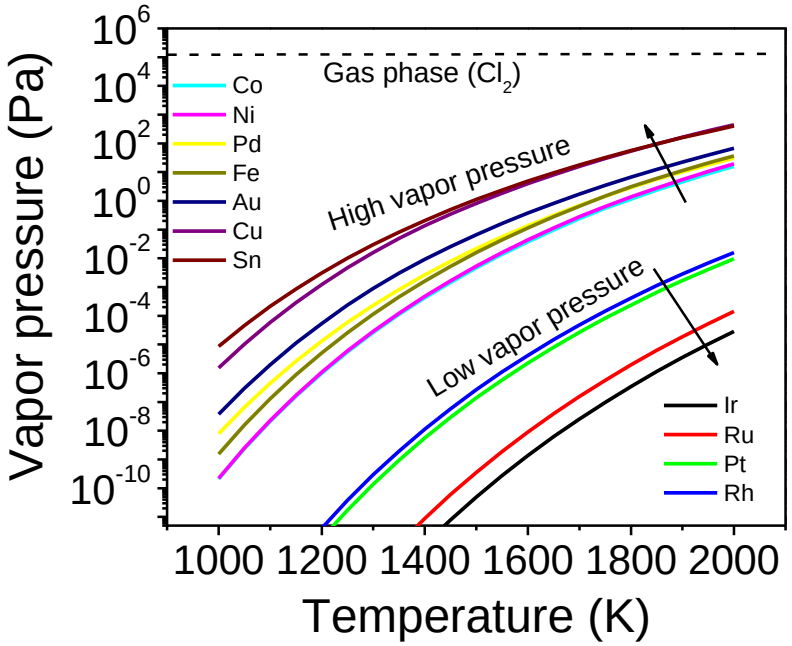

Fig. S47.

Theoretical metal vapor pressures as a function of temperature on a logarithmic scale for each metal in the bulk and single element states. [Calculated using an online tool: https://www.iap.tuwien.ac.at/www/surface/vapor_pressure]

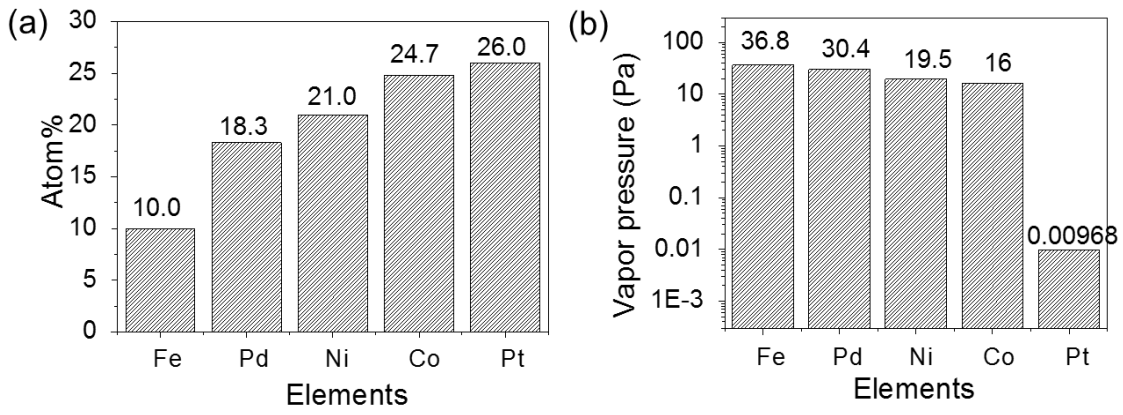

Fig. S48.

(a) ICP-MS results of quinary HEA-NPs (PtPdCoNiFe) and (b) theoretical vapor pressures for each element (PtPdCoNiFe) at 2000 K. The final composition for PtPdCoNiFe roughly follows their evaporation sequence.

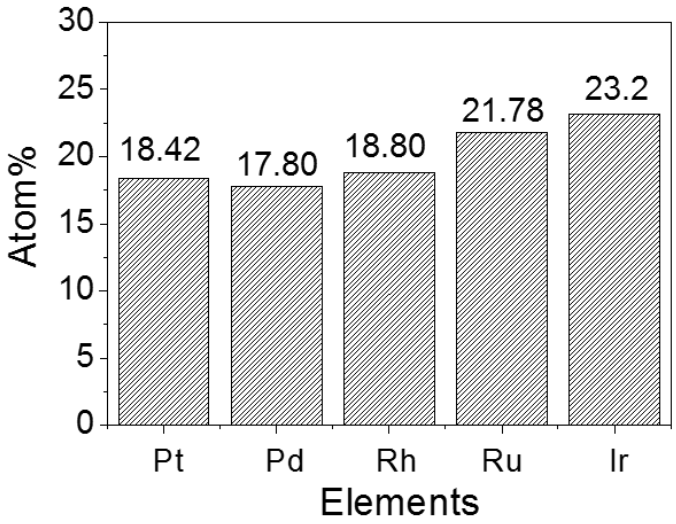

Fig. S49.

Compositional distribution of noble metal quinary HEA-NPs (PtPdRhRuIr) with an elemental ratio of nearly 1:1 ratio after the CTS method.

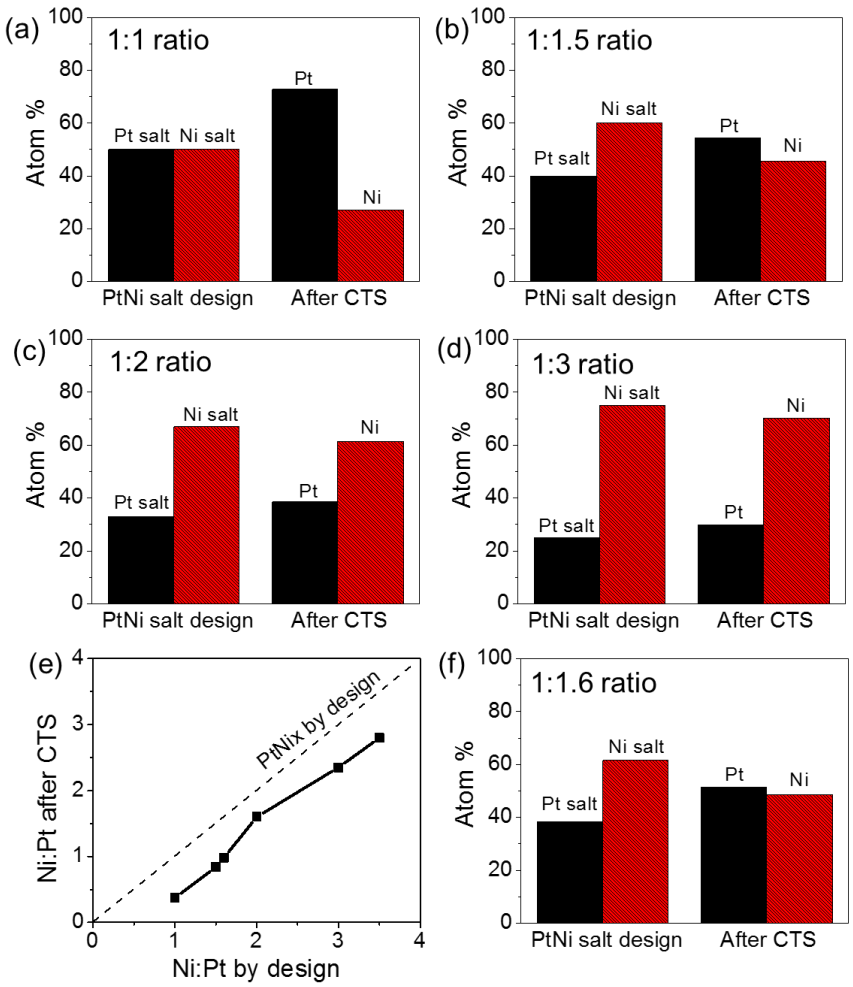

Fig. S50.

Compensating for Ni loss by adjusting the precursor salt ratio of the model PtNi system (i.e. adding more Ni to the initial precursor solution). (a)-(d) $PtNi_x$ synthesized with Pt:Ni ratios from 1:1 to 1:1.5, 1:2, and 1:3, respectively. (e) ICP-MS compositional ratio of PtNi vs. the initial ratio of the salt precursors. The linear trend can be used to precisely control the final product composition. (f) A nearly 1:1 ratio of PtNi was achieved by using an initial Pt:Ni ratio of 1:1.6.

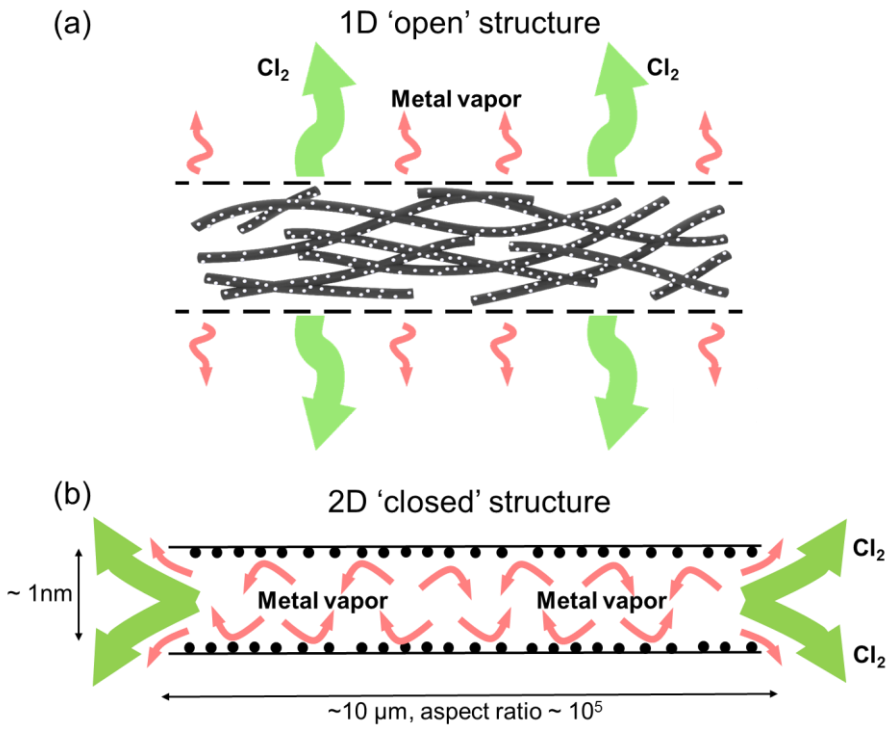

Fig. S51.

Metal evaporation comparison between a 1D 'open' structure (CNFs) and a 2D 'closed' structure (RGO). The 2D closed structure can minimize the metal evaporation that occurs at high temperature due to the impermeability of graphene sheets.

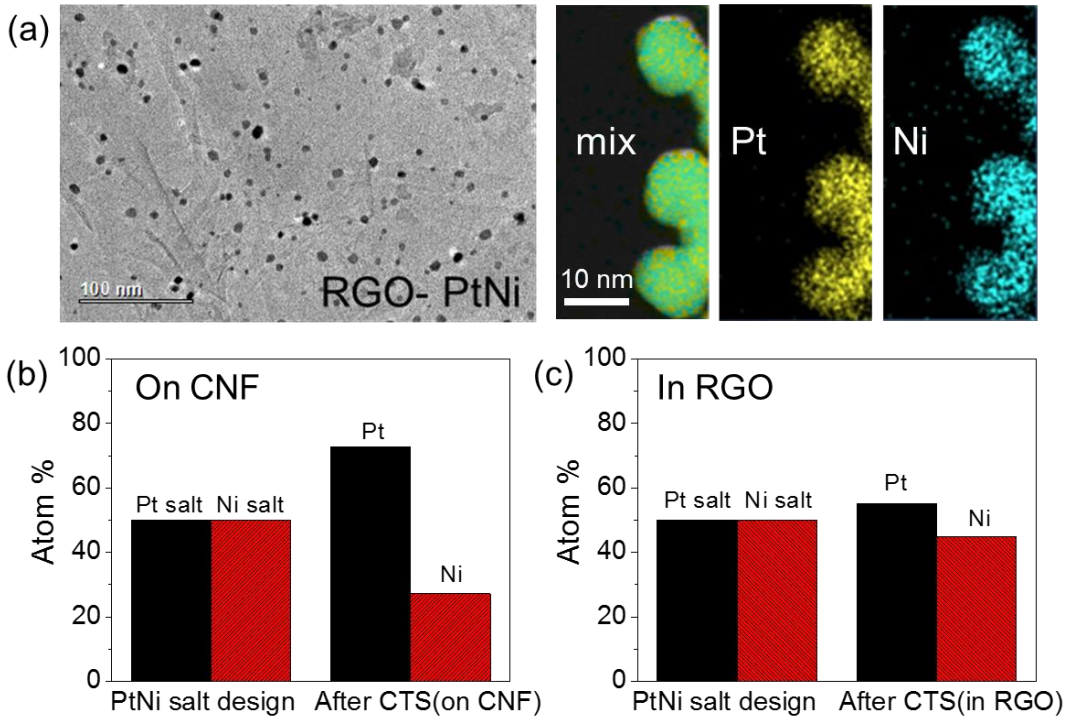

Fig. S52.

Indirect compositional control of PtNi nanoparticles synthesized on a "closed" RGO substrate. (a) STEM image and corresponding elemental maps for PtNi synthesized within a RGO film. ICP-MS results for PtNi synthesized on a (b) CNF film with an open structure and in a (c) RGO film with a 'closed' structure. The 2D RGO sheets minimize the amount of metal evaporation at high temperature due to its high aspect ratio.

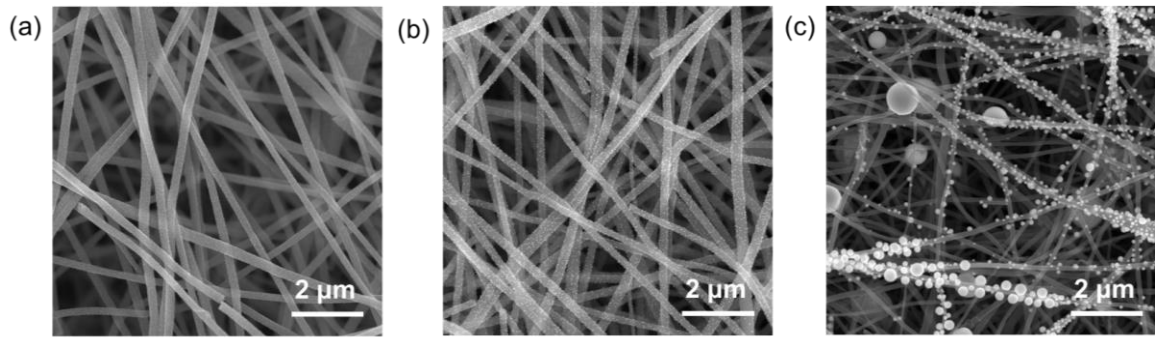

Fig. S53.

Synthesized nanoparticles on CNFs with different defect concentrations (control experiments). (a-c) SEM images of AuNi nanoparticles on CNF films carbonized at 873 K, 1073 K, and 1273 K, respectively.

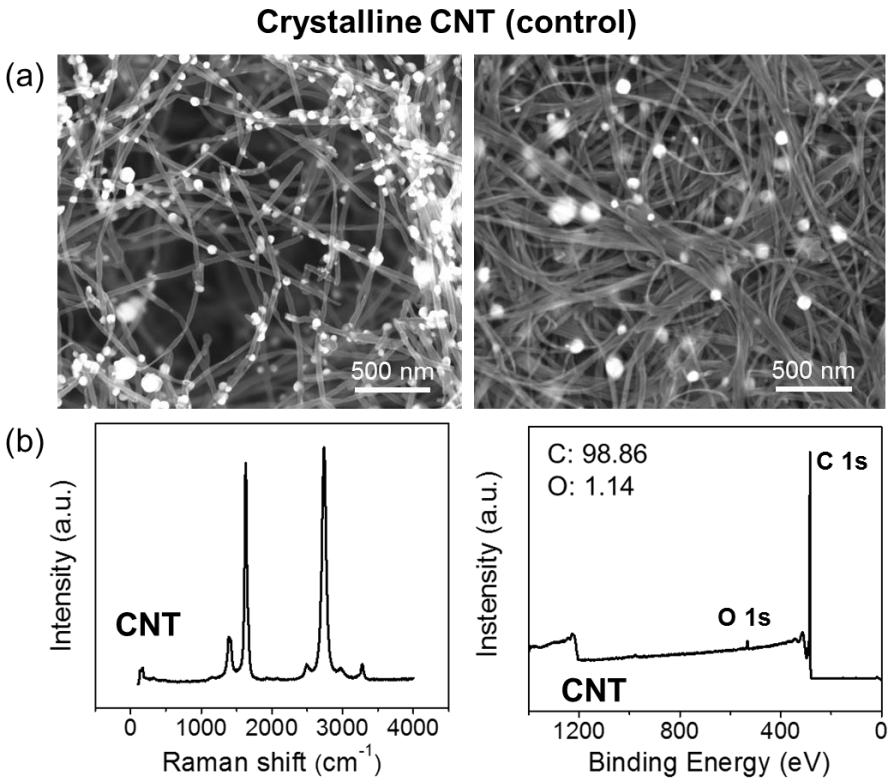

Fig. S54.

Role of defects in nanoparticle dispersion on CNTs as a control experiment. (a) AuNi NPs on crystalline CNTs, showing only aggregates due to the lack of defects. (b) Defect characterization for CNTs by Raman and XPS spectra. Note that crystalline CNTs barely disperse metals via the CTS method.

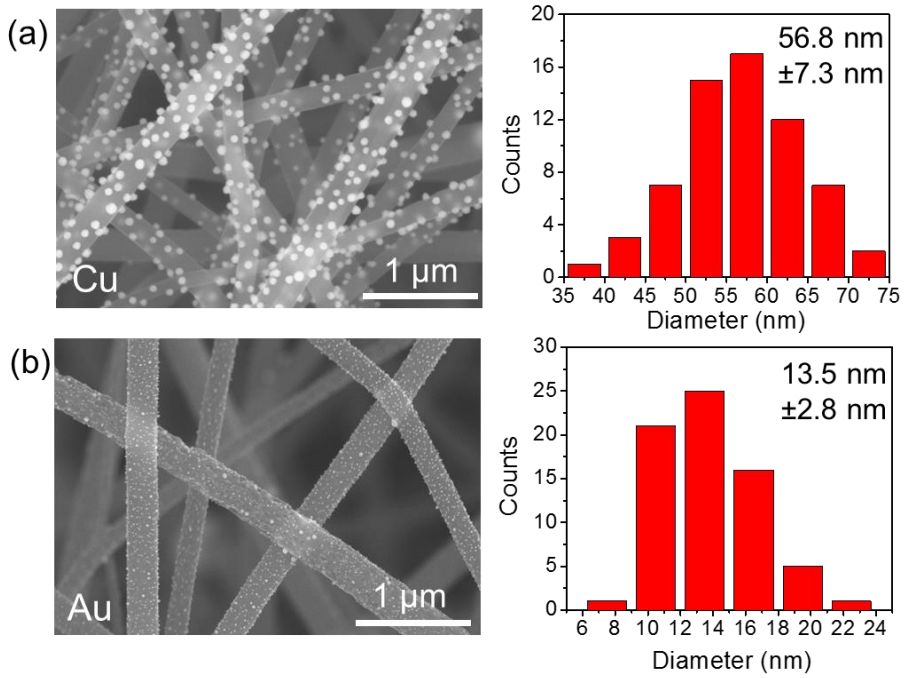

Fig. S55.

SEM images of the metallic nanoparticle dispersions on CNFs using the same CTS synthesis conditions: (a) Cu and (b) Au. Although Au and Cu have similar physical properties, the particle size distributions achieved through the same CTS process are vastly different, which indicates a particle dispersion mechanism related to the individual metal species (i.e. catalytic activity).

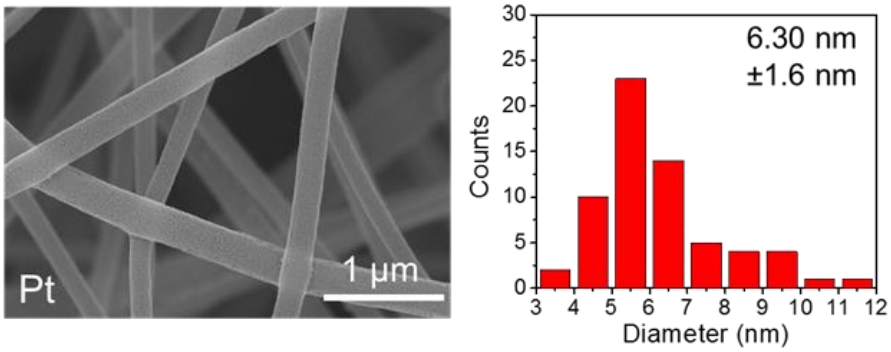

Fig. S56.

SEM images of Pt nanoparticles dispersed on CNFs. A much smaller size distribution compared to Au and Cu is evident, which confirms that metal species with higher catalytic activity aid in the generation and dispersion of smaller and more uniform nanoparticles.

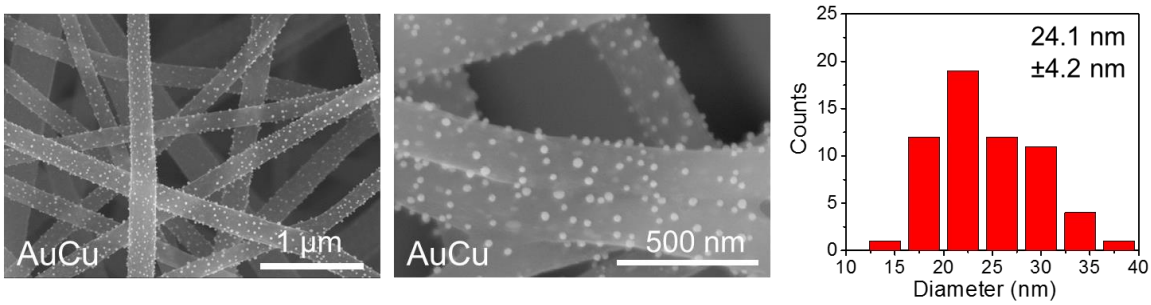

Fig. S57.

SEM images of AuCu nanoalloys and their dispersion on CNFs. The combination of AuCu yields a particle size distribution in between pure Au and Cu yet the higher catalytic element (Au) improves the dispersion of the binary alloy nanoparticles to levels beyond pure Cu.

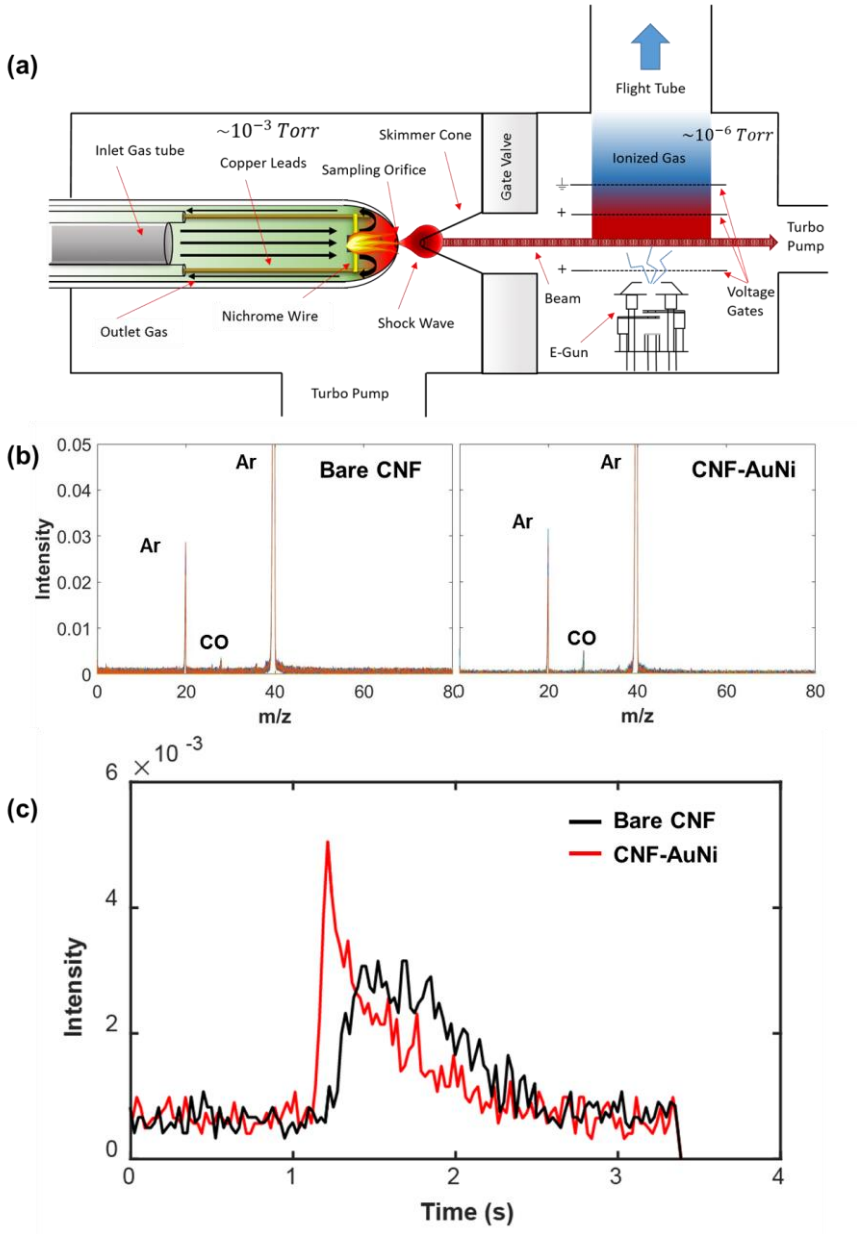

Fig. S58.

(a) Experimental setup and Molecular Beam Mass Spectrometer schematic for flame sampling during combustion. (b) The full mass spectrum obtained during a 55 ms high temperature CTS for bare CNF and CNF-AuNi. (c) Temporal CO emission profiles for bare CNF and CNF-AuNi. The CNF-AuNi sample shows a sharp peak in terms of CO release compared to bare CNF, which demonstrates a catalytic carbon metabolism (C+O*=CO↑) reaction occurs during the CTS process.

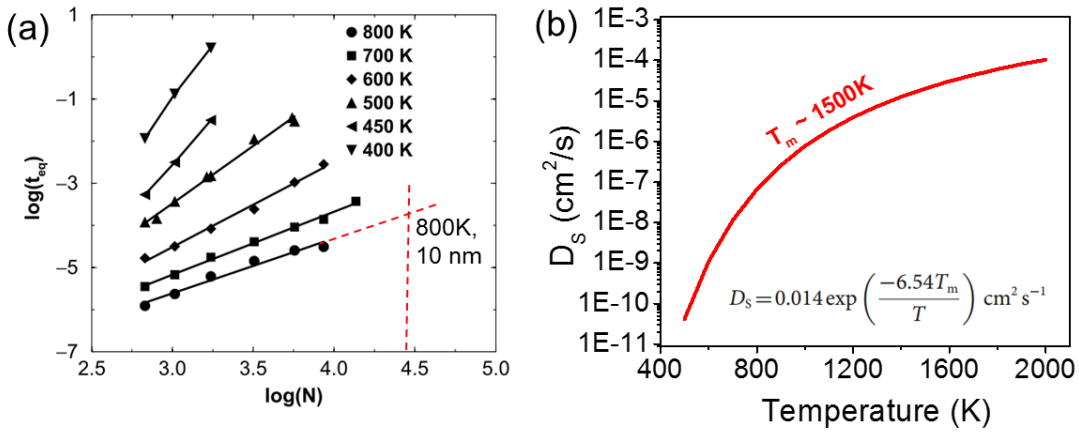

Fig. S59.

(a) Log-log plot showing relaxation time (teq) as a function of the crystallite size (N is the number of atoms) at different temperatures *(28).* (b) Estimation of temperature-dependent surface diffusivity for metals with a melting temperature of ~1500 K. The inset equation is used for estimation, where Ds is the diffusivity, Tm is the melting point, and T is temperature *(30).*

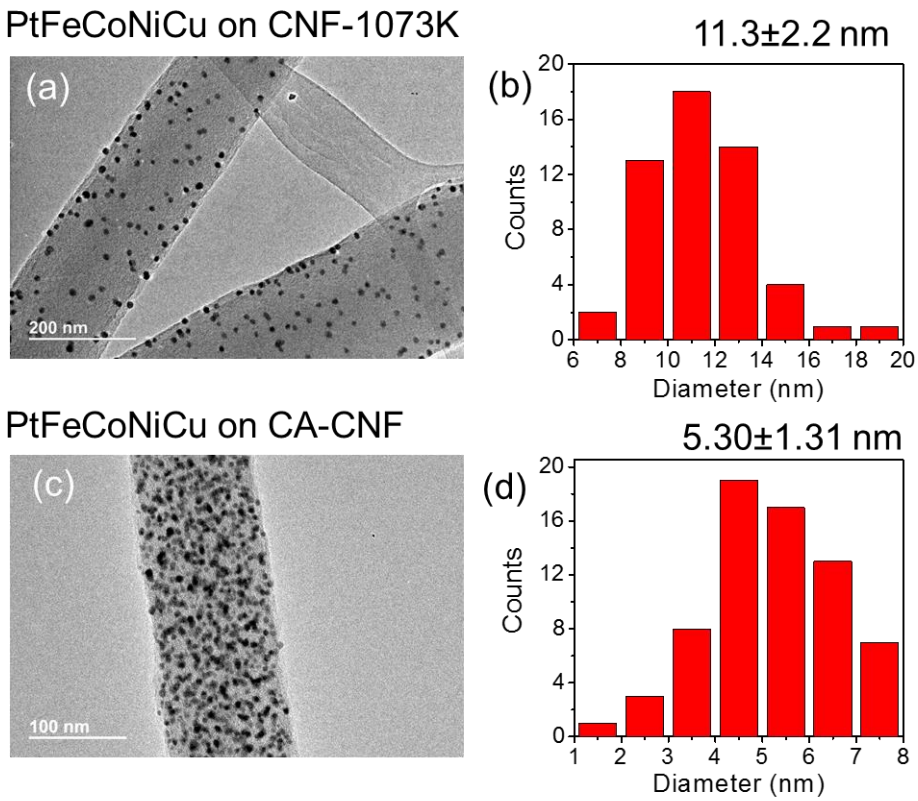

Fig. S60.

(a)-(b) TEM and size distribution of PtFeCoNiCu on CNFs. (c)-(d) TEM and size distribution of PtFeCoNiCu on CO_2-activated CNFs (CA-CNFs).

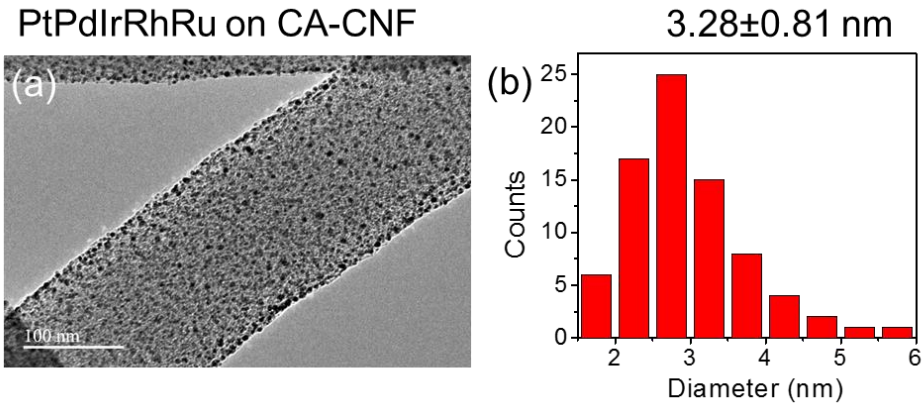

Fig. S61.

(a)-(b) TEM image and size distribution of ultrafine, well-dispersed quinary HEA-NPs (PtPdIrRhRu) on CA-CNFs, which shows a narrow size distribution (3.28 nm ± 0.81 nm).

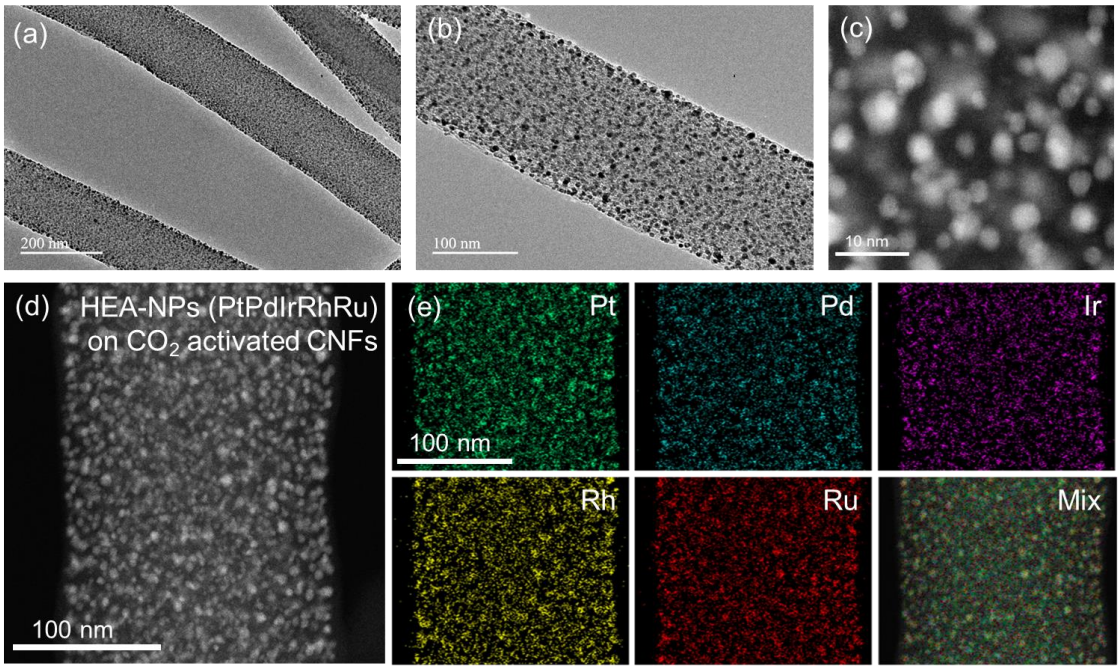

Fig. S62.

(a)-(c) TEM and HAADF images of quinary HEA-NPs (PtPdIrRhRu) on CA-CNFs, which exhibit favorable particle dispersity/uniformity at low magnifications. (d)-(e) STEM elemental maps of the same quinary nanoparticle composition on CA-CNFs, showing a uniform distribution of each element and thus, the formation of high entropy alloy structures.

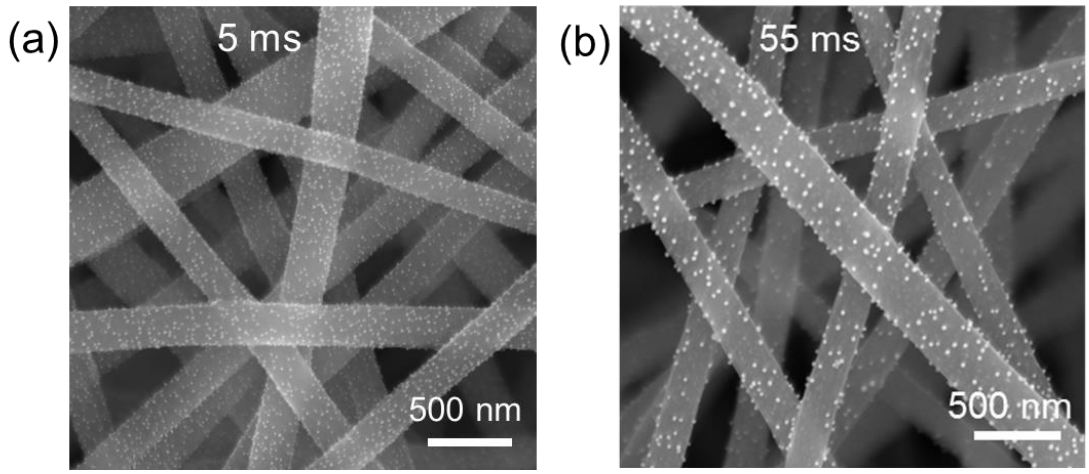

Fig. S63.

Shock time-dependent size distributions of synthesized nanoparticles by CTS. AuNi nanoparticles formed by a (a) 5 ms and (b) 55 ms CTS process, respectively.

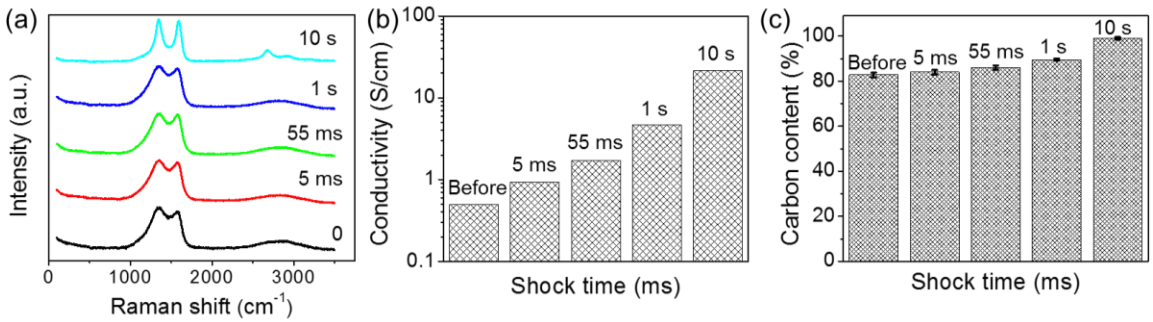

Fig. S64.

Defect concentrations of CNFs after various shock durations. (a-c) Raman spectra, conductivity measurements and changes in carbon content for CNF-PtNi films after 5 ms, 55 ms, 1 s, and 10 s CTS processes.

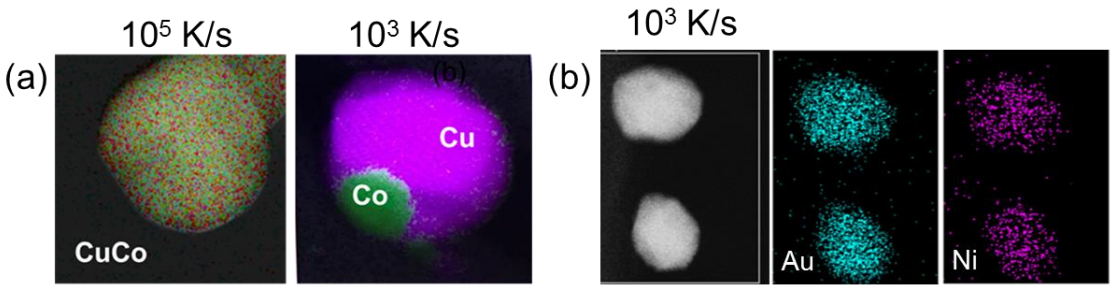

(c)

	10^5 K/s	10^3 K/s	10 K/s
AuNi	Solid solution	Solid solution	Separation
CuCo	Solid solution	Separation	

Fig. S65.

Rate-dependent non-equilibrium structures for both Cu-Co and Au-Ni systems. (a) CuCo nanoparticles show phase mixing with a ~10^5 K/s cooling rate yet, phase separation occurs when cooled at a rate of ~10^3 K/s. (b) The synthesized AuNi nanoparticles are solid solutions with ~10^5 K/s and ~10^3 K/s cooling rates. Phase separation occurs at a very slow cooling rate of 10 K/s. (c) A table that summarizes the rate-dependent non-equilibrium structures for CuCo and AuNi nanoparticle systems.

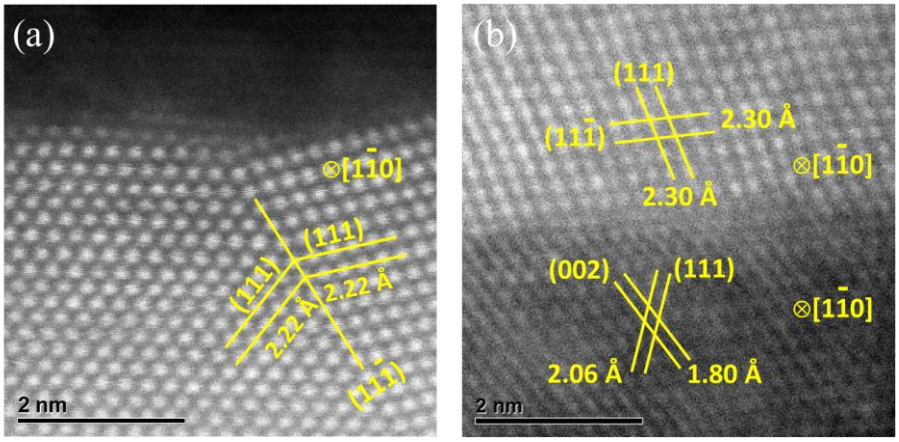

Fig. S66.

Atomic HAADF images of AuNi synthesized with different cooling rates: (a) 10^5 K/s and (b) 10 K/s.

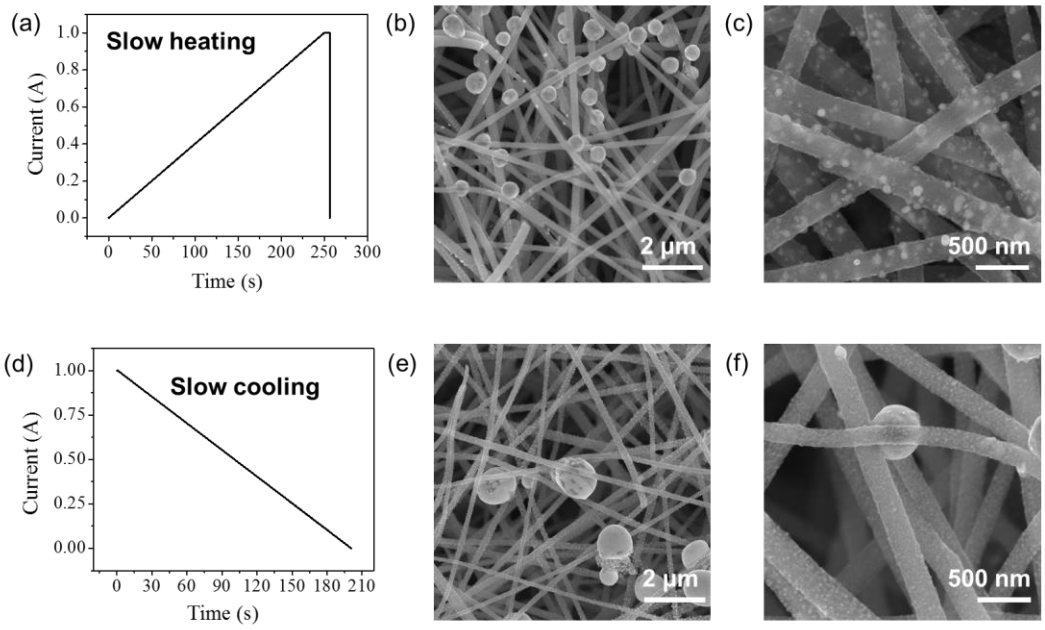

Fig. S67.

Synthesized nanoparticles by slow heating and cooling rates (control experiments). (a-c) Slow heating profile (10 K/s) and SEM images of the CNF-AuNi system via a slow heating rate. (d-f) Slow cooling profile (10 K/s) and SEM images of the CNF-AuNi using a slow cooling rate.

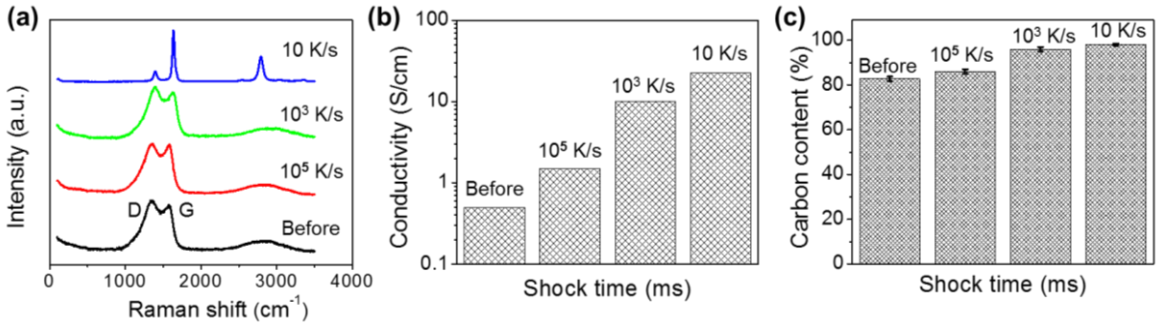

Fig. S68.

The properties of CNF films exposed to different cooling rates. (a) Raman spectra, (b) conductivity measurements, and (c) the change in carbon content for CNF-AuNi at 10^5 K/s, 10^3 K/s, and 10 K/s cooling rates.

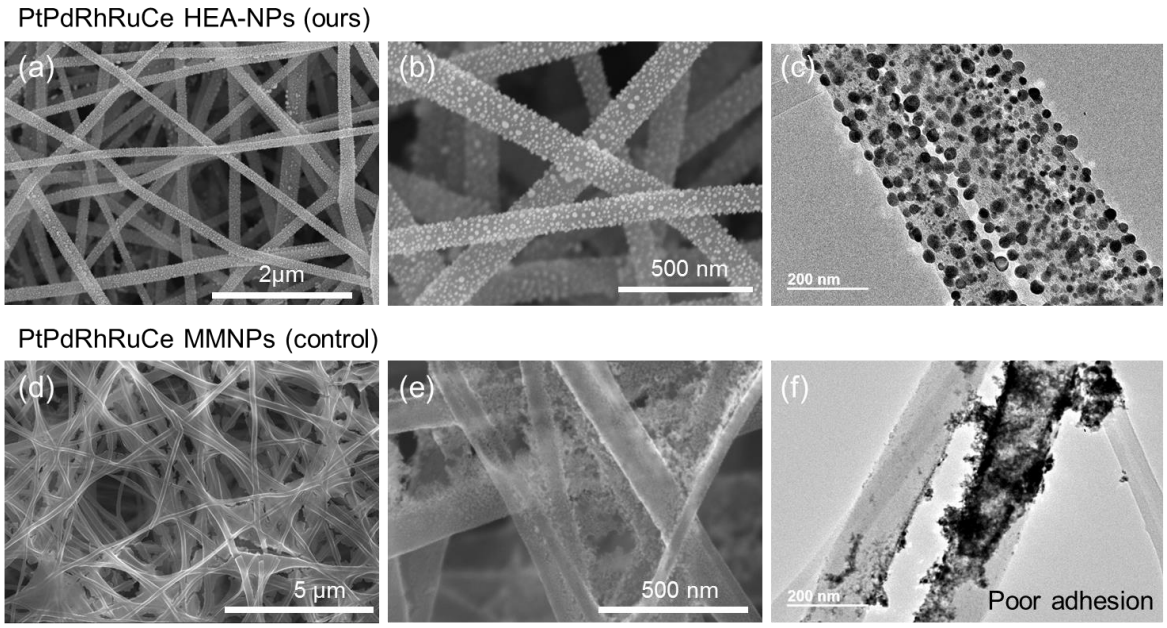

Fig. S69.

SEM and TEM images of quinary PtPdRhRuCe catalyst samples prepared via two different synthesis methods: (a)-(b) SEM and (c) TEM images of HEA-NPs by our CTS method; (d)-(e) SEM and (f) TEM images of MMNPs by the wet impregnation method. Our HEA-NPs show excellent particle formation, dispersion, and adhesion on the CNF support. However, the control sample merely reduced the precursor in situ without exhibiting particle dispersive capabilities. Note that only a small amount of particles are present on CNFs after sonication (for TEM preparation) due to poor adhesion.

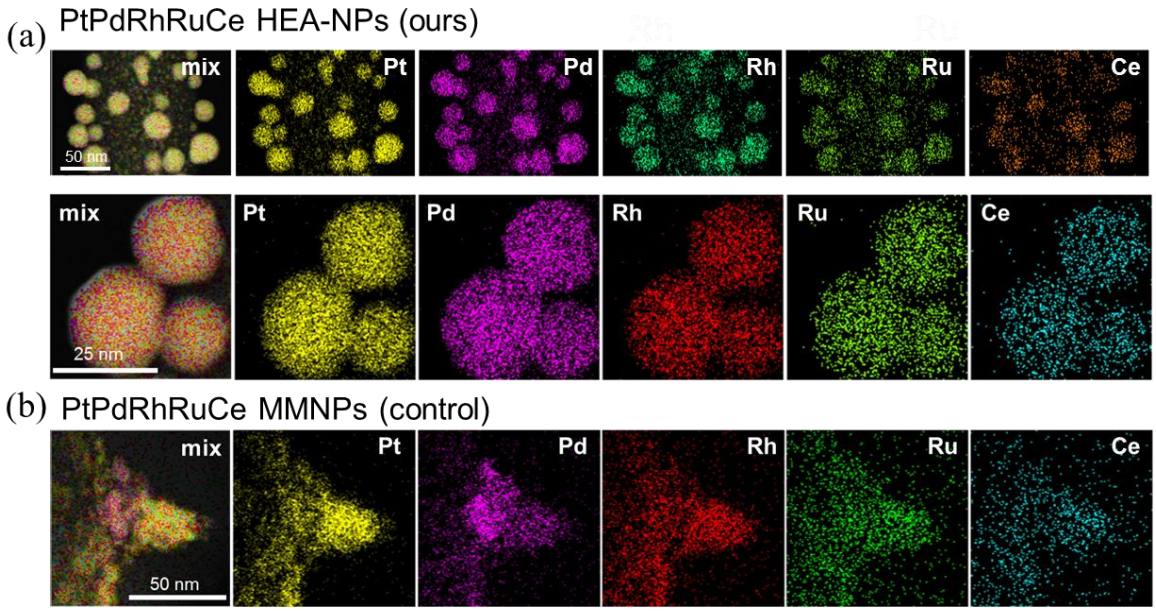

Fig. S70.

STEM elemental maps for (a) PtPdRhRuCe HEA-NPs and (b) PtPdRhRuCe MMNPs (control). Our HEA-NPs retain the homogeneously mixed liquid metal state due to rapid quenching, which results in a uniform elemental distribution within the nanoparticles. However, the control sample exhibits phase/elemental separation/segregation especially between Pt and Pd due to the slow, low-temperature reduction procedure.

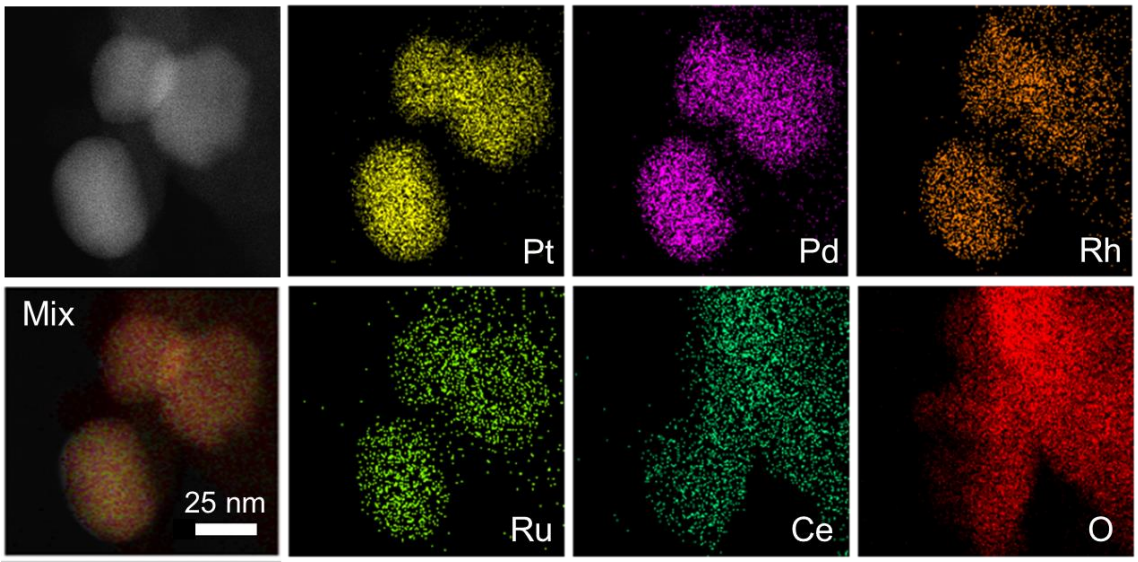

Fig. S71.

STEM elemental maps of quinary PtPdRhRuCe HEA-NPs after undergoing catalytic reaction. The nanoparticles retain their original high entropy solid solution structure, which demonstrates the structural stability of HEA-NPs at high temperature to resist thermo-driven phase separation. Note that after the high temperature catalytic reaction, Ce becomes oxidized, which is expected due to the element's poor oxidation resistance.

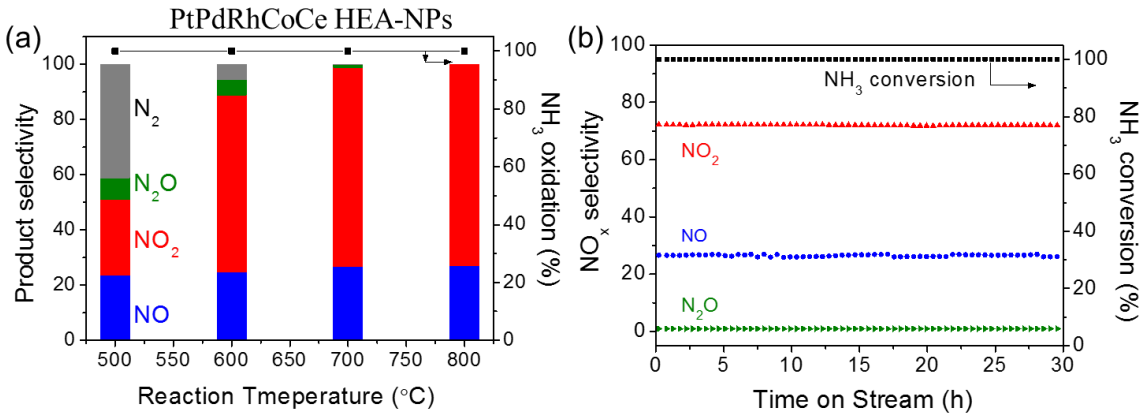

Fig. S72.

Catalytic application of relatively inexpensive quinary HEA-NPs for ammonia oxidation: (a) Temperature-dependent product distribution (left) and conversion (right) of NH_3 oxidation for the PtPdRhCoCe HEA-NP sample; (b) time-dependent catalytic performance of PtPdRhCoCe HEA-NPs at 700°C.

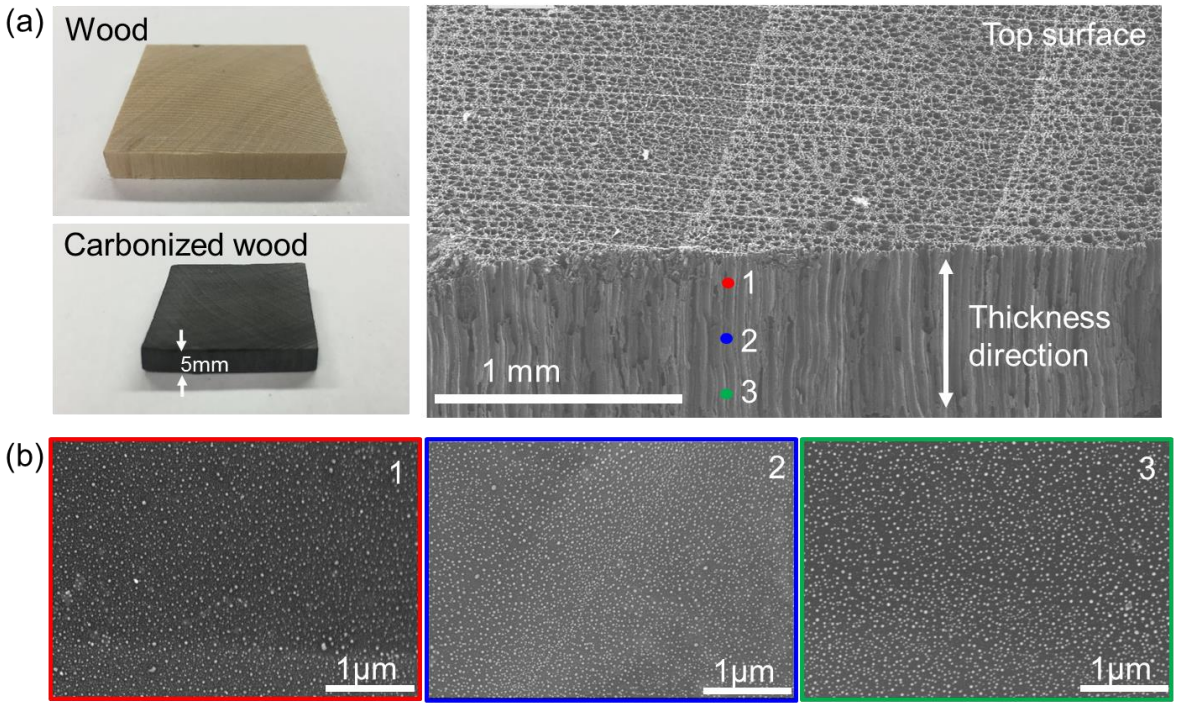

Fig. S73.

Carbonized wood as a 3D substrate to increase the NP production of our CTS method. (a) Digital images of both wood and carbonized wood, and an SEM image of the carbonized wood. Wood has a unique microstructure: open microsized pores on the top surface and vertically-aligned microsized channels in the thickness direction. (b) SEM images of uniformly distributed quinary HEA-NPs (PtPdRhRuCe) in three different locations of the 3D substrate as noted in (a).

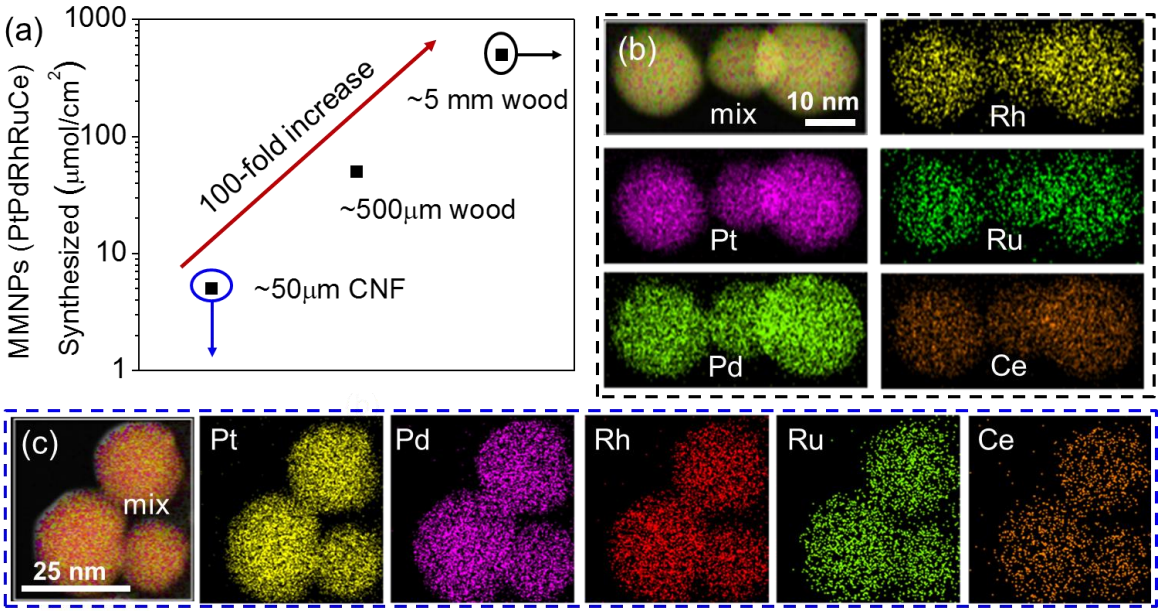

Fig. S74.

Increased particle loading on carbonized wood samples. (a) The areal loading increased from 5 μmol/cm^2 for the CNF film to 60-600 μmol/cm^2 for the carbonized wood substrate. This corresponds to a ~10X (~10 mg/cm^2) and ~100X (~100 mg/cm^2) increase in particle production compared to the CNF films. STEM elemental maps for quinary HEA-NPs (PtPdRhRuCe) prepared on (b) carbonized wood and (c) CNFs, respectively. Each HEA-NP is a high entropy, uniformly mixed structure, which indicates the nanoparticle quality is not compromised during scale up.

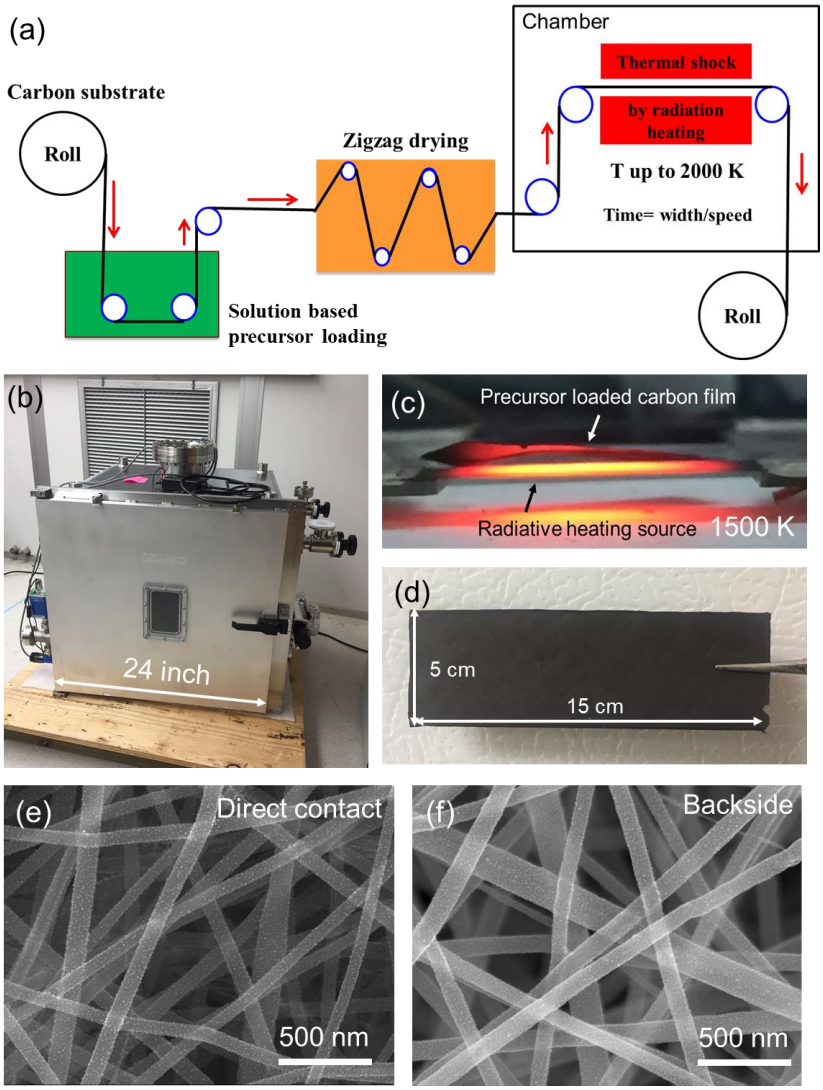

Fig. S75.

(a) Continuous roll-to-roll manufacturing schematic of a carbon-metallic NP composite by rapid radiative heating. (b) A custom-built chamber to simulate a small-scale roll-to-roll process located within Dr. Hu's lab at the University of Maryland, College Park. (c) To mimic the roll-to-roll process by radiation-based heating, the precursor-loaded carbon substrate was placed above the radiative heating source for ~1s at ~1500K. (d) The NP-loaded carbon film synthesized by radiation-based heating (i.e. scalable CTS). SEM image of Pt NPs synthesized by radiative heating on a ~30 μm thick CNF film: (e) direct contact side and (f) backside.

Table S1.

Physi-chemical properties of the elemental precursor salts used and corresponding metals.

Precursors	Chemical reduction potential [V]	Physical decom-position T [K]	Metals	Atomic Radius [Å]	Melting point [K]	Boiling point [K]	Room-T structure
H_2PtCl_6	0.68, 0.73, 1.18	573, 653, 853	Pt	1.39	2041	4098	FCC
$PdCl_2$	0.95	952	Pd	1.37	1828	3236	FCC
$NiCl_2$	-0.25	>1073	Ni	1.24	1728	3186	FCC
$FeCl_3$	0.77, -0.44	553, 588	Fe	1.26	1811	3134	BCC
$CoCl_2$	-0.28	>873	Co	1.25	1768	3200	HCP
$HAuCl_4$	1.5	527	Au	1.44	1337	3129	FCC
$CuCl_2$	0.34	1266	Cu	1.28	1358	3200	FCC
$SnCl_2$	-0.14	896	Sn	1.40	505	2875	tetragonal

Reduction potential relative to standard hydrogen electrode;
FCC: face-centered-cubic; BCC: body-centered-cubic; HCP: hexagonal-close-packing.

Table S2.

Miscibility between binary elemental combinations with a 1:1 ratio. [Data from ASM Alloy Phase Diagram Database]

	Pt	Pd	Co	Ni	Fe	Au	Cu	Sn
Pt	1	0	1	1	1	1	1	0
Pd	0	1	1	1	0	1	1	1
Co	1	1	1	1	0	0	0	0
Ni	1	1	1	1	0	0	0	0
Fe	1	0	0	0	1	0	0	0
Au	1	1	0	0	0	1	1	0
Cu	1	1	0	0	0	1	1	0
Sn	0	1	0	0	0	0	0	1

Note: 1 forms an alloy or intermetallic; 0 are immiscible.

Table S3.

STEM elemental maps and ICP-MS composition of HEA-NPs with 2, 5, and 8 elements.

Elements	Method	Pt	Pd	Co	Ni	Fe	Cu	Au	Sn
2	TEM average	74.15			25.85				
	ICP-MS	72.8			27.1				
5	TEM average	28.91	19.92	24.77	19.04	7.38			
	ICP-MS	26	18.3	24.8	21	10			
8	TEM Average	18.58	15.9	12.01	12.50	9.90	9.19	17.55	4.46
	ICP-MS	20.3	17.7	10.6	10.26	9.4	9.55	18.75	3.53

Table S4.

Physical properties of Au and Cu.

Metals	Atomic Radius [Å]	Melting point [K]	Boiling point [K]	Room-T structure	Wetting at ~1330 K
Au	1.44	1337	3129	FCC	138°
Cu	1.28	1358	3200	FCC	139°

Table S5.

Composition of PtPdRhRuCe HEA-NP catalysts synthesized by the CTS method.

Composition	Pt	Pd	Rh	Ru	Ce	Loading
Design	0.8	0.15	0.035	0.005	0.01	30%
ICP MS	0.769	0.166	0.046	0.012	0.008	28.21%
TEM average	0.757	0.160	0.055	0.026	0.003	

Table S6.

Literature comparison of catalytic ammonia oxidation performance.

Catalysts[a]	NO_x yield (%)	T[b] (°C)	Reference
Pt gauze	98	800	[1]
(90-95%) Pt + (5-10%) Rh	94-96	800-950	[2]
90% Pt-5% Pd-5% Rh	96	800-1000	[3]
88% Pt-7% Pd-5% Rh	94	800-1000	[4]
92.4% Pt-4% Pd-3.5% Rh-0.1% Ce	98	900	[5]
81% Pt-15% Pd-3.5% Rh-0.5% Ru	94	900	[6]
21.7% Pt-4.68% Pd-1.3% Rh-0.34% Ru-0.23% Ce	99	700	Current work
17.2% Pt-4.1% Pd-1.1% Rh-4.1% Co-0.7% Ce	>90	600-700	Current work

[a] the composition of different metals were expressed as weight percentages

[1] J. Pérez-Ramírez, E. V. Kondratenko, G. Novell-Leruth, J. M. Ricart, Mechanism of ammonia oxidation over PGM (Pt, Pd, Rh) wires by temporal analysis of products and density functional theory. J. Catal. 261, 217–223 (2009) *(45).*

[2] J. Pérez-Ramírez, B. Vigeland, Perovskite membranes in ammonia oxidation: Towards process intensification in nitric acid manufacture. Angew. Chemie - Int. Ed. 44, 1112–1115 (2005) *(46).*

[3] P. A. J. Bagot et al., Oxidation and Surface Segregation Behavior of a Pt-Pd-Rh Alloy Catalyst. J. Phys. Chem. C. 118, 26130–26138 (2014) *(34).*

[4] L. Xin, H. Yongqiang, J. Husheng, Pt-Rh-Pd Alloy Group Gauze Catalysts Used for Ammonia Oxidation. Rare Met. Mater. Eng. 46, 339–343 (2017) *(33).*

[5] X. Hu, Y. Ning, L. Chen, Q. Shi, C. Jia, Physical Properties and Application Performance of Platinum-Palladium-Rhodium Alloys Modified with Cerium. Platin. Met. Rev. 56, 40–46 (2012) *(36).*

[6] E. F. Sutormina et al., Effect of the Reaction Medium on the Physicochemical Properties of the Oxide Monolith Catalyst IK-42-1 for Ammonia Oxidation. Kinet. Catal. 50, 892–898 (2009) *(47).*

References

1. P.-C. Chen, X. Liu, J. L. Hedrick, Z. Xie, S. Wang, Q.-Y. Lin, M. C. Hersam, V. P. Dravid, C. A. Mirkin, Polyelemental nanoparticle libraries. *Science* **352**, 1565–1569 (2016). doi:10.1126/science.aaf8402 Medline

2. L. Bu, N. Zhang, S. Guo, X. Zhang, J. Li, J. Yao, T. Wu, G. Lu, J.-Y. Ma, D. Su, X. Huang, Biaxially strained PtPb/Pt core/shell nanoplate boosts oxygen reduction catalysis. *Science* **354**, 1410–1414 (2016). doi:10.1126/science.aah6133 Medline

3. S. G. Kwon, G. Krylova, P. J. Phillips, R. F. Klie, S. Chattopadhyay, T. Shibata, E. E. Bunel, Y. Liu, V. B. Prakapenka, B. Lee, E. V. Shevchenko, Heterogeneous nucleation and shape transformation of multicomponent metallic nanostructures. *Nat. Mater.* **14**, 215–223 (2015). doi:10.1038/nmat4115 Medline

4. M. Takahashi, H. Koizumi, W.-J. Chun, M. Kori, T. Imaoka, K. Yamamoto, Finely controlled multimetallic nanocluster catalysts for solvent-free aerobic oxidation of hydrocarbons. *Sci. Adv.* **3**, e1700101 (2017). doi:10.1126/sciadv.1700101 Medline

5. X. Huang, Z. Zhao, L. Cao, Y. Chen, E. Zhu, Z. Lin, M. Li, A. Yan, A. Zettl, Y. M. Wang, X. Duan, T. Mueller, Y. Huang, High-performance transition metal-doped Pt3Ni octahedra for oxygen reduction reaction. *Science* **348**, 1230–1234 (2015). doi:10.1126/science.aaa8765 Medline

6. G. Chen, Y. Zhao, G. Fu, P. N. Duchesne, L. Gu, Y. Zheng, X. Weng, M. Chen, P. Zhang, C.-W. Pao, J.-F. Lee, N. Zheng, Interfacial effects in iron-nickel hydroxide-platinum nanoparticles enhance catalytic oxidation. *Science* **344**, 495–499 (2014). doi:10.1126/science.1252553 Medline

7. M. R. Buck, J. F. Bondi, R. E. Schaak, A total-synthesis framework for the construction of high-order colloidal hybrid nanoparticles. *Nat. Chem.* **4**, 37–44 (2011). doi:10.1038/nchem.1195 Medline

8. N. A. Frey, S. Peng, K. Cheng, S. Sun, Magnetic nanoparticles: Synthesis, functionalization, and applications in bioimaging and magnetic energy storage. *Chem. Soc. Rev.* **38**, 2532–2542 (2009). doi:10.1039/b815548h Medline

9. M. B. Cortie, A. M. McDonagh, Synthesis and optical properties of hybrid and alloy plasmonic nanoparticles. *Chem. Rev.* **111**, 3713–3735 (2011). doi:10.1021/cr1002529 Medline

10. K. D. Gilroy, A. Ruditskiy, H.-C. Peng, D. Qin, Y. Xia, Bimetallic nanocrystals: Syntheses, properties, and applications. *Chem. Rev.* **116**, 10414–10472 (2016). doi:10.1021/acs.chemrev.6b00211 Medline

11. E. Reddington, A. Sapienza, B. Gurau, R. Viswanathan, S. Sarangapani, E. S. Smotkin, T. E. Mallouk, Combinatorial electrochemistry: A highly parallel, optical screening method for discovery of better electrocatalysts. *Science* **280**, 1735–1737 (1998). doi:10.1126/science.280.5370.1735 Medline

12. P. C. Chen, G. Liu, Y. Zhou, K. A. Brown, N. Chernyak, J. L. Hedrick, S. He, Z. Xie, Q.-Y. Lin, V. P. Dravid, S. A. O'Neill-Slawecki, C. A. Mirkin, Tip-directed synthesis of

multimetallic nanoparticles. *J. Am. Chem. Soc.* **137**, 9167–9173 (2015). doi:10.1021/jacs.5b05139 Medline

13. P.-C. Chen, J. S. Du, B. Meckes, L. Huang, Z. Xie, J. L. Hedrick, V. P. Dravid, C. A. Mirkin, Structural evolution of three-component nanoparticles in polymer nanoreactors. *J. Am. Chem. Soc.* **139**, 9876–9884 (2017). doi:10.1021/jacs.7b03163 Medline

14. S. Ranganathan, Alloyed pleasures: Multiatomic cocktails. *Curr. Sci.* **85**, 1404–1406 (2003).

15. J.-W. Yeh, S.-K. Chen, S.-J. Lin, J.-Y. Gan, T.-S. Chin, T.-T. Shun, C.-H. Tsau, S.-Y. Chang, Nanostructured high-entropy alloys with multiple principal elements: Novel alloy design concepts and outcomes. *Adv. Eng. Mater.* **6**, 299–303 (2004). doi:10.1002/adem.200300567

16. B. S. Murty, J.-W. Yeh, S. Ranganathan, *High-Entropy Alloys* (Butterworth-Heinemann, 2014).

17. Z. Li, K. G. Pradeep, Y. Deng, D. Raabe, C. C. Tasan, Metastable high-entropy dual-phase alloys overcome the strength-ductility trade-off. *Nature* **534**, 227–230 (2016). doi:10.1038/nature17981 Medline

18. Y. F. Ye, Q. Wang, J. Lu, C. T. Liu, Y. Yang, High-entropy alloy: Challenges and prospects. *Mater. Today* **19**, 349–362 (2016). doi:10.1016/j.mattod.2015.11.026

19. D. C. Hofmann, J.-Y. Suh, A. Wiest, G. Duan, M.-L. Lind, M. D. Demetriou, W. L. Johnson, Designing metallic glass matrix composites with high toughness and tensile ductility. *Nature* **451**, 1085–1089 (2008). doi:10.1038/nature06598 Medline

20. D. A. Porter, K. E. Easterling, M. Y. Sherif, *Phase Transformations in Metals and Alloys* (CRC Press, ed. 3, 2009).

21. Materials and methods are available as supplementary materials.

22. N. Eustathopoulos, M. G. Nicholas, B. B. Drevet, *Wettability at High Temperatures* (Elsevier, 1999), vol. 3.

23. M. Lukas, V. Meded, A. Vijayaraghavan, L. Song, P. M. Ajayan, K. Fink, W. Wenzel, R. Krupke, Catalytic subsurface etching of nanoscale channels in graphite. *Nat. Commun.* **4**, 1379 (2013). doi:10.1038/ncomms2399 Medline

24. F. Tao, M. E. Grass, Y. Zhang, D. R. Butcher, J. R. Renzas, Z. Liu, J. Y. Chung, B. S. Mun, M. Salmeron, G. A. Somorjai, Reaction-driven restructuring of Rh-Pd and Pt-Pd core-shell nanoparticles. *Science* **322**, 932–934 (2008). doi:10.1126/science.1164170 Medline

25. M. A. Newton, C. Belver-Coldeira, A. Martínez-Arias, M. Fernández-García, Dynamic in situ observation of rapid size and shape change of supported Pd nanoparticles during CO/NO cycling. *Nat. Mater.* **6**, 528–532 (2007). doi:10.1038/nmat1924 Medline

26. F. Tao, S. Dag, L.-W. Wang, Z. Liu, D. R. Butcher, H. Bluhm, M. Salmeron, G. A. Somorjai, Break-up of stepped platinum catalyst surfaces by high CO coverage. *Science* **327**, 850–853 (2010). doi:10.1126/science.1182122 Medline

27. P.-H. Lu *et al*., Highly deformable and mobile palladium nanocrystals as efficient carbon scavengers. arXiv:1802.00207 [physics.app-ph] (1 Feb 2018).

28. N. Combe, P. Jensen, A. Pimpinelli, Changing shapes in the nanoworld. *Phys. Rev. Lett.* **85**, 110–113 (2000). doi:10.1103/PhysRevLett.85.110 Medline

29. C. C. Wang, Q.-J. Li, L. Chen, Y.-H. Cheng, J. Sun, Z.-W. Shan, J. Li, E. Ma, Ultrafast shape change and joining of small-volume materials using nanoscale electrical discharge. *Nano Res.* **8**, 2143–2151 (2015). doi:10.1007/s12274-014-0685-7

30. D.-G. Xie, Z.-J. Wang, J. Sun, J. Li, E. Ma, Z.-W. Shan, In situ study of the initiation of hydrogen bubbles at the aluminium metal/oxide interface. *Nat. Mater.* **14**, 899–903 (2015). doi:10.1038/nmat4336 Medline

31. D. Wang, Y. Li, One-pot protocol for Au-based hybrid magnetic nanostructures via a noble-metal-induced reduction process. *J. Am. Chem. Soc.* **132**, 6280–6281 (2010). doi:10.1021/ja100845v Medline

32. D. M. Considine, *Chemical and Process Technology Encyclopedia* (CRC Press, 1974).

33. L. Xin, H. Yongqiang, J. Husheng, Pt-Rh-Pd alloy group gauze catalysts used for ammonia oxidation. *Rare Met. Mater. Eng.* **46**, 339–343 (2017). doi:10.1016/S1875-5372(17)30091-7

34. P. A. J. Bagot, K. Kruska, D. Haley, X. Carrier, E. Marceau, M. P. Moody, G. D. W. Smith, Oxidation and surface segregation behavior of a Pt-Pd-Rh alloy catalyst. *J. Phys. Chem. C* **118**, 26130–26138 (2014). doi:10.1021/jp508144z

35. B. V. I. Chernyshov, I. M. Kisil, Platinum metals catalvtic systems in nitric acid production. *Platin. Met. Rev.* **37**, 136–143 (1993).

36. X. Hu, Y. Ning, L. Chen, Q. Shi, C. Jia, Physical properties and application performance of platinum-palladium-rhodium alloys modified with cerium. *Platin. Met. Rev.* **56**, 40–46 (2012). doi:10.1595/147106711X615749

37. C. B. Alcock, V. P. Itkin, M. K. Horrigan, Vapour pressure equations for the metallic elements: 298–2500K. *Can. Metall. Q.* **23**, 309–313 (1984). doi:10.1179/cmq.1984.23.3.309

38. H. W. Kim, H. W. Yoon, S.-M. Yoon, B. M. Yoo, B. K. Ahn, Y. H. Cho, H. J. Shin, H. Yang, U. Paik, S. Kwon, J.-Y. Choi, H. B. Park, Selective gas transport through few-layered graphene and graphene oxide membranes. *Science* **342**, 91–95 (2013). doi:10.1126/science.1236098 Medline

39. L. S. Lobo, S. A. C. Carabineiro, Kinetics and mechanism of catalytic carbon gasification. *Fuel* **183**, 457–469 (2016). doi:10.1016/j.fuel.2016.06.115

40. B. L. Farrell, V. O. Igenegbai, S. Linic, A viewpoint on direct methane conversion to ethane and ethylene using oxidative coupling on solid catalysts. *ACS Catal.* **6**, 4340–4346 (2016). doi:10.1021/acscatal.6b01087

41. U. Zavyalova, M. Holena, R. Schlögl, M. Baerns, Statistical analysis of past catalytic data on oxidative methane coupling for new insights into the composition of high-performance catalysts. *Chem. Cat. Chem.* **3**, 1935–1947 (2011). doi:10.1002/cctc.201100186

42. B. H.-Y. Chen, H.-L. R. Chang, Development of low temperature three-way catalysts for future fuel efficient vehicles. *Johnson Matthey Technol. Rev.* **59**, 64–67 (2015). doi:10.1595/205651315X686011

43. G. Liu, P.-X. Gao, A review of NO_x storage/reduction catalysts: Mechanism, materials and degradation studies. *Catal. Sci. Technol.* **1**, 552–568 (2011). doi:10.1039/c1cy00007a

44. C. Carrillo, H. Xiong, A. T. DeLaRiva, D. Kunwar, E. J. Peterson, S. R. Challa, G. Qi, S. Oh, M. H. Wiebenga, X. I. P. Hernandez, Y. Wang, A. K. Datye, Designing catalysts for meeting the DOE 150° C challenge for exhaust emissions. *Microsc. Microanal.* **23** (S1), 2028–2029 (2017). doi:10.1017/S1431927617010807

45. J. Pérez-Ramírez, E. V. Kondratenko, G. Novell-Leruth, J. M. Ricart, Mechanism of ammonia oxidation over PGM (Pt, Pd, Rh) wires by temporal analysis of products and density functional theory. *J. Catal.* **261**, 217–223 (2009). doi:10.1016/j.jcat.2008.11.018

46. J. Pérez-Ramírez, B. Vigeland, Perovskite membranes in ammonia oxidation: Towards process intensification in nitric acid manufacture. *Angew. Chem. Int. Ed.* **44**, 1112–1115 (2005). doi:10.1002/anie.200462024 Medline

47. E. F. Sutormina, L. A. Isupova, A. N. Nadeev, V. A. Rogov, V. P. Ivanov, E. B. Burgina, A. A. Budneva, Effect of the reaction medium on the physicochemical properties of the oxide monolith catalyst IK-42-1 for ammonia oxidation. *Kinet. Catal.* **50**, 892–898 (2009). doi:10.1134/S0023158409060160